

NUMERICAL AND EXPERIMENTAL STUDY ON IMPROVING DIAGNOSIS IN  
STRUCTURAL HEALTH MONITORING

By

JUNGEUN AN

A DISSERTATION PRESENTED TO THE GRADUATE SCHOOL  
OF THE UNIVERSITY OF FLORIDA IN PARTIAL FULFILLMENT  
OF THE REQUIREMENTS FOR THE DEGREE OF  
DOCTOR OF PHILOSOPHY

UNIVERSITY OF FLORIDA

2011

© 2011 Jungeun An

To my parents

## ACKNOWLEDGMENTS

First of all, I would like to give special thanks and appreciation to Dr. Raphael T. Haftka, the chairman of my advisory committee. I am grateful to him for providing me with this excellent opportunity to complete my doctoral studies. I sincerely hope we will remain in contact in the future. I would also like to thank to Dr. Nam-Ho Kim, co-chairman of my advisory committee, for his valuable comments at our weekly meeting. I would also like to thank to Dr. Mark Sheplak and Michael J. Daniels for their willingness to review my Ph.D. research and to provide me with the constructive comments which helped me to complete this dissertation.

I also wish to express my gratitude to Dr. Fuh-Gwo Yuan from North Carolina State University, who worked together to provide a large share of knowledge and insight to the future of our research. The experience he supplied me greatly contributed to this dissertation.

I thank Dr. Byung Man Kwak from Korea Advanced Institute of Science and Technology, who was my advisor during my PhD study in Korea, for kind and helpful advice. He had shown a good attitude toward research. I also thank Dr. Hoon Sohn and Mr. Chul-Min Yeum from Korea Advanced Institute of Science and Technology for helping me to do the experiment. Since their great knowledge and experience in this field helped me a lot, I had a wonderful opportunity to co-author a journal paper with them.

I also thank to my colleagues at the Structural and Multidisciplinary Group of the Mechanical and Aerospace Engineering Department of the University of Florida for their support, friendship and many technical discussions.

I thank Rick Ross, Thiagaraja Krishnamurthy and Tzikang Chen from NASA for their comments and question all along this research. I also thank the Air Force Office of Scientific Research (Grant: FA9550-07-1-0018) and NASA (Grant: NNX08AC334) for their great interest and funding of this research.

I also would like to express my deepest appreciation to my parents for their emotional support.

# TABLE OF CONTENTS

	<u>page</u>
ACKNOWLEDGMENTS.....	4
LIST OF TABLES.....	8
LIST OF FIGURES.....	9
LIST OF SYMBOLS AND ABBREVIATIONS .....	13
ABSTRACT .....	15
1 INTRODUCTION .....	17
Aircraft Maintenance and Its Impact on Safety .....	17
Structural Health Monitoring (SHM) .....	19
Damage Diagnosis .....	21
Damage Severity .....	25
Damage Prognosis .....	26
Objective of This Research.....	28
How to Achieve the Objective .....	29
2 BASIC PRINCIPLES.....	31
Lamb Wave Propagation in a Thin Plate.....	31
Wave Equation .....	31
Wave Scatter .....	37
Piezoelectric Materials .....	39
Actuation Equation .....	40
Sensing Equation .....	42
Analytical Solution to a Toneburst Excitation .....	44
Wavefield Simulation [51, 54] .....	53
Governing Equations of Flexural Waves .....	53
Finite Difference Algorithm .....	55
3 IDENTIFYING CRACK LOCATION USING MIGRATION TECHNIQUE.....	59
Migration Technique .....	59
Bayesian Approach.....	66
Bayesian Approach .....	66
Direct Image Intensity.....	69
Multivariate Normal Model about Center of Intensity .....	70
Compensation for Geometrical Decay .....	73
Geometrical Decay in Plate Wave.....	75
Application to Migration Technique .....	77

	Numerical Simulation .....	78
4	EXPERIMENTAL STUDY ON IDENTIFYING CRACKS OF INCREASING SIZE ...	82
	Test Panel and Test Procedure .....	82
	Results.....	88
	Scattered Signal from the Damage .....	88
	Variation of the Signal with Crack Size.....	88
	Effect of Frequency .....	91
	Crack Location Effect .....	94
	Migration Technique with Experimental Data.....	96
5	BAYESIAN APPROACH TO IMPROVE DIAGNOSIS FROM PAST PROGNOSIS.....	100
	Modeling .....	100
	Improved Diagnosis by using Bayesian Approach.....	104
	Constructing Prior Distribution using Different Prognosis .....	106
	Perfect Prognosis .....	107
	Uncertainty in Crack Propagation Parameters .....	108
	Prognosis using Least Squares Fit of Paris Law .....	110
	Prognosis using Least Squares (Non-Physics Model).....	112
6	CONCLUSION.....	116
	LIST OF REFERENCES .....	117
	BIOGRAPHICAL SKETCH.....	124

## LIST OF TABLES

<u>Table</u>		<u>page</u>
2-1	Properties of piezoelectric disc .....	45
3-1	Estimation error due to different imaging techniques.....	73
3-2	Comparison of accuracy, different imaging results. ....	80
3-3	Comparison of imaging results .....	80
4-1	Mechanical properties of aluminum plate .....	83
4-2	Properties of piezoelectric disc (modified PZT-4) .....	83
4-3	List of crack sizes tested, (unit: mm) .....	83
4-4	Comparison of different imaging methods .....	96
5-1	Parameters related to simulated crack propagation. ....	102
5-2	Comparison of accuracy with 10000 MCS.....	114
5-3	Comparison of accuracy with 1000 MCS when $\Delta N=25$ cycles .....	115



## LIST OF FIGURES

<u>Figure</u>	<u>page</u>
1-1 Safety record from worldwide commercial jet fleet [1] .....	17
1-2 Fatigue crack growth [2] .....	18
1-3 Structural Health Monitoring .....	20
1-4 Pitch-catch method [8].....	22
1-5 Pulse-echo method [8].....	23
1-6 Phased array method [8] .....	23
1-7 Migration technique [53] .....	24
1-8 Time of Flight Diffraction (TOFD) [34].....	26
1-9 Fatigue crack size estimation [35] .....	26
1-10 Applying crack propagation model to improve accuracy of detection results.....	29
2-1 Axisymmetric structural waves in plates in cylindrical coordinates .....	32
2-2 Symmetric and antisymmetric particle motion across the plate thickness .....	33
2-3 Typical wave speed dispersion curves for symmetric and antisymmetric waves. ....	36
2-4 Wave reflection from a small cavity .....	37
2-5 Circular piezoelectric actuator .....	40
2-6 Hole detection problem.....	45
2-7 Five peaked toneburst excitation sent to the actuator (110 kHz) .....	46
2-8 PZT actuator attached to an aluminum plate .....	47
2-9 Displacement at the boundary of the PZT ( $r=a$ ).....	48
2-10 Displacement field induced by the piezoelectric actuation.....	50
2-11 Scattered displacement response at $r=113.4$ mm from the cavity center. ....	51
2-12 Electric signal obtained at the sensor position.....	51

2-13	Comparison with experimental data .....	52
2-14	Snapshot of the simulated structural wave .....	57
2-15	Finite difference solution compared with wave propagation analysis .....	58
3-1	Cross-correlation coefficient used to find the time difference between excitation and scattered signal in migration technique. ....	60
3-2	Actuator and sensor positions for migration technique .....	61
3-3	Excitation signal.....	63
3-4	Scattered wavefield and incident wavefield for back propagation.....	64
3-5	Final images obtained by evaluating the image intensity at each point from simulation for a 50mm straight horizontal crack.....	65
3-6	Combining image using direct image intensity as likelihood.....	70
3-7	Estimation error in x and y directions.....	71
3-8	Combined image using multivariate normal model. ....	72
3-9	Possible errors related to geometrical decay.....	74
3-10	Signal decay with respect to wave propagation in plate .....	76
3-11	An example of compensated signal displayed on time scale.....	77
3-12	Images from migration technique with the same sensor data.....	79
3-13	Image intensity distribution for a single actuator image .....	80
4-1	Layout of actuators and sensors.....	84
4-2	Damage manufactured to the plate .....	84
4-3	Signal generation and acquisition in the experimental set-up.....	85
4-4	Test procedure for estimated location by migration technique and signal amplitude measurement .....	86
4-5	Frequency sweep experiment.....	87
4-6	Toneburst excitation measured from all eight sensors from simulation and experiment.....	89
4-7	Experimental scattered signal amplitude change in different size cracks. ....	90

4-8	Signal amplitude variation (maximum peak-to-peak amplitude). .....	91
4-9	Scattered signal amplitude with 150kHz excitation.....	92
4-10	Signal amplitude variation (maximum peak-to-peak amplitude). .....	93
4-11	Different crack center location with respect to the actuator positions: second crack center location is (-100mm, -140mm) .....	95
4-12	Scattered signal amplitude variation for cracks growing at a different location excited by 110 kHz ultrasonic toneburst. ....	95
4-13	Reconstructed scattered wavefield .....	97
4-14	Experimental result is reproduced into image using migration technique. ....	97
4-15	Combination of all 7 actuators available in the experiment.....	98
5-1	Aircraft fuselage.....	101
5-2	Simplified loading condition .....	101
5-3	Crack propagation. ....	103
5-4	Sample of detected estimated crack sizes (based on Eq.5-3).....	104
5-5	Simulation procedure.....	106
5-6	Probability distribution function of crack size updated at every 50 cycles.....	108
5-7	Crack size found by Bayesian update .....	108
5-8	Probability distribution function of crack size updated at every 50 cycles with uncertain parameters C and m. ....	109
5-9	Crack size found by Bayesian update with uncertain C and m.....	109
5-10	Approximation of the inspection data by Least squares fit of Paris law with 95% prediction bounds. ....	110
5-11	Estimated crack size by least square fitting of Paris law at each inspection cycle .....	111
5-12	Demonstration of the suggested method to estimate crack size by Bayesian approach using prognosis based on least squares.....	111
5-13	Approximation of the inspection data by 4 <sup>th</sup> order polynomial with 95% prediction bounds. Only 40 recent data are used for curve fitting.....	113

5-14 Estimated crack size by least square fitting using a quartic polynomial at  
each inspection cycle ..... 113

## LIST OF SYMBOLS AND ABBREVIATIONS

A	Signal amplitude
a	Crack size
$a_i$	Initial crack size
C, m	Crack propagation parameters
c	Phase velocity of a Lamb wave
$c_g$	Group velocity of a Lamb wave
$c_L$	Pressure wave velocity
$c_T$	Shear wave velocity
$D_3$	Electrical displacement in z-direction (charge per unit area)
d	Plate thickness
$d_{31}, d_{33}$	Piezoelectric coupling constant
$E_3$	Electric field in z-direction
$\epsilon$	Mechanical strain
FFT	Fast Fourier Transform
H	Heaviside step function
$H_n$	Hankel functions
iFFT	inverse FFT
$I^i$	Image intensity from $i^{\text{th}}$ simulation or experiment
$I_{d\text{-corr}}$	Adjusted image intensity by geometrical decay compensation
$J_n$	Bessel functions
k	Wave number
$l$	Likelihood
$\lambda, \mu$	Lamé constants
N	Number of cycles

$\nu$	Poisson's ratio
NDE	Non destructive evaluation
PZT	Lead zirconate titanate, a ceramic perovskite material that shows a marked piezoelectric effect.
RUL	Remaining useful life
SHM	Structural health monitoring, an automated inspection and maintenance system development
$s^E$	Mechanical compliance
$\sigma$	Mechanical stress
TOF	Time of flight, time difference between excitation signal and scattered signal
$\Phi_{fg}$	Cross-correlation (coefficient)
$\omega$	Angular frequency

Abstract of Dissertation Presented to the Graduate School  
of the University of Florida in Partial Fulfillment of the  
Requirements for the Degree of Doctor of Philosophy

NUMERICAL AND EXPERIMENTAL STUDY ON IMPROVING DIAGNOSIS IN  
STRUCTURAL HEALTH MONITORING

By

Jungeun An

August 2011

Chair: Raphael Tuvia Haftka  
Major: Aerospace Engineering

Structural Health Monitoring (SHM) is a procedure of assessing structural integrity during its service period to improve maintenance in terms of cost and reliability. In SHM for aircraft applications, crack identification using reflected ultrasonic Lamb waves from a crack is one of the most active research areas. In addition to detecting a crack, estimating its size is important for judging the severity of the damage, and this can be done by various techniques. Specifically, we focus on the relationship between the sensor signal amplitude and crack size through experiments and simulation for help in size estimation. The maximum received signal amplitude is found to vary linearly from simulation and this agrees with measurements with crack size up to 30 mm.

However, SHM using embedded sensors have limitation in terms of accuracy of detection. Our approach to overcome this is as follows. If measurements are frequently performed using the above mentioned techniques while the crack grows, then a better estimation of crack size may be possible by analyzing sensor signals for the same crack location at different sizes.

The main objective of this research is to improve the accuracy of current diagnosis by using the prediction from previous inspection results. Unlike manual inspection, SHM

can take frequent measurements and trace crack growth. By taking advantage of this aspect, higher accuracy about current crack size can be achieved. First, using the previous SHM measurements and the crack propagation model, we predict the statistical distribution of crack sizes at the next SHM inspection cycle. Then, this predicted distribution is combined with the SHM measurement at the next cycle by using the Bayesian approach for more precise estimate. The propagated distribution from the previous inspection is used as a prior and the variability at the current inspection is used to build the likelihood function. The uncertainty in measurements is modeled by a lognormal distribution. Results show substantial improvements in accuracy.



## CHAPTER 1 INTRODUCTION

### Aircraft Maintenance and Its Impact on Safety

The importance of proper maintenance to prevent fatigue failure is a key issue for all mechanical components in an airplane. As shown in Figure 1-1, major catastrophic failures of aircrafts come from lack of maintenance and repair rather than design errors in commercial jet fleets [1].

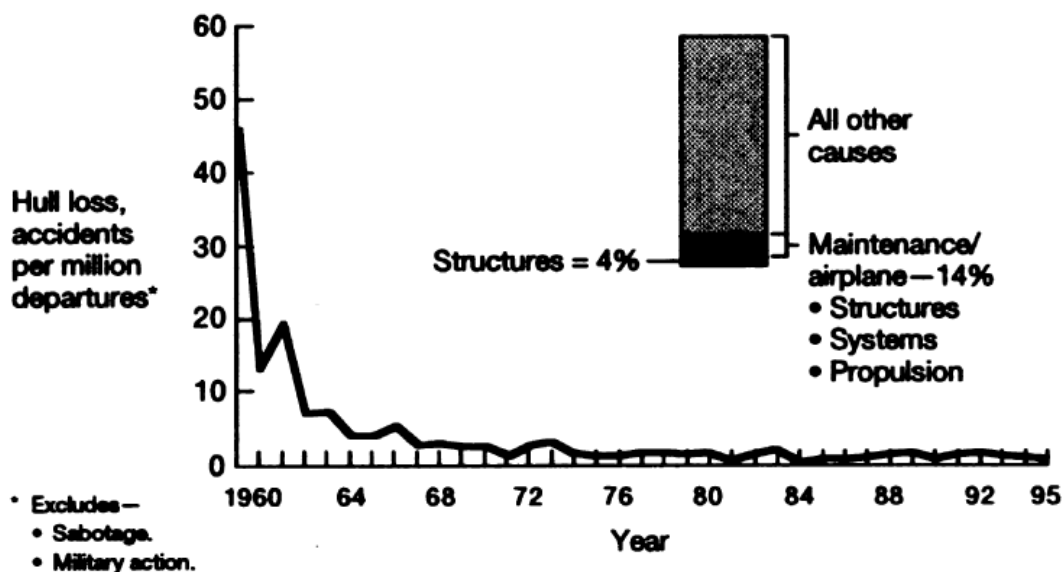


Figure 1-1. Safety record from worldwide commercial jet fleet [1]

Fatigue crack growth is one of the most common types of failure in an aircraft since the safety factor of designed aircraft is relatively low, and the aircraft is subjected to many different types of cyclic loadings during its service period. Cracks usually start from inherent material defects or micro-cracks, increase their size by cyclic loadings, and eventually lead the structure to fail.

Many crack propagation models are proposed to describe the behavior of fatigue crack growth. Fatigue cracks usually propagate very slowly in the beginning, but the

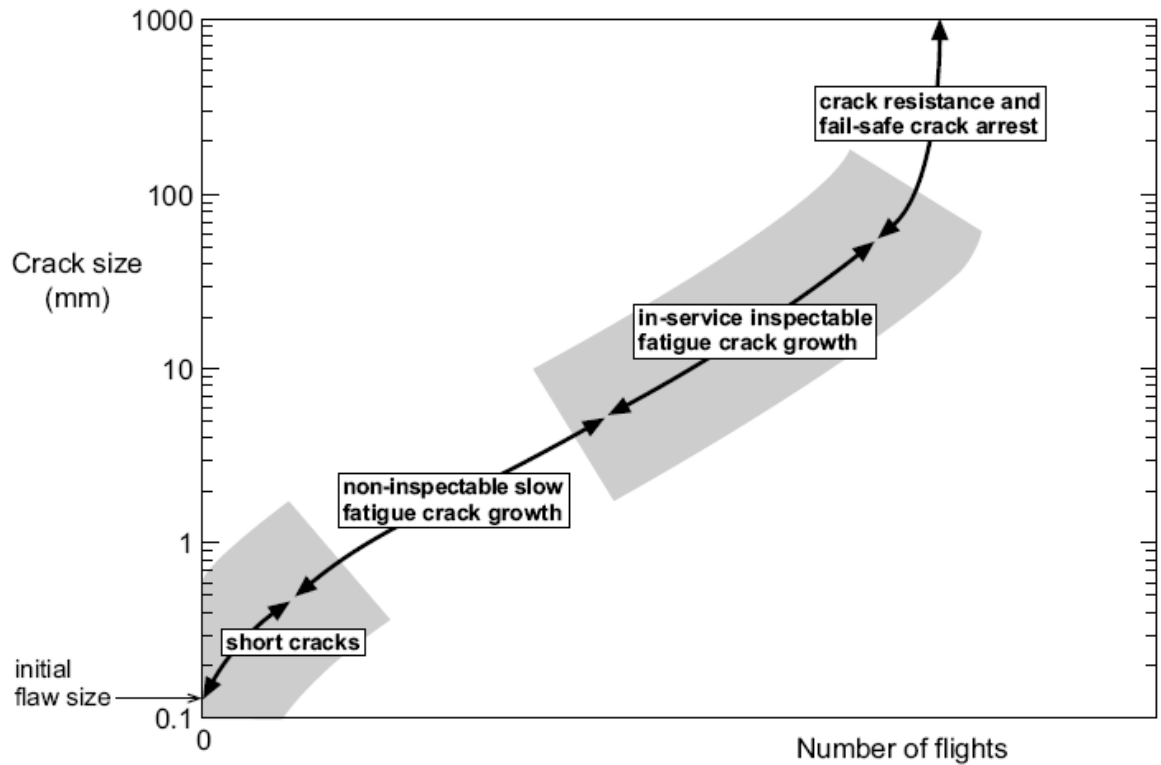


Figure 1-2. Fatigue crack growth [2]

propagation speed increases exponentially with time. Since the cracks in the beginning stage are too small to detect, most inspection methods focus on the stable crack growth stage (refer to Figure 1-2).

In FAA regulations, inspections of an aircraft in service should be scheduled on an annual basis to maintain structural safety [3]. Under current approach, the aircraft is inspected under fixed schedule in order to replace panels with any sub-millimeter size cracks that might become dangerous before the next inspection. This is called manual inspection, or preventive maintenance. The aircraft is sent to a hanger, and damaged panel in an aircraft is identified using several inspection techniques and replaced. The cost for this procedure includes downtime of the aircraft and high labor costs. Since the number of panels that are replaced during the entire service period of an airplane is

about 2 – 3%, most of cost is spent on inspecting panels that do not have cracks with significant size.

To prevent all possible failures between inspections, the manual inspection procedures should be very accurate. In fact, the current state-of-the-art manual inspection procedure is so accurate that some of sub-millimeter cracks within the structure can be detected during the inspection [4]. However, manual inspection is very costly and time consuming, and there are “hot-spots” where the reliability is crucial but inspectors cannot access easily during the manual inspection procedure. If we can automate the inspection procedure, the diagnosis of current health status of the structure under operation can be more reliable. As a result, we can reduce the overall costs and obtain a better knowledge about the possible failure of the structure simultaneously.

This is the reason for interest in condition-based maintenance over preventive maintenance. Structural health monitoring (SHM) is an enabling technology that can detect, diagnose, and predict the structural behavior under unsupervised modes. There is great interest in developing SHM using embedded sensors as an alternative for manual inspection [5-45]. The next section will explain the basic concepts of SHM, followed by literature review on damage diagnosis and prognosis.

### **Structural Health Monitoring (SHM)**

Structural health monitoring (SHM) is an integrated technology of assessing structural damage using an automated procedure. The importance of SHM is currently increasing because of economic and safety reasons.

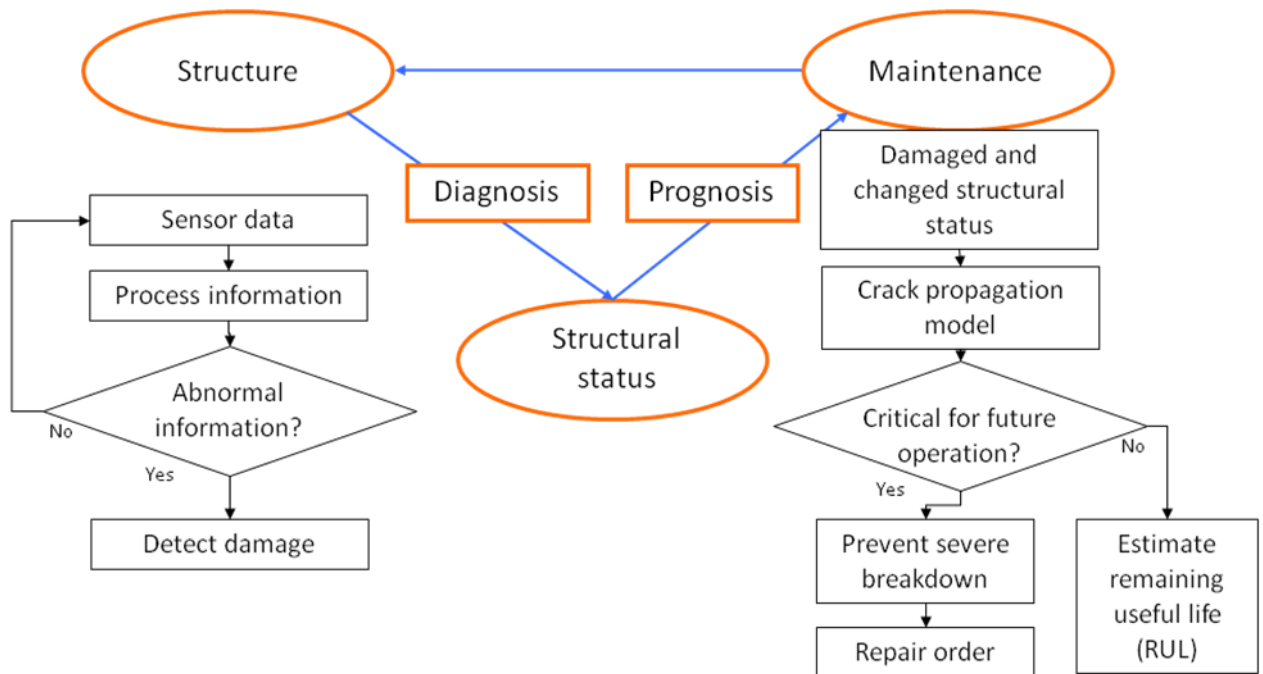


Figure 1-3. Structural Health Monitoring

As shown in Figure 1-3, SHM consists of diagnosis and prognosis. Diagnosis in SHM processes the signal from embedded sensors to detect the damage. When damage is found, prognosis uses a crack propagation model to find out the future behavior of the damage and whether the part needs maintenance or not.

Initially the development of SHM technologies focused on damage detection using embedded sensors, and progressively moved toward the future behavior of the damage. With SHM systems, we can perform the damage assessment at any time, so that the system can execute continuous monitoring of the structure. Using the monitored data from SHM systems, we can predict the damage growth and design the maintenance schedule in accordance with the most critical damage for an airplane.

The main advantage of SHM is that we can perform condition-based maintenance by following crack propagation, thereby substantially increasing the average time

intervals between downtime between maintenance and reducing the total number of replaced panels during the entire service period of an aircraft [45].

### **Damage Diagnosis**

Damage diagnosis refers to the procedure of identifying the current damage state. This includes damage detection, material property characterization, and determination of dangerous spots. For an automated procedure of diagnosis, several non-destructive evaluation (NDE) techniques have been developed by many researchers. Modern NDE techniques include radioscopy, ultrasonic guided wave scanning, shearography, dye penetrant testing, magnetic resonance imagery, laser interferometry, acoustic holography, infrared thermography, fiber optics and eddy-current [6-26]. Among them, ultrasonic guided wave based methods are very popular and widely developed and used since they have several advantages such as better sensitivity to local damage [6-11]. They are cheap, easy to implement, and enable active sensing and monitoring. They use piezoelectric transducers for excitation of Lamb waves, which are a type of structural waves in plate structures. Lamb waves are guided by two parallel free surfaces, and their wavelengths are of the same order of magnitude as the thickness of the plate [7].

Currently developed techniques using ultrasonic wave include pitch-catch, pulse-echo, phased array, and migration technique [8-10]. Basic measurements for all of these techniques include the time of flight (TOF), phase change, frequency and amplitude change, and angle of wave deflection. Among them, the time of flight, which indicates the time difference between excitation and sensing, is the most reliable in locating the damage; so many methods rely on this property.

The pitch-catch method detects damage from the changes in the Lamb wave traveling through the damaged region. The change in the wave propagation path due to damage causes the difference between the healthy state and damaged state. This method uses transducers in pairs: transmitter and receiver. The difference in the structural wave traveling from transmitter and receiver evaluates the damage located between this pair. The process is shown in Figure 1-4. In general, this method is good for determining the damage existence, but is not sensitive to location or size of the damage. To overcome these difficulties, many researchers have proposed several methods in this category [21].

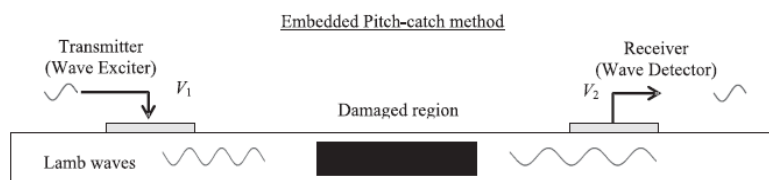


Figure 1-4. Pitch-catch method [8]

The pulse-echo method (Figure 1-5) relies on the scattered wave from damages to detect them. The transmitters and receivers are located on the same side of the damage to evaluate reflection in this method. If the velocity of the Lamb waves is known, we can calculate the distance from which the location of damage can be found. This method provides wider coverage with the same set of actuator-sensor pairs, and the TOF is more sensitive to the location of damage than pitch-catch method. However, since the scattered signal is much smaller than the original excitation, it may easily be contaminated by noise. Although no significant improvements have been made on the method itself, pulse-echo is still widely used in many SHM applications [9].

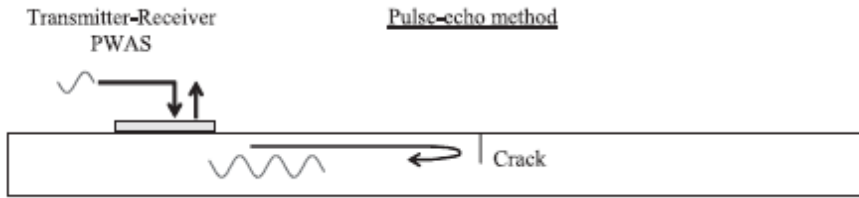


Figure 1-5. Pulse-echo method [8]

The phased array method (Figure 1-6) is adopted from the principles used by the radar systems. Many excitation sources located in a compact region send Lamb waves with different frequencies at the same time. Then the phase change in the received signal forms an image, in which the maximum phase change indicates the possible location of damage. This method is suitable to examine inner structural damage in a 3-D medium. Many researchers have tried to improve this technique, and there is a wide variety of phased array methods available for different applications. [8, 31]

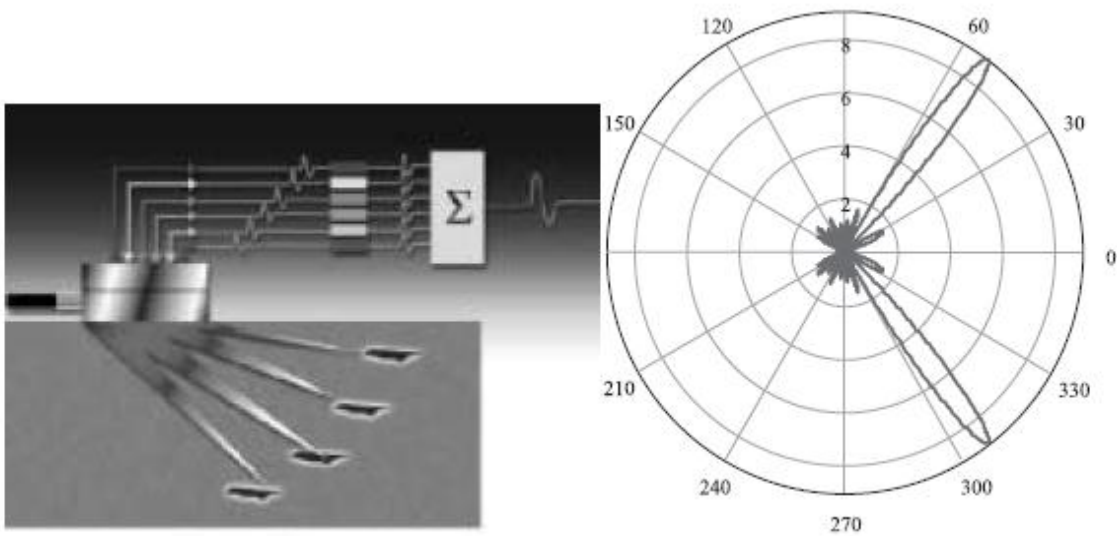


Figure 1-6. Phased array method [8]

The migration technique (Figure 1-7) is one of the most powerful tools to detect damage in a structure. Its basic principle is almost the same as pulse-echo technique, but the major difference is that we find the cross-correlation between the excitation and

scattered wave to accurately find the location of damage. A solid foundation of the migration technique has been established over nearly a decade [51-56]. Since damage identification used in this work is based on the migration technique, this method is explained in detail in Chapter 3.

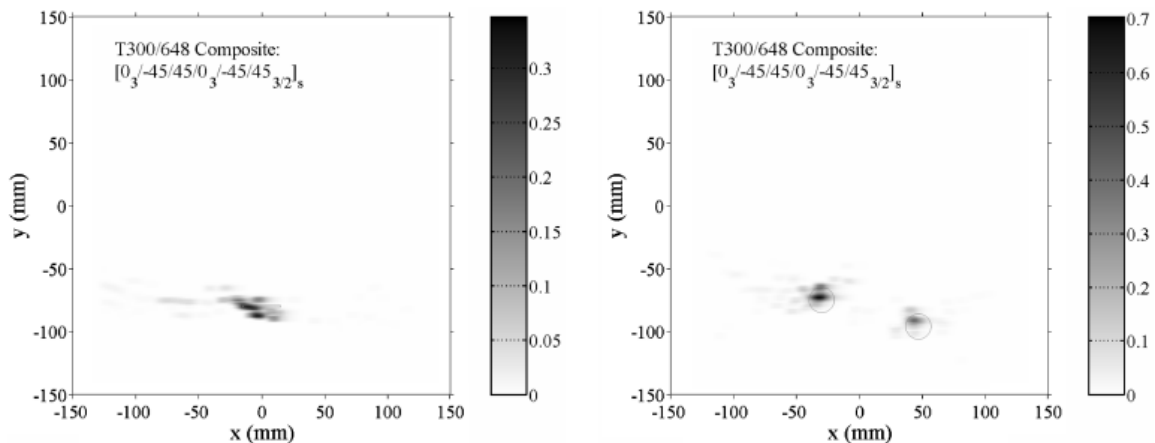


Figure 1-7. Migration technique [53]

There are many other techniques to identify damage within a structure, but every active monitoring technique using ultrasonic wave is classified into one of the categories in terms of sending and receiving signals. For example, the time reversal technique whose biggest advantage is no requirement for baseline information is a type of pitch-catch algorithm [32], and methods employing sensor network are a hybrid form of pitch-catch and pulse-echo techniques [37, 38].

There are several other techniques that produce results in the form of images [39-42]. For example, DORT method is developed based on time reversal operator and there is an attempt to apply tomography to SHM [40]. L-SAFT processing technique produces modified B-scan type images of Lamb wave inspection results [42].



## Damage Severity

The term “damage severity” can indicate many different aspects of a flaw. A severe damage can be a flaw at the most critical location with structural load, or it can be a huge flaw at a relatively less critical location. Although there is no objective measure of severity, the size is usually the most important information for assessing damage severity. Since the location of a flaw is closely related to the size, the size estimation does not have a meaning when we do not know the location of damage [5]. This is why most of current research for two dimensional applications focuses more on the existence or location of damage rather than accurate quantification. However, there have been techniques to estimate damage size using ultrasonic wave or change in the natural frequency when the approximate location of the damage is known. Time of flight diffraction (TOFD) is a well known approach of estimating the defect size and location in beams by embedded PZT sensors [34]. The diffracted signal is measured at the receiver to estimate the size of a crack as shown in Figure 1-8.

Also, several other approaches were used for beam structures. Fromme [35] demonstrated a fatigue crack growth in a beam by using the change in the reflected signal, and compared it with simulation results. He demonstrated that the signal amplitude and crack size are related, but the signal amplitude might not be accurate enough to determine crack size by comparison between simulation and experiment (Figure 1-9).

Currently, the estimation of flaw size is not ready for real-life implementation yet. Sohn et al. [7] mentioned that the crack sizes are obtained with errors that can be as large as 21% even for a beam. The size estimation part is of great interest to most developers in SHM.

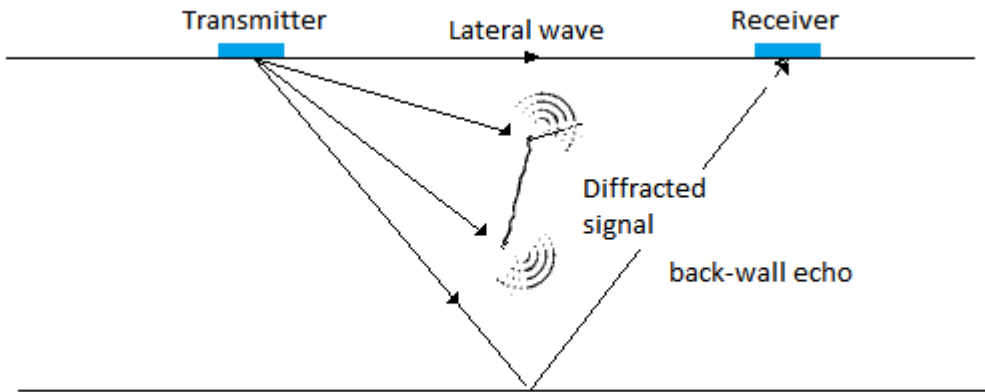


Figure 1-8. Time of Flight Diffraction (TOFD) [34]

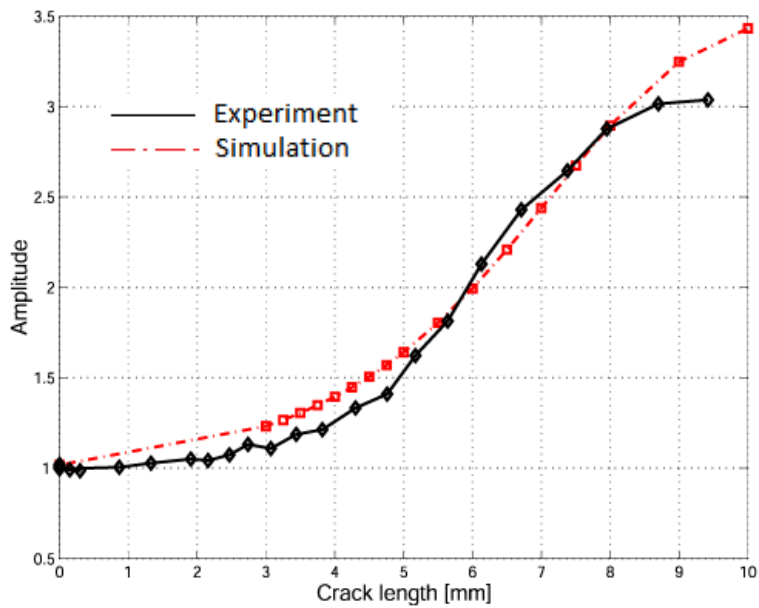


Figure 1-9. Fatigue crack size estimation [35]

### Damage Prognosis

Prognosis is a process to make a prediction about the future behavior of damage.

This includes remaining useful life (RUL) estimation, crack propagation behavior

prediction and the adjustment of maintenance schedule. . If accurate RUL can be estimated, the propagation of cracks and the next maintenance schedule can easily be calculated. Therefore, the research in prognosis naturally focuses on accurately estimating the RUL. In general, prognosis requires a good knowledge on the uncertainties in the detection capabilities, average and prospective loading, and material properties that governs damage growth. Because of these uncertainties, RUL should be modeled as a statistical distribution.

The research on prognosis has several challenges. Estimated future loadings and estimated crack size contain large uncertainty, and the crack propagation model is not exact. Despite all these practical difficulties, research on prognosis is vigorous these days. Started from Paris' law [74] in early 1960's, the crack propagation model has experienced rapid advances. Elber [75] observed that the effect of crack closure is important, and the model using effective range of stress intensity factor was developed by Paris et al. [74]. Recent developments in crack propagation model include universal model of Paris' law [76] and NASGRO model that can be used with more number of parameters.

Since there is no actual SHM system installed on an aircraft, most research on prognosis relies on conceptual SHM system. Kulkarni and Achenbach [59] have analyzed a conceptual SHM system to quantify the effects of imperfect inspections during the growth of a macrocrack. However, the effort to implement SHM in a practical system is being developed, and many researchers estimated the RUL through several examples. For example, Wang and Youn [60] have applied real time prognostics and health management to estimate RUL in a statistical manner. Also, on-line structural

health monitoring strategy has been applied to integrated prognosis model by Mohanty et al. [61]

This work employs prognosis model for predicting future behavior. Paris' law for relatively simple example is encountered for improving diagnosis. We also considered data-driven models for prognosis.

### **Objective of This Research**

The objective of this work is to develop a diagnosis method to identify crack information using ultrasonic wave, and explain how to make the diagnostic result more accurate by employing past prognosis information. From the diagnosis result, it is possible to obtain information of current crack such as its location and size. During regular inspection cycles, those inspection results are used to make a prediction about the crack size at the next inspection (prognosis). This forms a prior knowledge about the crack size before we actually take the measurements. When we have the measurement at the corresponding cycle, the current crack size is estimated by combining the prior knowledge with the inspection data. Therefore, the main objective of this research is to provide a framework that incorporates the crack propagation model to improve size estimation result (Figure 1-10).

The current developments of SHM system consider the diagnosis and prognosis as two separate procedures (Figure 1-3). However, we can improve the diagnosis by using the crack propagation model and current inspection as a predictor-corrector concept. We bring the crack propagation model into the loop of diagnosis to improve diagnosis result.

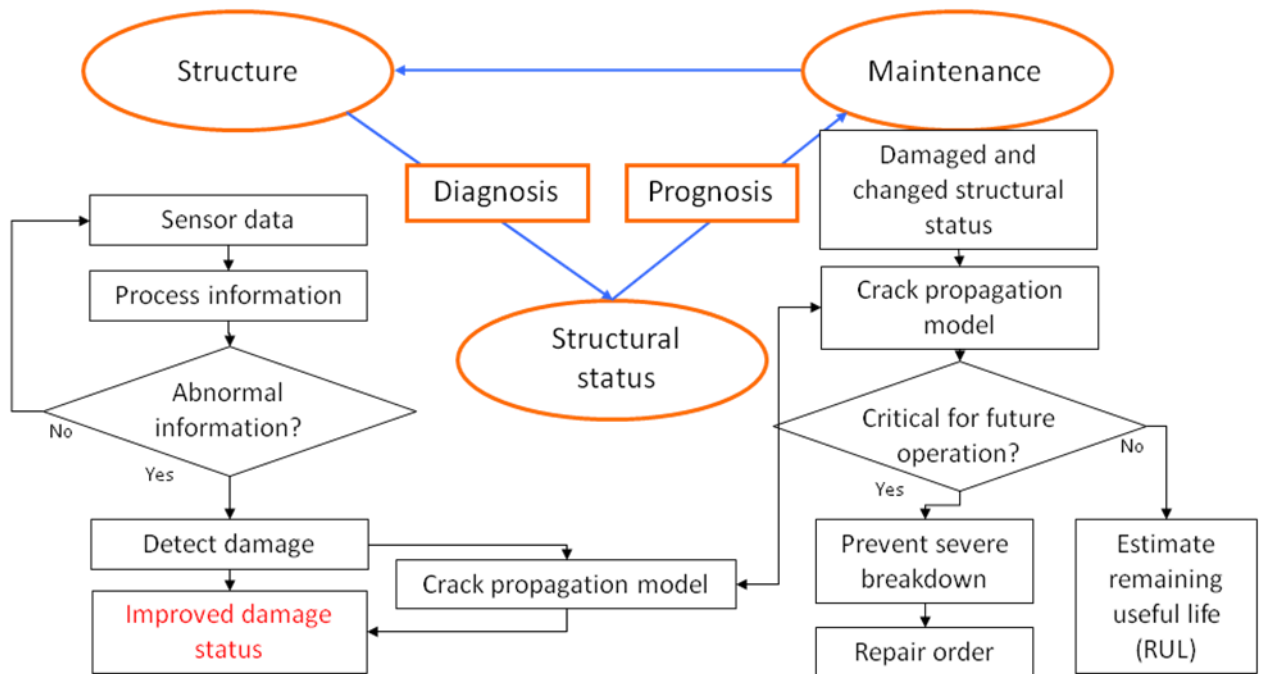


Figure 1-10. Applying crack propagation model to improve accuracy of detection results

### How to Achieve the Objective

Accurate location of the damage should be known prior to estimating damage severity. Chapter 3 explains migration technique, a popular method used to estimate the location of damage. Section 3.1 presents migration technique developed by Dr. Yuan. On the basis of what he has achieved, various approaches are described to improve the identification of crack location in Section 3.2 and 3.3.

One of the measures of damage severity is the length of a crack. This is essential information required to move on to the prognostic stage. There have been researches on increasing signal strength due to longer or bigger cracks. Chapter 4 describes the relation between crack size and signal amplitude by comparing simulation with experiment. Simulation tool described in Section 2.4 is provided by Dr. Yuan.

In Chapter 5, we assume a situation where we have measurement uncertainty, and we have to estimate the size from uncertain data. With a hypothetical SHM system, a simulation result of fuselage panel is presented. Section 5.2 explains how to apply Bayesian approach to this problem. The Bayesian approach for this application uses current inspection results to form a likelihood function and previous result to construct a prior distribution. By combining those two, a more accurate result can be obtained.

## CHAPTER 2 BASIC PRINCIPLES

For various active monitoring applications, structural wave propagation by piezoelectric actuator/sensor is often used. In this chapter, some basic concepts are introduced related to the wave propagation in plates and piezoelectric behavior. Section 2.1 discusses some issues related to Lamb wave propagation and the behavior of scattered wave from damage, and Section 2.2 discusses the behavior of piezoelectric materials with respect to the electric field applied to the actuators and strain applied to the sensors. Section 2.3 presents an example of exciting Lamb wave and detecting the scattered wave using a piezoelectric patch. Excitation of PZT material uses the actuation equation described in Section 2.2, propagation and scatter use the solution to the wave equation explained in Section 2.1, and sensing of electrical signal uses the sensing equation described in Section 2.2. By comparing the analytical approach to the experimental result, we found a good agreement in the shape of detected signals. Section 2.4 introduces a finite difference algorithm we have used to simulate the damage detection problem.

### **Lamb Wave Propagation in a Thin Plate**

#### **Wave Equation**

Lamb waves are structural ultrasonic waves that are guided between two parallel free surfaces. Two basic types of Lamb wave, symmetric and antisymmetric, can exist in the plate. The movement of a particle for symmetric Lamb wave resembles pressure wave, whereas it resembles shear wave for antisymmetric Lamb wave (Figure 2-1). Lamb waves are highly dispersive, and their speed depends on the product of

frequency and the plate thickness. This section explains the stress and strain behavior within a plate when Lamb waves induced by external excitation propagate within the plate.

First assume a simple case where we have an infinite plate with thickness  $2d$ , and the wave is propagating from the origin (Figure 2-1). To describe the displacement behavior of particles induced by wave propagation, Navier's governing equation [8] for equation of motion in cylindrical coordinates is as follows (No body forces):

$$\begin{aligned} (\lambda + \mu) \frac{\partial \Delta}{\partial r} + \mu \nabla^2 u_r - \mu \frac{u_r}{r^2} &= \rho \frac{\partial^2 u_r}{\partial t^2} \\ (\lambda + \mu) \frac{\partial \Delta}{\partial z} + \mu \nabla^2 u_z &= \rho \frac{\partial^2 u_z}{\partial t^2} \end{aligned} \quad (2-1)$$

Under the axisymmetric assumption, the equations can be described as  $\theta$ -invariant.  $\lambda$  and  $\mu$  are Lamé constants,  $\rho$  is density,  $\nabla = \frac{\partial}{\partial r} \mathbf{r} + \frac{\partial}{\partial z} \mathbf{k}$  is the gradient operator,  $\nabla^2 = \frac{1}{r} \frac{\partial}{\partial r} \left( r \frac{\partial}{\partial r} \right) + \frac{\partial^2}{\partial z^2}$  is the Laplace operator, and  $\Delta = \frac{\partial u_r}{\partial r} + \frac{u_r}{r} + \frac{\partial u_z}{\partial z}$  is the divergence term.

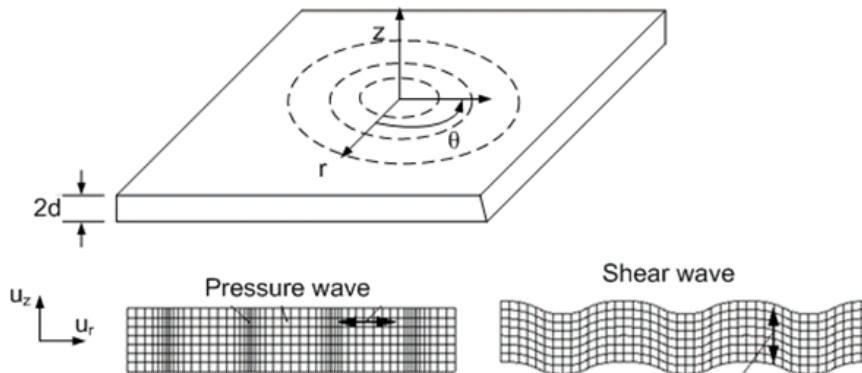


Figure 2-1. Axisymmetric structural waves in plates in cylindrical coordinates. It may be misleading, but  $u_z$  is present for the pressure wave because of the displacement induced by Poisson's ratio.



The speed for each mode of Lamb wave is described by:

$$c_L = \sqrt{\frac{\lambda + 2\mu}{\rho}} \quad (\text{pressure wave}) \quad (2-2)$$

$$c_T = \sqrt{\frac{\mu}{\rho}} \quad (\text{shear wave})$$

There are two independent solutions for the wave equation, each corresponds to pressure and shear wave, described by symmetric and antisymmetric modes, respectively. For each mode, the reference coordinates for the direction of particle motion are shown in Figure 2-2. Particle movement for the symmetric mode of Lamb wave is symmetric with respect to the mid plane of the plate, while it is opposite for the antisymmetric mode.

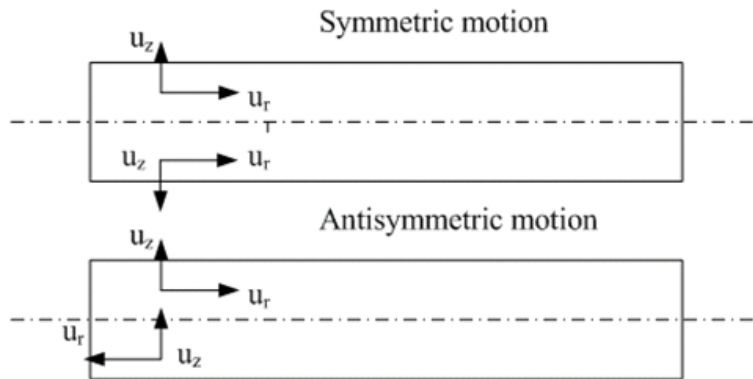


Figure 2-2. Symmetric and antisymmetric particle motion across the plate thickness

Wave number analysis decomposes the signal shape into the sum of cosine and sine waves in the form of  $u_z = e^{-i\omega t}$ . There exist many different angular frequencies for an excitation if the excitation is not a simple harmonic function, and each of them has a different solution. The solution of Eq.2-1 corresponding to the excitation  $u_z = e^{-i\omega t}$  is available in the literature [9,46,47]:

$$\begin{cases}
u_r = A^* \left[ -2k^2 q \cos qd \cos pz + q(k^2 - q^2) \cos pd \cos qz \right] J_1(kr) e^{-i\omega t} \\
u_z = A^* \left[ 2kpq \cos qd \cos pz + k(k^2 - q^2) \cos pd \cos qz \right] J_0(kr) e^{-i\omega t}
\end{cases} \quad (\text{Symmetric})$$

$$\begin{cases}
u_r = A^* \left[ -2k^2 q \sin qd \sin pz + q(k^2 - q^2) \sin pd \sin qz \right] J_1(kr) e^{-i\omega t} \\
u_z = A^* \left[ 2kpq \sin qd \sin pz + k(k^2 - q^2) \sin pd \sin qz \right] J_0(kr) e^{-i\omega t}
\end{cases} \quad (\text{Antisymmetric})$$

(2-3)

where  $A^*$  is an arbitrary constant calculated by applying initial and boundary conditions,

$$p = k \sqrt{1 - \left(\frac{c}{c_L}\right)^2}, q = k \sqrt{1 - \left(\frac{c}{c_T}\right)^2}, c = \frac{\omega}{k} \text{ is the phase velocity, } J_0, J_1 \text{ are Bessel functions, } \omega$$

is the angular frequency, and  $k$  is the wave number. For a general input signal, we have many different frequency components of  $\omega$  for modified wave number analysis.

Corresponding  $k$  are found by considering the wave velocity.

The solution in Eq.2-3 implies that the amplitude of a circular crested wave in a plate experiences a decay described by Bessel function in space.

One important property of Lamb wave is that there are several propagation modes. Each mode has different frequency due to different wave number, and the wave velocity can be calculated from its characteristic equations. To derive the characteristic equation, the traction free boundary conditions should be considered. The strain components induced by this displacement field are listed as follows:

$$\begin{aligned}
\varepsilon_{rr} &= \frac{\partial u_r}{\partial r} & \varepsilon_{r\theta} &= \frac{1}{2} \left( \frac{1}{r} \frac{\partial u_r}{\partial \theta} + \frac{\partial u_\theta}{\partial r} - \frac{u_\theta}{r} \right) \\
\varepsilon_{\theta\theta} &= \frac{1}{r} \frac{\partial u_\theta}{\partial \theta} + \frac{u_r}{r} & \varepsilon_{rz} &= \frac{1}{2} \left( \frac{\partial u_r}{\partial z} + \frac{\partial u_z}{\partial r} \right) \\
\varepsilon_{zz} &= \frac{\partial u_z}{\partial z} & \varepsilon_{\theta z} &= \frac{1}{2} \left( \frac{\partial u_\theta}{\partial z} + \frac{1}{r} \frac{\partial u_z}{\partial \theta} \right)
\end{aligned} \quad (2-4)$$

To introduce the boundary conditions for the upper and lower free surfaces of the plate, the stresses can be derived from:

$$\begin{aligned}\sigma_{zz} &= \lambda\Delta + 2\mu\varepsilon_{zz} \\ \sigma_{rz} &= 2\mu\varepsilon_{rz}\end{aligned}\tag{2-5}$$

Then, the characteristic equation for the symmetric and antisymmetric wave are obtained by applying  $\sigma_{zz}(d) = 0, \sigma_{rz}(d) = 0$ :

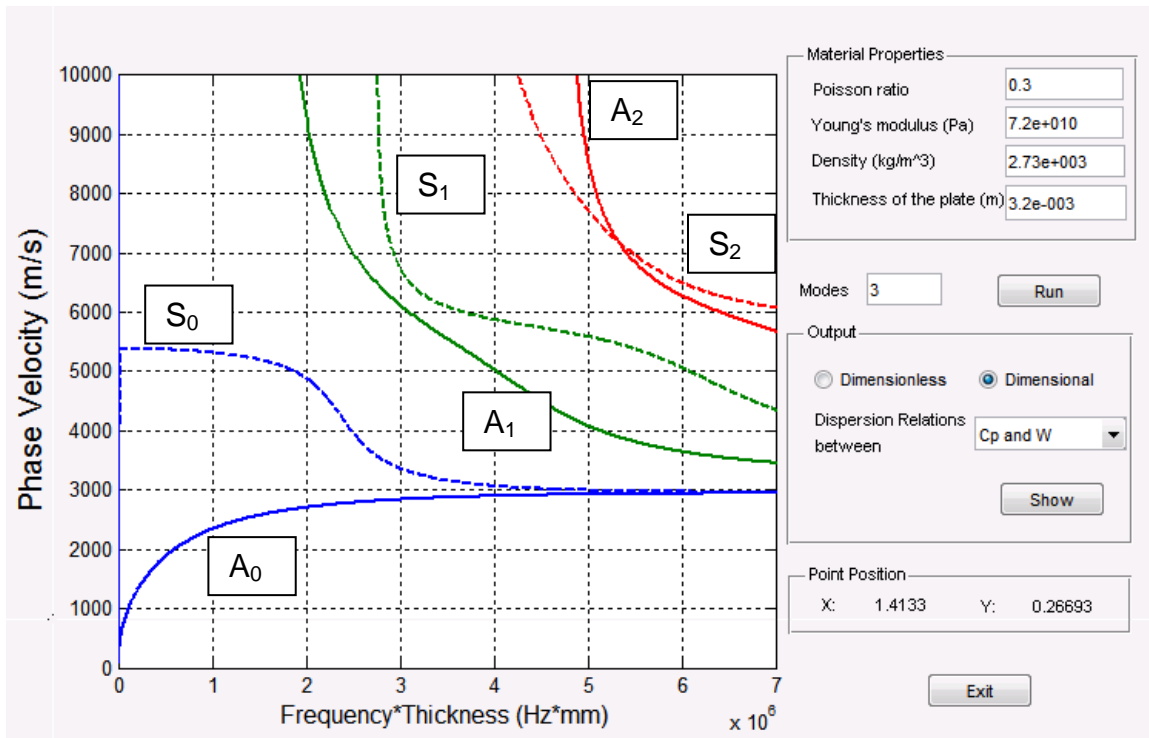
$$\begin{aligned}\frac{\tanh(iqd)}{\tanh(ipd)} &= -\frac{4pqk^2}{(k^2 - q^2)^2} && \text{(Symmetric)} \\ \frac{\tanh(iqd)}{\tanh(ipd)} &= -\frac{(k^2 - q^2)^2}{4pqk^2} && \text{(Antisymmetric)}\end{aligned}\tag{2-6}$$

There is another important property of the Lamb wave, which is the traveling speed of Lamb wave packets, such as the one limited by a Hann window. Hann window is a type of window function, which is zero-valued outside of some chosen interval. The traveling speed of Lamb wave packets is called the group velocity, and calculated from the phase velocity  $c$ .

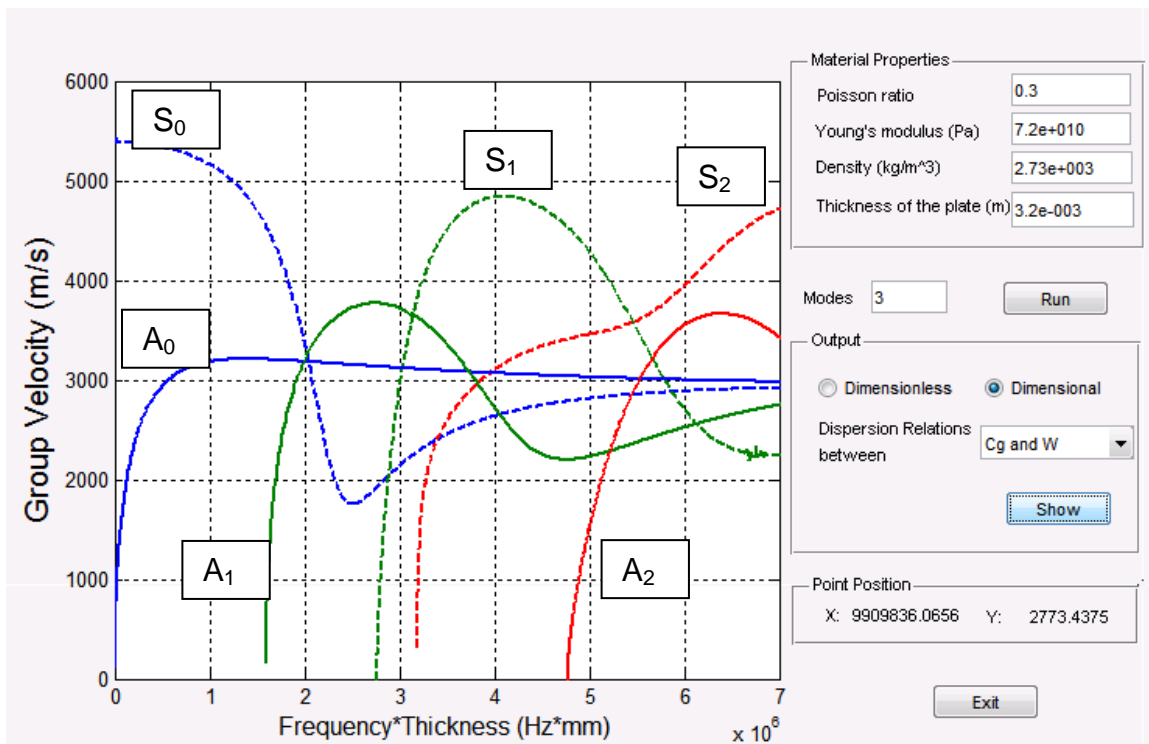
$$c_g = c^2 \left( c - \omega d \frac{\partial c}{\partial(\omega d)} \right)^{-1}\tag{2-7}$$

The wave speed dispersion curves in an aluminum plate are shown in Figure 2-3. The figure is generated using Lambwave\_UI developed by Yuan et al [55].

From Figure 2-3, we know that the wave velocity depends on the frequency. The relationship between wave velocities in the plate and frequency is inherent material properties. The wave propagation analysis depends on the wave velocity, which is used to calculate the wave number for the corresponding propagation mode.



A



B

Figure 2-3. Typical wave speed dispersion curves for symmetric and antisymmetric waves. A) Phase velocity B) Group velocity

## Wave Scatter

When a Lamb wave hits a defect, it scatters around the defect as if the defect is a secondary source. The amplitude of scattered wave depends on the direction, mode (symmetric or antisymmetric), wave number, and frequency. The simplest way to model the scatter from an arbitrary shaped damage is by analyzing an infinitesimal cavity in the wave propagation path, and using Huygen's principle [48] to model the wave front and corresponding amplitude. Huygen's principle for reflection describes the scattered or diffracted wave as a sum of reflections from many secondary sources on the reflection boundary. Consider a small cavity of radius  $a$  standing in the path of the wave propagation, as shown in Figure 2-4.

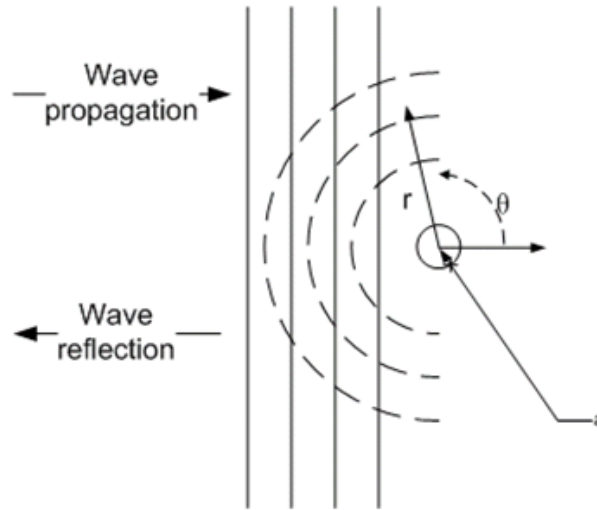


Figure 2-4. Wave reflection from a small cavity

The equation of motion for a simple wave is:

$$\nabla^2 u_r - \frac{1}{c_T^2} \ddot{u}_r = 0$$

$$\text{where } \nabla^2 u_r = \frac{1}{r} \frac{\partial}{\partial r} \left( r \frac{\partial u_r}{\partial r} \right) + \frac{1}{r^2} \frac{\partial^2 u_r}{\partial \theta^2} \quad (2-8)$$

In this case, both the incident wave and scattered wave exist. Denoting the displacement field induced by incident wave as  $u_i$  and scattered wave as  $u_s$ , the displacement field is given by  $u_r = u_i + u_s$ .

The incident wave can be expressed through Bessel function [49]:

$$u_i = \sum_{n=0}^{\infty} U_0 \varepsilon_n (-1)^n J_n(kr) \cos n\theta \quad (\varepsilon_0 = 1, \varepsilon_n = 2) \quad (2-9)$$

where  $J_n(kr)$  are the Bessel functions,  $U_0$  is a constant related to the magnitude of the incident wave, and  $k = \omega/c$  is the wave number.

When the incident wave interacts with the cavity, a scattering field will result.

Substituting the scattered wave  $u_s = U_s(r, \theta)e^{i\omega t}$  to Eq. 2.8., the solution for the wave equation for the scattered wave can be written as [47]:

$$u_s(r, \theta) = \left( \sum_{n=0}^{\infty} A_n H_n^{(2)}(kr) \cos n\theta \right) e^{i\omega t} \quad (2-10)$$

To find the coefficients  $A_n$ , we need to consider the traction-free boundary conditions on the cavity surface:

$$\begin{cases} \sigma_{rr} = \sigma_{r\theta} = \sigma_{\theta\theta} = 0 \\ \frac{\partial \mathbf{u}}{\partial r} = 0 \end{cases} \quad \text{at } r = a$$

$$\sigma_{rr} = \lambda \left( \frac{\partial u_r}{\partial r} + \frac{1}{r} \frac{\partial u_\theta}{\partial \theta} + \frac{u_r}{r} \right) + 2\mu \frac{\partial u_r}{\partial r}$$

$$\sigma_{\theta\theta} = \mu \left( \frac{1}{r} \frac{\partial u_r}{\partial \theta} + \frac{\partial u_\theta}{\partial r} - \frac{u_\theta}{r} \right) \quad (2-11)$$

The total displacement field  $u_r = u_i + u_s$  should satisfy the boundary conditions.

$$\frac{\partial u_i}{\partial r} + \frac{\partial u_s}{\partial r} = 0 \quad \text{at } r = a$$

$$\sum_{n=0}^{\infty} \left\{ U_0 \varepsilon_n (-1)^n \frac{dJ_n(kr)}{dr} + A_n \frac{dH_n^{(2)}(kr)}{dr} \right\} \cos n\theta = 0 \quad (2-12)$$

Because functions  $\cos n\theta$  are orthogonal, we find the coefficient values  $A_n$  from Eq.2-10 as follows:

$$A_n = \frac{U_0 \varepsilon_n (-1)^n J_n'(ka)}{H_n^{(2)}(ka)} \quad (2-13)$$

The scattered field has the form of Eq.2-10 with coefficients in Eq.2-13. In the far field, using an asymptotic expression, the result can be written as:

$$u_s(r, \theta, t) = U_0 \sqrt{\frac{2}{\pi kr}} \exp\{i(\omega t - kr)\} S(\theta) \quad (2-14)$$

This implies that the wave decays with respect to time, and the amplitude is proportional to  $1/\sqrt{kr}$ . Also, the amplitudes depends on the angle via  $S(\theta)$ . There is no general analytical solution for  $S(\theta)$ , but it can be calculated numerically. Graff has shown several numerical results of the structural wave scattering [49] when the size of cavity is of the same order of magnitude with the wavelength.

### **Piezoelectric Materials**

Piezoelectricity, by definition, is a property of certain materials to physically deform in the presence of an electric field or, conversely, to produce an electric charge when mechanically deformed. There are a wide variety of materials that exhibit this phenomenon. When we applied electrical field to those materials for polarization, the material becomes permanently elongated in the direction of the poling field (polar axis) and correspondingly reduced in the transverse direction. Applying a voltage in the direction of the poling voltage produces further elongation along the axis and a corresponding contraction in the transverse direction obtained from its Poisson's ratio.

## Actuation Equation

Piezoelectric material couples the electrical and mechanical effects through the piezoelectric constitutive equations. The ability to generate mechanical strain from applied electric field is modeled using actuation equation in polar coordinates [8]:

$$\begin{aligned}\varepsilon_{rr} &= s_{rr}^E \sigma_{rr} + s_{r\theta}^E \sigma_{\theta\theta} + d_{3r} E_3 \\ \varepsilon_{\theta\theta} &= s_{r\theta}^E \sigma_{rr} + s_{\theta\theta}^E \sigma_{\theta\theta} + d_{3\theta} E_3\end{aligned}\tag{2-15}$$

where  $\varepsilon$  is the mechanical strain,  $\sigma$  is the stress,  $E$  is the electric field applied to the piezoelectric material,  $s^E$  is the mechanical compliance of the material measured at zero electric field ( $E=0$ ), and  $d$  is a material property representing the piezoelectric coupling effect.

The remainder of this section will derive the displacement field generated by a circular piezoelectric actuator attached on a plate. Consider an isotropic circular piezoelectric actuator (Figure 2-5), which undergoes uniform radial and circumferential expansion, the strain-displacement relation in polar coordinates reduces to:

$$\begin{aligned}\varepsilon_{rr} &= \frac{\partial u_r}{\partial r} \\ \varepsilon_{\theta\theta} &= \frac{u_r}{r} \\ \varepsilon_{r\theta} &= 0\end{aligned}\tag{2-16}$$

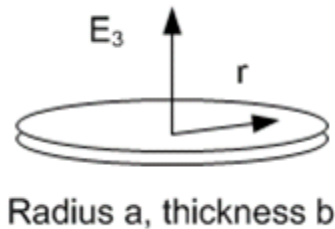


Figure 2-5. Circular piezoelectric actuator



The piezoelectric coupling constant and mechanical compliance are identical in planar directions (orthogonal to polarization direction):

$$\begin{aligned} d_{3r} &= d_{3\theta} = d_{31} \\ s_{rr}^E &= s_{\theta\theta}^E = s_{11}^E, \quad s_{r\theta}^E = s_{12}^E \end{aligned} \quad (2-17)$$

where subscript 3 denotes the z-direction (polarization)

Solving Eq.2-15 for  $\sigma$  yields:

$$\begin{aligned} \sigma_{rr} &= \frac{\varepsilon_{rr} + \nu\varepsilon_{\theta\theta} - (1+\nu)d_{31}E_3}{s_{11}^E(1-\nu^2)} \\ \sigma_{\theta\theta} &= \frac{\nu\varepsilon_{rr} + \varepsilon_{\theta\theta} - (1+\nu)d_{31}E_3}{s_{11}^E(1-\nu^2)} \end{aligned} \quad (2-18)$$

where  $\nu$  is the Poisson ratio defined as  $\nu = -\frac{s_{12}^E}{s_{11}^E}$ . By the displacement-strain

relationship in Eq.2-16, the stresses can be expressed in terms of displacements:

$$\begin{aligned} \sigma_{rr} &= \frac{1}{s_{11}^E(1-\nu^2)} \left[ \frac{\partial u_r}{\partial r} + \nu \frac{u_r}{r} - (1+\nu)d_{31}E_3 \right] \\ \sigma_{\theta\theta} &= \frac{1}{s_{11}^E(1-\nu^2)} \left[ \nu \frac{\partial u_r}{\partial r} + \frac{u_r}{r} - (1+\nu)d_{31}E_3 \right] \end{aligned} \quad (2-19)$$

Newton's law of motion applied to an infinitesimal element yields:

$$\frac{d\sigma_{rr}}{dr} + \frac{\sigma_{rr} - \sigma_{\theta\theta}}{r} = -\omega^2 \rho u_r \quad (2-20)$$

Therefore, the following wave equation can be obtained:

$$\frac{1}{s_{11}^E(1-\nu^2)} \left[ \frac{d^2 u_r}{dr^2} + \frac{1}{r} \frac{du_r}{dr} - \frac{u_r}{r^2} \right] = -\omega^2 \rho u_r \quad (2-21)$$

Using the wave velocity  $c_p = \sqrt{\frac{1}{\rho s_{11}^E(1-\nu^2)}}$  and the wave number  $k = \omega/c_p$ , the

equation becomes:

$$r^2 \frac{d^2 u_r}{dr^2} + r \frac{du_r}{dr} + (k^2 r^2 - 1) u_r = 0 \quad (2-22)$$

which is the Bessel differential equation of order 1. The general solution for Eq.2-22 is:

$$u_r(r) = A \cdot J_1(kr) \quad (2-23)$$

The constant  $A$  is determined from boundary conditions. For stress-free boundary conditions at  $r=r_a$ , we have:

$$\begin{aligned} \sigma_{rr}(r_a) &= \frac{1}{s_{11}^E(1-\nu^2)} \left[ \frac{\partial u_r}{\partial r} + \nu \frac{u_r}{r} - (1+\nu)d_{31}E_3 \right] = 0 \\ AkJ_1'(kr_a) + \frac{\nu}{a} AJ_1(kr_a) &= (1+\nu)d_{31}E_3 \\ A &= \frac{(1+\nu)r_a d_{31}E_3}{kr_a J_0(kr_a) - (1-\nu)J_1(kr_a)} \end{aligned} \quad (2-24)$$

So the displacement induced by circular piezoelectric actuator is:

$$u_r(r) = \frac{(1+\nu)J_1(kr)}{kr_a J_0(kr_a) - (1-\nu)J_1(kr_a)} r_a d_{31}E_3 \quad (2-25)$$

This implies that at a given radial location, the displacement amplitude is proportional to the applied electric field. Many manufacturers of piezoelectric devices provide wide range of linearity that this relation can be applied within its normal operation condition.

### Sensing Equation

Similarly, piezoelectric materials respond to mechanical strain to generate electric field within them. The process of generating electric field from stress is described by sensing equation [8]:

$$E_3 = g_{3r}\sigma_{rr} + g_{3\theta}\sigma_{\theta\theta} + \beta_{3k}^T D_k \quad (2-26)$$

where  $g_{ij}$  is the piezoelectric voltage coefficient and represents how much electric field is induced per unit stress,  $D$  is the electrical displacement (charge per unit area), and  $\beta_{jk}$  is the inverse of the permittivity coefficient  $e$ .

The piezoelectric coefficients have following identities:

$$\begin{aligned} g_{iq} &= \beta_{ik}^T d_{kq} \\ d_{ip} &= e_{ik}^T g_{kp} \\ \beta_{ik}^T e_{kj}^T &= \delta_{ij} \end{aligned} \quad (2-27)$$

Consider an isotropic disc, Eq. 2.26 can be stated as:

$$D_3 = d_{31}\sigma_{rr} + d_{31}\sigma_{\theta\theta} + e_{33}^T E_3 \quad (2-28)$$

Then recall Eq.2-19,

$$\begin{aligned} \sigma_{rr} &= \frac{1}{s_{11}^E(1-\nu^2)} \left[ \frac{\partial u_r}{\partial r} + \nu \frac{u_r}{r} - (1+\nu)d_{31}E_3 \right] \\ \sigma_{\theta\theta} &= \frac{1}{s_{11}^E(1-\nu^2)} \left[ \nu \frac{\partial u_r}{\partial r} + \frac{u_r}{r} - (1+\nu)d_{31}E_3 \right] \end{aligned} \quad (2-29)$$

Substituting this to Eq.2-28,

$$D_3 = \frac{d_{31}}{s_{11}^E(1-\nu)} \left[ \frac{1}{r} \frac{d}{dr} (ru_r) \right] - \left( \frac{2d_{31}^2}{s_{11}^E(1-\nu)} - e_{33}^T \right) E_3 \quad (2-30)$$

Eq.2-30 defines the relation between induced displacement  $u_r$  and electrical field generated in piezoelectric sensor. If there is no external electric field, the electric displacement within the piezoelectric dipole can be described with the first term of Eq.2-30. Note that  $u_z$  is the dominant particle movement, but the stress applied to the PZT sensor is related only to  $u_r$ . To obtain the voltage from the electric displacement, the charge is obtained by integrating  $D$ , and by dividing with capacitance of the PZT sensor, we can obtain the voltage difference.

$$V = \frac{Q}{C} = \frac{\int D_3 dz}{C} \quad (2-31)$$

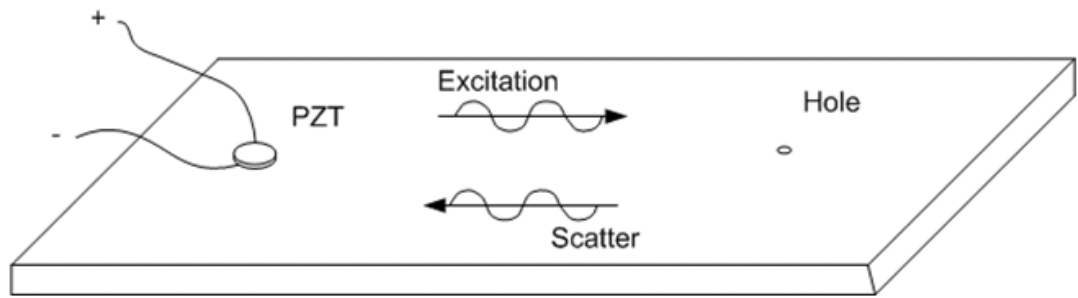
However, the stress field within the piezoelectric sensor is not uniform and not easy to analyze. Assuming the size of PZT sensors is smaller than the wavelength, we can use a pin-point approximation for the sensor for the central displacement [8].

### **Analytical Solution to a Toneburst Excitation**

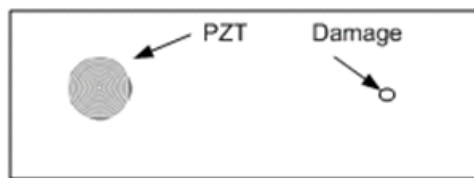
An analytical analysis on the problem of flaw detection should include all the previous concepts to explain the wave behavior. To summarize all the basic concepts to simulate a problem of flaw detection, a practical example is introduced in this section. In an infinite plate with thickness 3.2 mm, one PZT actuator is attached at the origin of the plate, and the signal is obtained at the same position. We excite the plate using a toneburst signal for successful generation of Lamé wave of 110 kHz. 110 kHz is determined to have the maximum response for  $A_0$  wave from the experiment (Also explained in Chapter 4). The dimensions and material properties of PZT actuator are listed in Table 2-1. It is assumed that there is one through-the-thickness hole of 2 mm diameter, located 113.4 mm from the PZT center.

The procedure to find an analytical solution to the problem is shown in Figure 2-6B.

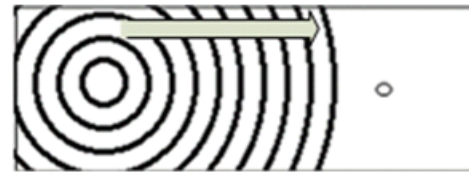
When we apply voltage to the PZT actuator, it generates displacement field by actuation equation (Eq.2-15). Wave propagates the space between the actuator and damage, and the displacement field is described by wave propagation equation (Eq.2-3). When the wave hits the damage, it is scattered and the scattered wave solution is found using Eq.2-10. Finally, the PZT sensor detects the scattered wave, and it generates electric signal described by the sensing equation (Eq.2-25).



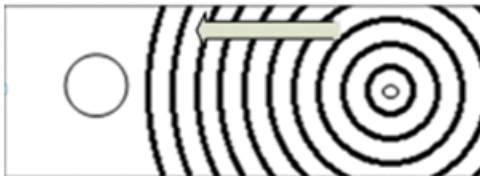
A



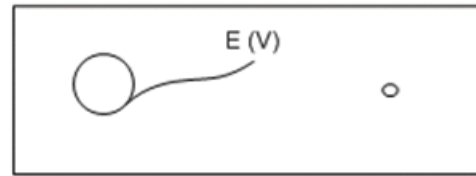
1. Displacement field generation within the PZT actuator



2. Lamb wave generation, induced displacement field



3. Scattered wave from the damage



4. Voltage generation from strain at the PZT sensor

B

Figure 2-6. Hole detection problem. A) Problem layout B) Flowchart for analysis

Table 2-1. Properties of piezoelectric disc (modified PZT-4)

Geometry (mm)	diameter:10.0, thickness:0.4
Density $\rho$ (kg/m <sup>3</sup> )	$7.9 \times 10^3$
Young's modulus E (GPa)	$E_{11}: 86, E_{33}: 73$
piezoelectric coefficient $d_{31}$ (m/V)	$-140 \times 10^{-12}$
Piezoelectric coefficient $d_{33}$ (m/V)	$320 \times 10^{-12}$
Piezoelectric coefficient $g_{31}$ (Vm/N)	$-11 \times 10^{-3}$
Piezoelectric coefficient $g_{33}$ (Vm/N)	$25 \times 10^{-3}$
Dielectric constant $K_3$	1400

We review only the fundamental  $A_0$  mode in this section. Similar analysis can be made for higher antisymmetric modes or symmetric modes by changing the wave velocity to corresponding mode. The excitation signal is 5 count toneburst shown in

Figure 2-7 and Eq.2-32. The sampling frequency is 5 MHz.

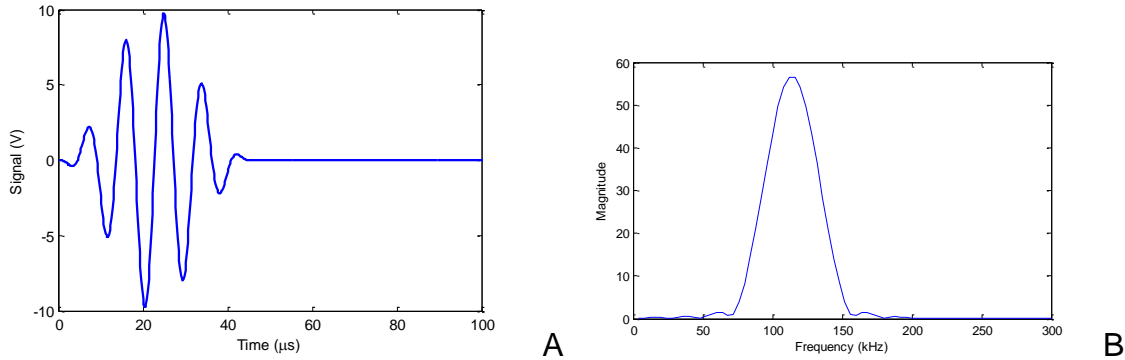


Figure 2-7. Five peaked toneburst excitation sent to the actuator (110 kHz) A) Time domain, B) Frequency domain

$$V_{in}(t) = 10 \left[ H(t) - H\left(\frac{t-5}{f_c}\right) \right] \left( 1 - \cos \frac{2\pi f_c t}{5} \right) \sin 2\pi f_c t \quad (2-32)$$

where  $H(t)$  is the Heaviside step function,  $f_c=110$  kHz is the central frequency. The frequency domain signal is obtained by discrete Fourier transform applying to the time domain signal.

$$V_{in}(t) = \sum_{n=0}^{N-1} A_n e^{in\omega t} \quad (2-33)$$

The solution provided in this section uses harmonic analysis. To calculate discrete Fourier transform, FFT (fast-Fourier transform) algorithm is used to calculate the frequency domain coefficients. Considering an infinite time domain, the transformed signal is actually a collection of infinite tonebursts. However, since our assumption is an infinite plate, the effect of excitation before zero time will be banished if we adjust the signal length long enough. From Figure 2-7, we have nonzero frequency component up to 220 kHz, and from FFT, this corresponds to 44 frequency components to represent the wave accurately at given sampling frequency.

First, we will calculate the displacement field induced by applied voltage. We will use actuation equation, but we cannot use Eq.2-25 directly since the PZT actuator is attached to the aluminum plate. When the PZT is mounted on the structure, its circumference is elastically constrained by the dynamic structural stiffness of the structure (Figure 2-8).

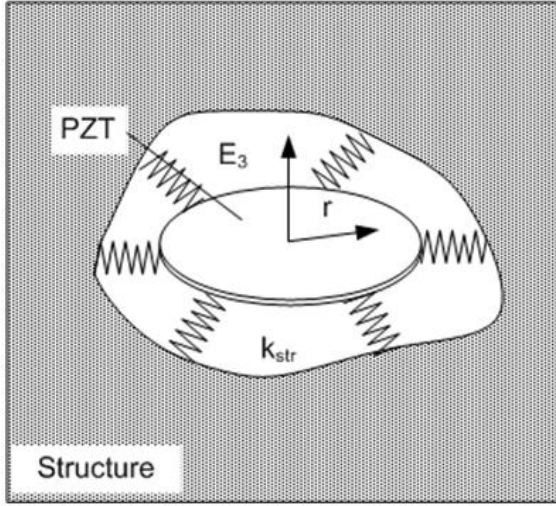


Figure 2-8. PZT actuator attached to an aluminum plate

At the boundary  $r=r_a$ , we have the following boundary condition [8]:

$$\sigma_{rr}(r_a) = \frac{k_{str}(\omega)u_r(r_a)}{t_a} \quad (2-34)$$

where  $k_{str}(\omega)$  is the dynamic structural stiffness.

Applying Eq.2-34 to the boundary condition given in Eq.2-24 gives,

$$\sigma_{rr}(r_a) = \frac{1}{s_{11}^E(1-\nu^2)} \left[ \frac{\partial u_r}{\partial r} + \nu \frac{u_r}{r} - (1+\nu)d_{31}E_3 \right] = \frac{k_{str}(\omega)u_r(r_a)}{t_a} \quad (2-35)$$

$$\frac{\partial u_r}{\partial r} + \nu \frac{u_r}{r} - (1+\nu)d_{31}E_3 = \frac{k_{str}(\omega)u_r(r_a)}{k_{PZT}r_a}$$

where  $k_{PZT} = \frac{t_a}{r_a s_{11}^E(1-\nu^2)}$  is the stiffness of PZT.

With the condition, the solution to the PZT excitation problem (Eq.2-25) changes

to:

$$u_r(r) = \frac{(1+\nu)J_1(kr)}{kr_a J_0(kr_a) - (1-\nu + \chi(1+\nu))J_1(kr_a)} r_a d_{31} E_3 \quad (2-36)$$

where  $\chi = k_{str} / k_{PZT}$  is the stiffness ratio between PZT and aluminum plate.

By applying  $E_3(t) = V_{in}(t) / t_a$  to Eq.2-36, the displacement field induced by the toneburst can be found as shown in Figure 2-9.

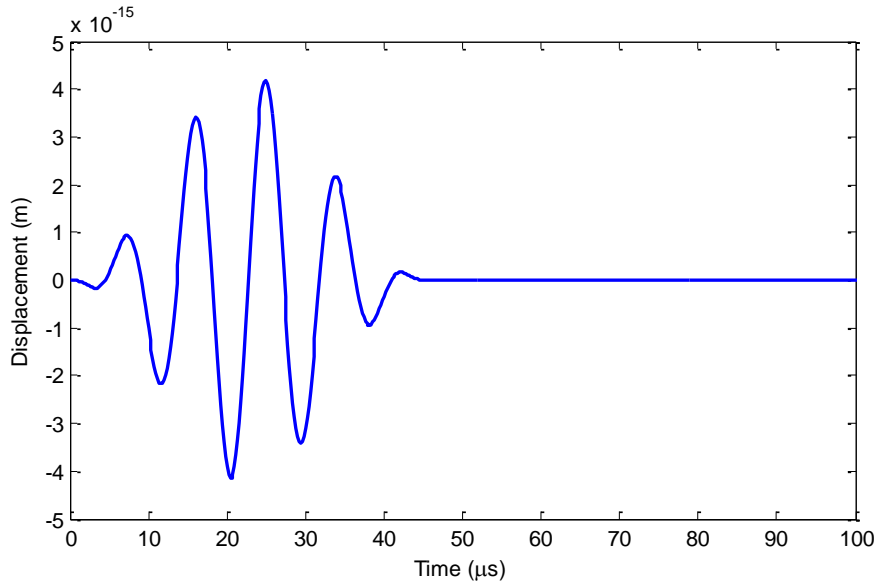


Figure 2-9. Displacement at the boundary of the PZT ( $r=a$ )

Secondly, the displacement introduced by the PZT transforms into structural Lamb wave described by Eq.2-3. Since we are interested the displacement at  $z=d$  (the surface where the PZT actuator is attached), the equation for this specific example can be rewritten as:

$$u_r(t)|_{z=d} = -A^* q (k^2 + q^2) \sin pd \sin qd J_1(kr) e^{-i\omega t} \quad (2-37)$$



where  $A_n^* = \frac{-A_n}{2kq \sin qd (q^2 - p^2)}$ , and  $A_n$  can be obtained by applying FFT to the

displacement  $u_r$  which is calculated by Eq.2-36.

Eq.2-37 gives the response to each frequency component. Inverse FFT (iFFT) is used to retrieve the time domain signal. The wave propagation in the plate is shown with respect to the distance (Figure 2-10A) and time (Figure 2-10B).

The incident wave that reaches to the damage is described by fixing  $r=113.4$  mm in Eq.2-35. At  $r=113.4$  mm, the displacement field changing in time can be described as Figure 2-10B.

The third step is calculating the scattered wavefield. To analyze the scattering behavior, we change our coordinate system centered at the cavity. Then, the incident wavefield to the damage and the scattered wavefield from the damage are found using Eq.2-9, 2.10 and Eq.2-13:

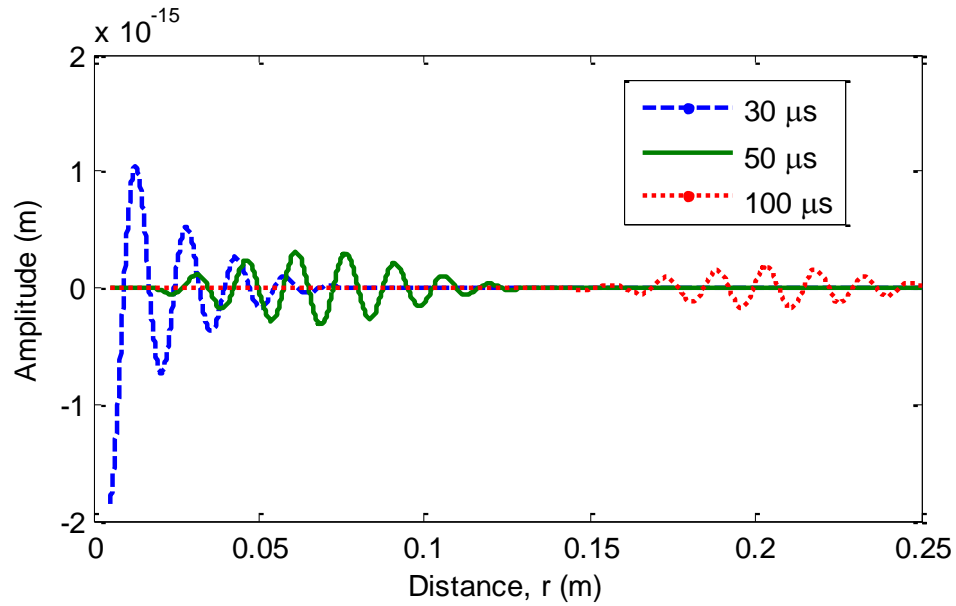
$$u_i = \sum_{n=0}^{\infty} U_0 \varepsilon_n (-1)^n J_n(kr) \cos n\theta$$

$$u_s(r, \theta) = \left( \sum_{n=0}^{\infty} A_n H_n^{(2)}(kr) \cos n\theta \right) e^{i\omega t} \quad (2-38)$$

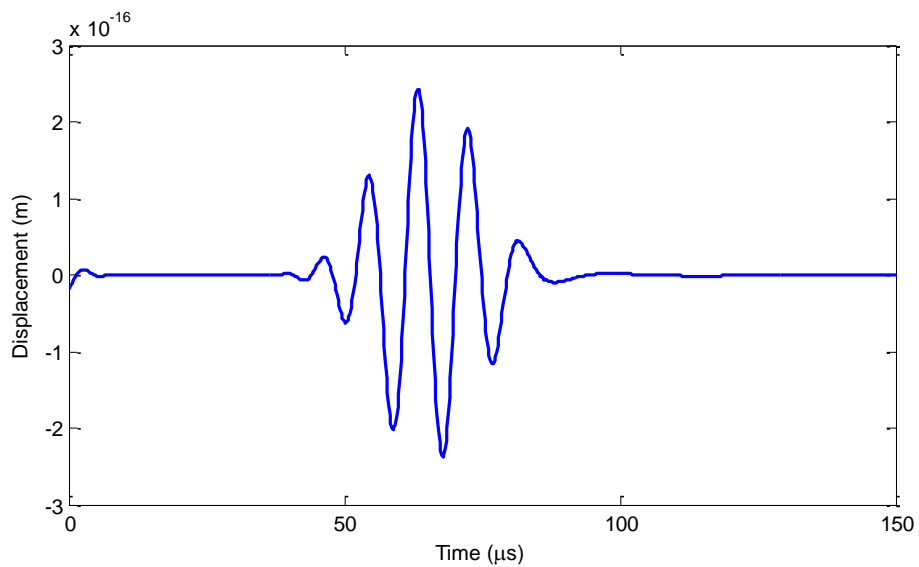
$$\text{where } A_n = \frac{U_0 \varepsilon_n (-1)^n J_n'(ka)}{H_n^{(2)}(ka)}$$

The coefficients  $U_0$  are found by applying discrete Fourier transform to the signal described by Figure 2-10B. Since this is an analytical expression for a single  $\omega$ , we apply FFT to the incident wave to transform the signal into frequency domain.

Accordingly, the coefficients  $A_n$  can be found from Eq.2-38, then we have the frequency response. Then the result is transformed into time domain signal using iFFT, and Figure 2-11 shows the scattered wavefield obtained at the sensor ( $r=113.4$  mm).



A



B

Figure 2-10. Displacement field induced by the piezoelectric actuation. A) In space B) In time (at  $r=100$  mm)

We assumed that there is no energy loss in reflection for simplicity. Note that the coordinate system is centered at the cavity for the scattered wavefield.

When the scattered wave hits the sensor, the piezoelectric disc generates electric field and the voltage difference between electrodes is measured (Figure 2-12).

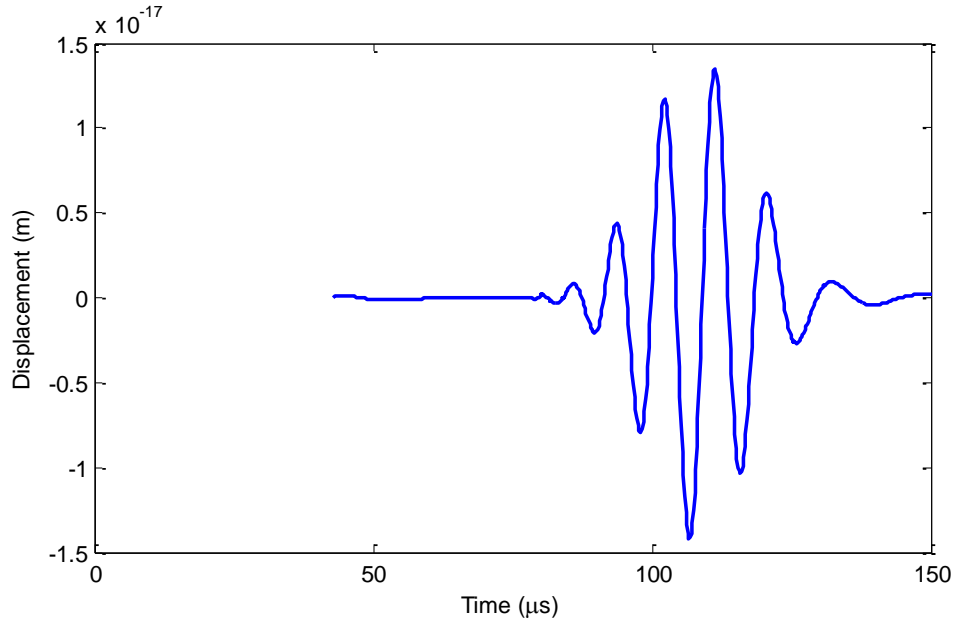


Figure 2-11. Scattered displacement response at  $r=113.4$  mm from the cavity center.

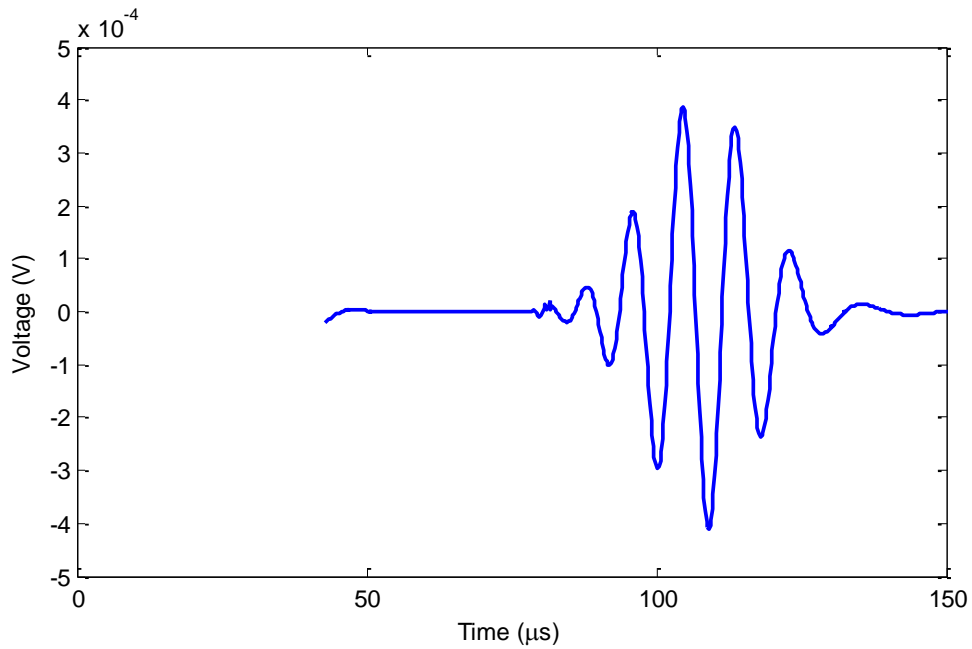


Figure 2-12. Electric signal obtained at the sensor position

Since the coefficients  $g_{ij}$  are given by the manufacturer, we can apply the sensing equation (Eq.2-26) directly to obtain the voltage as shown in Eq.2.39.

$$E_3 = \left( 1 + 2 \frac{g_{31} d_{31}}{s_{11}^E (1-\nu)} \right)^{-1} \frac{g_{31}}{s_{11}^E (1-\nu)} \left[ \frac{\partial u_r}{\partial r} + \frac{u_r}{r} \right] \quad (2-39)$$

The displacement field  $u_r$  is evaluated at  $r=113.4$  mm, which is the position of the sensor with respect to the cavity. Since we cannot assume an axisymmetric condition for the sensing problem, this is a rough approximation of stress field within the corresponding PZT sensor. Also, the PZT sensor is not small enough compared to the wavelength (27mm), so there may be errors due to this approximation.

In Chapter 4, we have some experimental results for a damage detection problem using PZT actuator and sensors. To verify this analytical solution, we compared the generated voltage with experimental data that has identical configuration. Figure 2-13 shows the comparison between experimental signal and analytical solution.

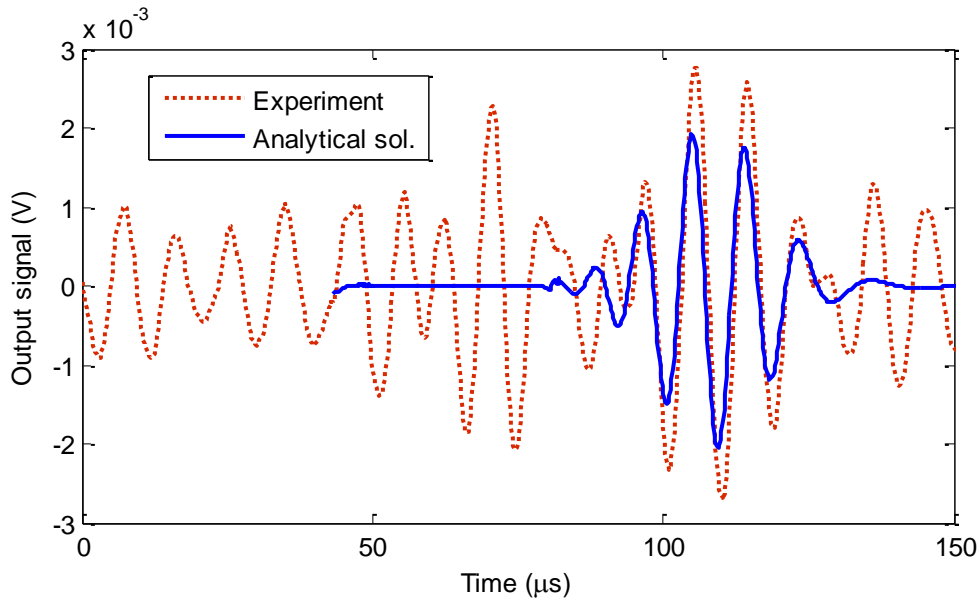


Figure 2-13. Comparison with experimental data

The experimental data includes  $S_0$  mode and  $A_0$  mode simultaneously, and the SNR (signal-to-noise ratio) is small because the scattered signal is weak. The experimental signal has a SNR of three (4.7 dB, infinity norm). Also, the experiment

includes boundary reflections because it is not an infinite plate. However, if we concentrate only the  $A_0$  mode, it is relatively easy to find the peak location and signal shape corresponding to the experimental data.

### Wavefield Simulation [51, 54]

Although the analytical solution is available for the structural wave propagation problem, it is not always efficient to evaluate analytical solution. Since our damage configurations are changing, we used a finite difference algorithm to simulate wave propagation and scatter. This section introduces the finite difference algorithm we used, which is developed in Matlab by Yuan et al. [51, 54]

### Governing Equations of Flexural Waves

The governing equations of flexural waves are formulated, in this subsection, as a first-order system that models the waves using a finite difference scheme, described in the next subsection. Using the stress resultants ( $Q_x$ ,  $Q_y$ ,  $M_x$ ,  $M_y$ , and  $M_{xy}$ ) and the plate displacement components ( $u$ ,  $\psi_x$ , and  $\psi_y$ ), the equations of motion can be written as:

$$\begin{aligned} \frac{\partial Q_x}{\partial x} + \frac{\partial Q_y}{\partial y} + q &= \rho h \frac{\partial^2 u}{\partial t^2} \\ \frac{\partial M_x}{\partial x} + \frac{\partial M_{xy}}{\partial y} - Q_x &= \frac{\rho h^3}{12} \frac{\partial^2 \psi_x}{\partial t^2} \\ \frac{\partial M_{xy}}{\partial x} + \frac{\partial M_y}{\partial y} - Q_y &= \frac{\rho h^3}{12} \frac{\partial^2 \psi_y}{\partial t^2} \end{aligned} \quad (2-40A)$$

and the constitutive equations:

$$\begin{Bmatrix} M_x \\ M_y \\ M_{xy} \end{Bmatrix} = D \begin{bmatrix} 1 & \nu & 0 \\ \nu & 1 & 0 \\ 0 & 0 & \frac{1-\nu}{2} \end{bmatrix} \begin{Bmatrix} \frac{\partial \psi_x}{\partial x} \\ \frac{\partial \psi_y}{\partial y} \\ \frac{\partial \psi_x}{\partial y} + \frac{\partial \psi_y}{\partial x} \end{Bmatrix}$$

$$Q_x = \kappa^2 Gh \left( \frac{\partial u}{\partial x} + \psi_x \right) \quad (2-40B)$$

$$Q_y = \kappa^2 Gh \left( \frac{\partial u}{\partial y} + \psi_y \right)$$

In Eq.2-40, E and G are Young's modulus and shear modulus respectively,  $q$  is the transverse loading applied to the plate,  $h$  is the plate thickness,  $\nu$  is the Poisson's ratio,  $\rho$  is the mass density,  $\kappa$  is a shear correction factor,  $\kappa^2 = \pi^2/12$ , and

$D = Eh^3 / [12(1-\nu^2)]$  is the flexural rigidity. Substituting the plate stress resultants in Eq.2-40B into Eq.2-40A, the equations of motions in terms of plate displacement components can be obtained. Then, by eliminating  $\psi_x$  and  $\psi_y$  from the three motion equations, a single differential equation in terms of transverse displacement  $u$  can be written as:

$$\left( \nabla^2 - \frac{\rho}{G'} \frac{\partial^2}{\partial t^2} \right) \left( D \nabla^2 - \frac{\rho h^3}{12} \frac{\partial^2}{\partial t^2} \right) u + \rho h \frac{\partial^2 u}{\partial t^2} = \left( 1 - \frac{D \nabla^2}{G' h} - \frac{\rho h^2}{12 G'} \frac{\partial^2}{\partial t^2} \right) q(x, y, t) \quad (2-41)$$

where  $G' = \kappa^2 G$ . When the wave number is small and the thickness of the plate is substantially smaller than the wavelength, Eq.2-41 can be approximated by

$$D \nabla^4 u + \rho h \frac{\partial^2 u}{\partial t^2} = q(x, y, t) \quad (2-42)$$

Defining  $\mathbf{u}^T = \{\dot{u}, \psi_x, \psi_y, Q_y, Q_x, M_x, M_y, M_{xy}\}$ ,  $\mathbf{q}^T = \{q, 0, 0, 0, 0, 0, 0, 0\}$  and differentiating

Eq.2-40B, the result can be rewritten in the matrix form:

$$\mathbf{E}_0 \frac{\partial \mathbf{u}}{\partial t} = \mathbf{A}_0 \frac{\partial \mathbf{u}}{\partial x} + \mathbf{B}_0 \frac{\partial \mathbf{u}}{\partial y} + \mathbf{C}_0 \mathbf{u} + \mathbf{q} \quad (2-43)$$

where

$$\mathbf{E}_0 = \begin{bmatrix} \rho h & 0 & 0 & 0 & 0 & 0 & 0 & 0 \\ 0 & \frac{\rho h^3}{12} & 0 & 0 & 0 & 0 & 0 & 0 \\ 0 & 0 & \frac{\rho h^3}{12} & 0 & 0 & 0 & 0 & 0 \\ 0 & 0 & 0 & \frac{1}{\kappa^2 Gh} & 0 & 0 & 0 & 0 \\ 0 & 0 & 0 & 0 & \frac{1}{\kappa^2 Gh} & 0 & 0 & 0 \\ 0 & 0 & 0 & 0 & 0 & \frac{1}{(1-\nu^2)D} & -\frac{\nu}{(1-\nu^2)D} & 0 \\ 0 & 0 & 0 & 0 & 0 & -\frac{\nu}{(1-\nu^2)D} & \frac{1}{(1-\nu^2)D} & 0 \\ 0 & 0 & 0 & 0 & 0 & 0 & 0 & \frac{2}{(1-\nu)D} \end{bmatrix} \quad \mathbf{A}_0 = \begin{bmatrix} 0 & 0 & 0 & 0 & 1 & 0 & 0 & 0 \\ 0 & 0 & 0 & 0 & 0 & 1 & 0 & 0 \\ 0 & 0 & 0 & 0 & 0 & 0 & 0 & 1 \\ 0 & 0 & 0 & 0 & 0 & 0 & 0 & 0 \\ 1 & 0 & 0 & 0 & 0 & 0 & 0 & 0 \\ 0 & 1 & 0 & 0 & 0 & 0 & 0 & 0 \\ 0 & 0 & 0 & 0 & 0 & 0 & 0 & 0 \\ 0 & 0 & 1 & 0 & 0 & 0 & 0 & 0 \end{bmatrix}$$

$$\mathbf{B}_0 = \begin{bmatrix} 0 & 0 & 0 & 1 & 0 & 0 & 0 & 0 \\ 0 & 0 & 0 & 0 & 0 & 0 & 0 & 1 \\ 0 & 0 & 0 & 0 & 0 & 0 & 1 & 0 \\ 1 & 0 & 0 & 0 & 0 & 0 & 0 & 0 \\ 0 & 0 & 0 & 0 & 0 & 0 & 0 & 0 \\ 0 & 0 & 0 & 0 & 0 & 0 & 0 & 0 \\ 0 & 0 & 1 & 0 & 0 & 0 & 0 & 0 \\ 0 & 1 & 0 & 0 & 0 & 0 & 0 & 0 \end{bmatrix} \quad \mathbf{C}_0 = \begin{bmatrix} 0 & 0 & 0 & 0 & 0 & 0 & 0 & 0 \\ 0 & 0 & 0 & 0 & -1 & 0 & 0 & 0 \\ 0 & 0 & 0 & -1 & 0 & 0 & 0 & 0 \\ 0 & 0 & 1 & 0 & 0 & 0 & 0 & 0 \\ 0 & 1 & 0 & 0 & 0 & 0 & 0 & 0 \\ 0 & 0 & 0 & 0 & 0 & 0 & 0 & 0 \\ 0 & 0 & 0 & 0 & 0 & 0 & 0 & 0 \\ 0 & 0 & 0 & 0 & 0 & 0 & 0 & 0 \end{bmatrix}$$

### Finite Difference Algorithm

Based on the finite difference algorithm developed by MacCormack [50], a higher-order algorithm is developed by Yuan [51, 54]. This algorithm is used in this study to simulate the  $A_0$  reflection waves, which is programmed by Matlab. When the initial condition at time step  $n$  is given by  $\mathbf{U}^n = \mathbf{E}_0 \mathbf{u}^n$ , the output value of the next time step  $\mathbf{U}^{n+2}$  can be expressed using the MacCormack splitting method as

$$\mathbf{U}^{n+2} = F_x F_y F_y^+ F_x^+ \mathbf{U}^n \quad (2-44)$$

where  $F_x$  and  $F_y$  are the backward-forward operator in x- and y- direction, and  $F_x^+$  and  $F_y^+$  are the forward-backward operator in x- and y- direction.

Although the explicit finite-difference scheme is computationally much more efficient than the implicit scheme, it is restricted by CFL (Courant–Friedrichs–Lewy) stability condition. CFL stability condition assumes that the waves are not allowed to propagate over two grids in just a single time step, so that the properties of the waves can be preserved in the numerical approximation and the stability is guaranteed. It requires the numerical propagation speed  $\Delta x/\Delta t$  to be less than fastest wave propagation wave. For the MacCormack scheme, the time step is limited by

$$\Delta t < \frac{2\Delta x}{3v_{\max}} \quad (2-45)$$

With  $v_{\max} \approx 3000\text{m/s}$  and  $\Delta x = 1.25\text{ mm}$ , the time step is chosen to be  $0.2\ \mu\text{s}$ . Therefore, the total time of simulation is  $250\ \mu\text{s}$  with 1250 steps, which corresponds to a 5MHz sampling frequency in the experiment. For an aluminum plate which is  $500 \times 500 \times 3.2\text{t mm}$ , the plate is discretized by a  $400 \times 400$  rectangular grid, with grid spacing of  $1.25\text{ mm}$ , and the excitation points is the center of the plate. A five-peaked tone burst signal is emitted from the excitation grid and the wave signal is shown at each grid and at each time step. Figure 2-14A shows a snapshot of the displacement field during simulation at  $t=100\ \mu\text{s}$ .

In the damaged plate simulation, the crack is modeled by altering the property matrix  $\mathbf{E}_0$  at the corresponding grid points. Figure 2-14B shows a snapshot of wave field in the same plate with a  $0.25\text{ mm} \times 0.125\text{ mm}$  rectangular hole (two grids), where we



can observe the scattered wave field. The domain is finite so boundary reflection is present, but is much weaker than the visualized signal at  $t=100\mu\text{s}$ .

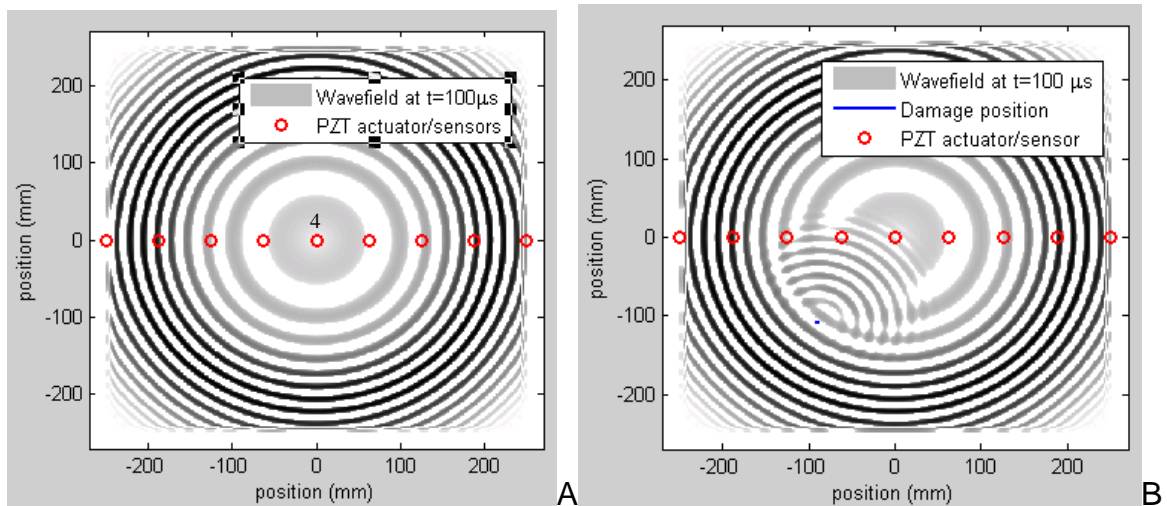


Figure 2-14. A) Snapshot of the simulated structural wave propagating in the pristine plate at  $t=100\mu\text{s}$ . The toneburst wave is emitted from Actuator 4. B) Snapshot of the wave in the damaged plate at  $t=100\mu\text{s}$ . The crack is  $0.25\text{ mm} \times 0.125\text{ mm}$  and located at  $(-90, -110)\text{ mm}$  from the origin.

The comparison between the numerical solution and the analytical solution is presented in Figure 2-15. Since the numerical procedure does not model piezoelectric effect, we only compare their shape and peak time. Also, there is a geometric discrepancy between FDM and analytical solution due to limitation of representation in FDM model. The geometry of damage is circular for the analytical solution, and rectangular for the FDM simulation.

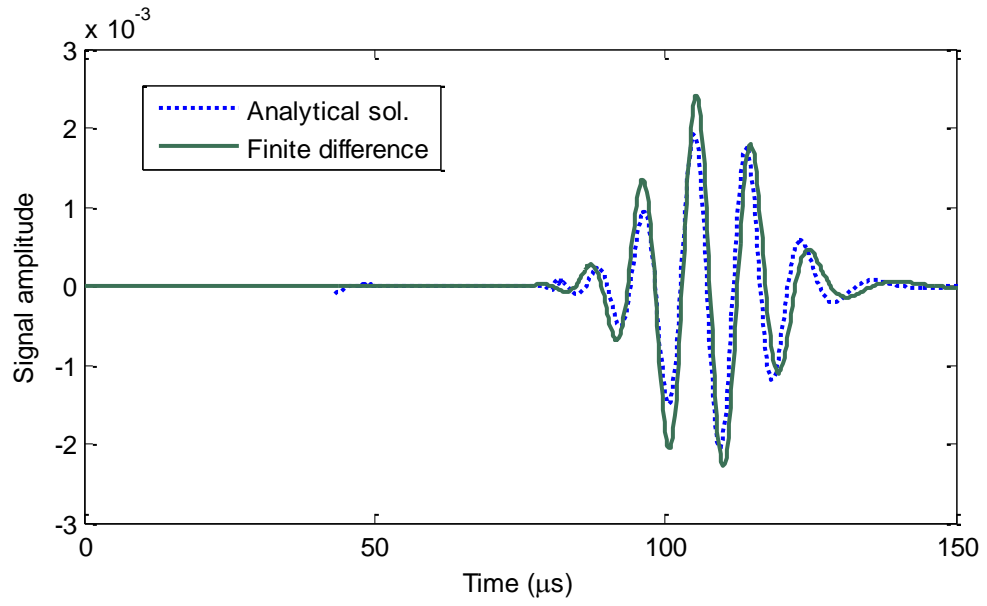


Figure 2-15. Finite difference solution compared with wave propagation analysis

CHAPTER 3  
IDENTIFYING CRACK LOCATION USING MIGRATION TECHNIQUE

The objective of this chapter is finding the location of a crack using the migration technique. The migration technique can identify and visualize the location of damage from the sensor signals. This chapter discusses how we can visualize a crack within the structure using the migration technique, and related topics to improve the performance.

**Migration Technique**

The concept of migration is that when a sensor receives a scattered signal, the time of flight can be found by moving the signal in time domain and finding a time at which the scattered signal matches best with the original excitation signal. In order to find the best matching time, the cross-correlation concept is utilized. Cross-correlation is a process to find the similarity of two correlated signals.

$$\begin{aligned}\Phi_{fg}(t) &= (f \star g)(t) = \int_{-\infty}^{\infty} f^*(\tau) \cdot g(t + \tau) d\tau \\ \Phi_{fg}(t)_{norm} &= \frac{\Phi_{fg}(t)}{\sqrt{\Phi_{ff}(0) \cdot \Phi_{gg}(0)}}\end{aligned}\tag{3-1}$$

where  $f$  is the scattered wavefield at each sensor position,  $f^*$  denotes its complex conjugate and  $g$  is the incident wavefield emitted from the actuator.  $t$  is the time difference, and it defines the  $y$ -location of the intensity value.  $\Phi_{fg}(t)_{norm}$  is the cross-correlation coefficient.

Equation 3.1 indicates that if the two signals are identical, the correlation coefficient  $\Phi_{ff}(0)_{norm}$  is 1, and if the two signals are completely out of phase ( $g = -f$ ), the coefficient  $\Phi_{-ff}(0)_{norm}$  is -1. Here we find the similarity between excitation wave and

scattered wave by adjusting the time difference. Cross-correlation is often used to compare two similar signals, and it is also known as temporal coherence [36]. The time difference that gives maximum value of cross correlation coefficient is defined as the time of flight (TOF).

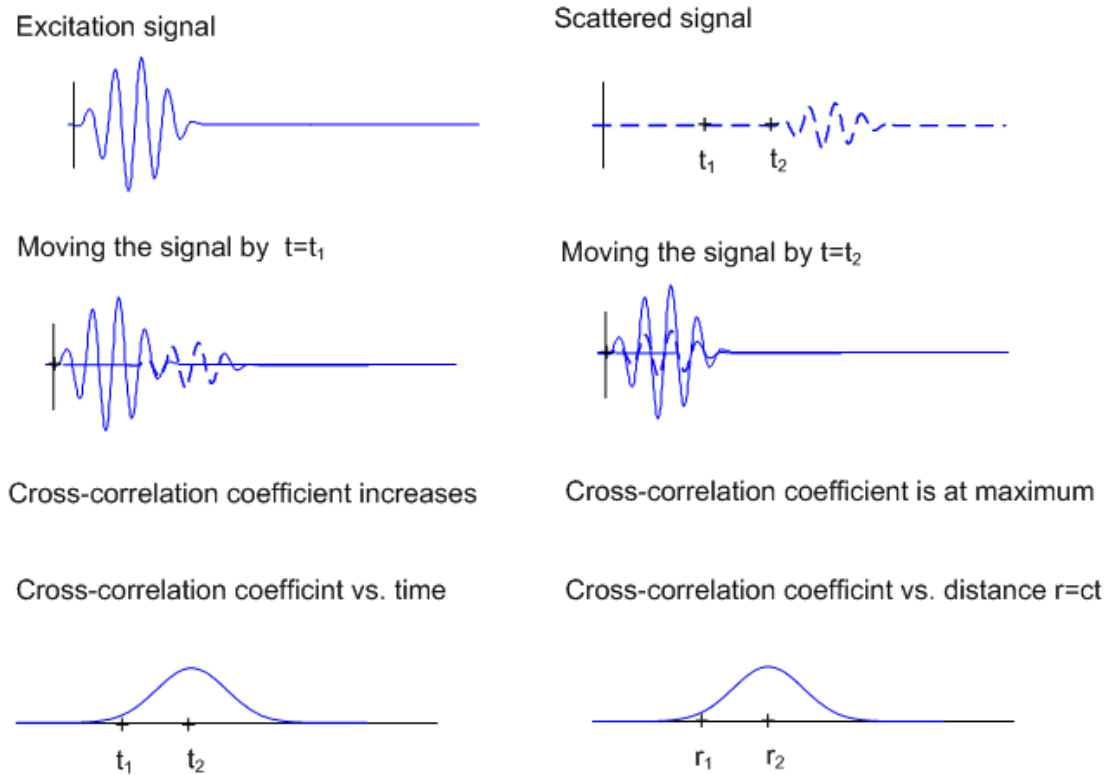


Figure 3-1. Cross-correlation coefficient used to find the time difference between excitation and scattered signal in migration technique.  $c$  is the wave velocity

As shown in Figure 3-1, we find the similarity between excitation and scattered signal. As we increase  $t$  to decrease the time difference between two signals, calculated cross correlation coefficient increases when the last peak of excitation corresponds to the first peak of scattered signal. It reaches the maximum value when all the peaks are at the same position on the adjusted time axis, and decreases after that. Since the wave velocity depends on material properties and frequency, the distance  $r$  is calculated from

the wave velocity and time difference.

One advantage of migration technique over other ultrasonic detection methods is that the TOF is not a deterministic value, but is a range of possible values with possibility specified by cross-correlation coefficient. This leaves a possibility to find the best match between different pairs of actuators or sensors by comparing multiple images.

Another advantage of using migration technique is that the damage image can be readily obtained using the sensor to collect reflected waves from the damage. With the image, the size and shape of the damage as well as its location can be quantified. That is, more accurate and quantifiable damage profile using multiple actuator-sensor pairs can be obtained. Image generation procedure will be discussed in detail later in this section.

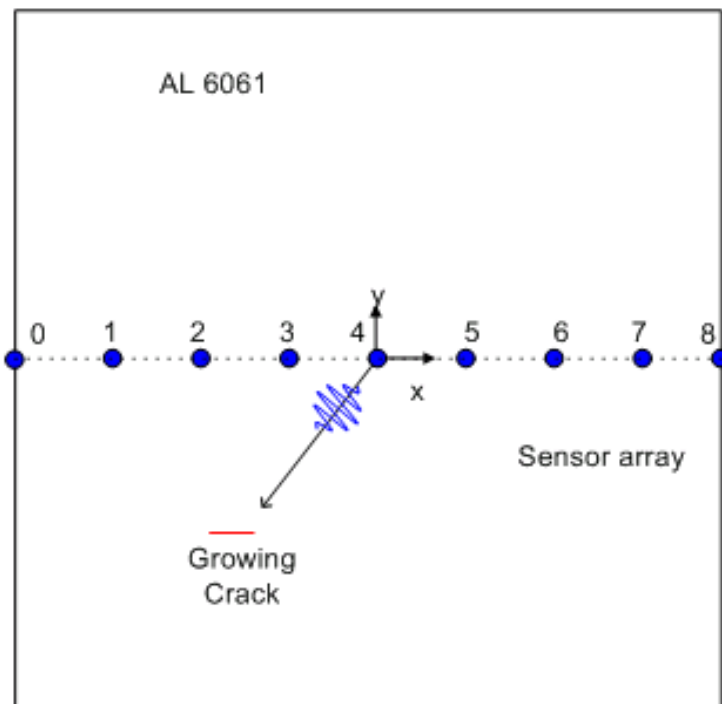


Figure 3-2. Actuator and sensor positions for migration technique

Although analytical solution to the wave propagation problem is available, wave scatter cannot be described with a general formula. Instead, a finite difference algorithm is used for simulation of migration technique. For simulation, an aluminum plate is modeled to identify a through-the-thickness crack in the plate (Fig 3.2). The size of AL 6061 plate is 500 x 500 x 3.2(t) mm, and discretized by 200 x 200 equally spaced grids (grid spacing: 2.5 mm). After the toneburst excitation is introduced, we examine the response of the plate during 250 $\mu$ s with 1250 time steps. To illustrate the procedure, we used signal information from every grid point along the sensor line, so that there are 200 equally spaced signal receivers along the line between 0 and 8. The crack is centered at (-9, -11) cm from the center of the plate. The ultrasonic toneburst wave sent from the actuator is a Hanning window modulated sinusoid transverse loading governed by:

$$q(t) = P \left[ H(t) - H\left(t - \frac{N_p}{f_c}\right) \right] \times \left[ 1 - \cos\left(\frac{2\pi f_c t}{N_p}\right) \right] \sin(2\pi f_c t) \quad (3-2)$$

where  $P$  is the force,  $N_p$  is the number of peaks of the loading, and  $f_c$  is the central (dominant) frequency.  $H$  is the Heaviside function, and  $N_p = 5$ ,  $f_c = 110$ kHz,  $P = 1$ N are used for simulation. Because the PZT excitation is not modeled in the finite difference scheme described in Section 2.4 due to scale difference, we directly apply loading  $q$  instead of voltage to the central point.

The propagating and scattered wave is captured in the form of displacements at each node. The migration technique uses Lamb wave propagation and reflection for imaging damages in the structure. The location of excitation sources are shown in Figure 3-2, and the actual force applied in time scale is shown in Figure 3-3. Sensor locations where we measure the velocity are assumed to be at every grid for maximum

resolution.

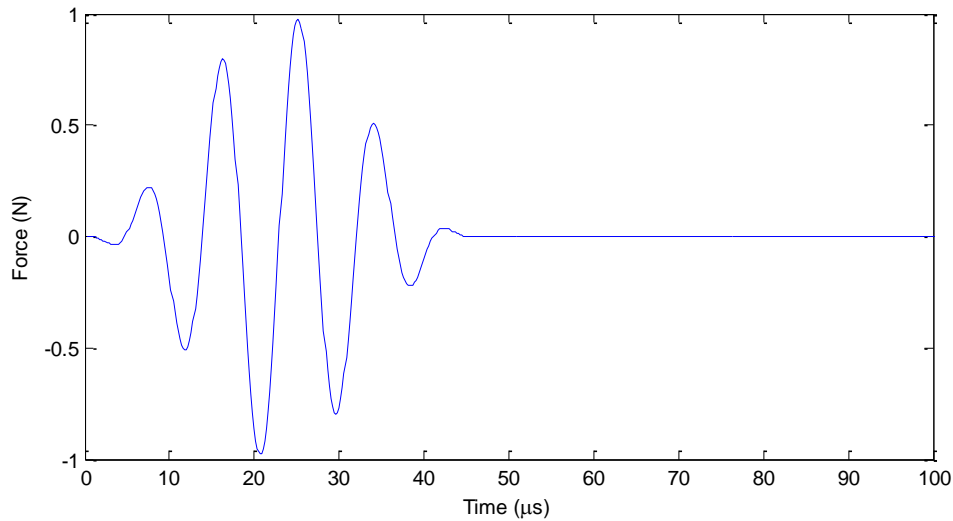


Figure 3-3. Excitation signal

We find the scattered wavefield by subtracting signal obtained from a healthy plate from signal obtained from a damaged plate. By evaluating the scattered wavefield, we can have the scattered wavefield in time and sensor position. Next step in migration technique is back propagation. In time scale, we let the excitation wave to propagate and do the cross-correlation to find the similarity between incident and scattered wavefield. From those wavefields, image intensity is evaluated at every grid point. The wave velocity multiplied by time difference  $t$  between excitation wave and scattered wave indicates the distance from the sensor to the point we are evaluating. The cross-correlation coefficient  $\Phi_{fg}(t)_{norm}$  at the corresponding point is the image intensity in the domain, and the higher image intensity becomes, the more likely to have damage at the given location within the structure. The scattered wavefield  $f$  and incident wavefield  $g$  are shown in Figure 3-4, and the detailed procedure is explained below.

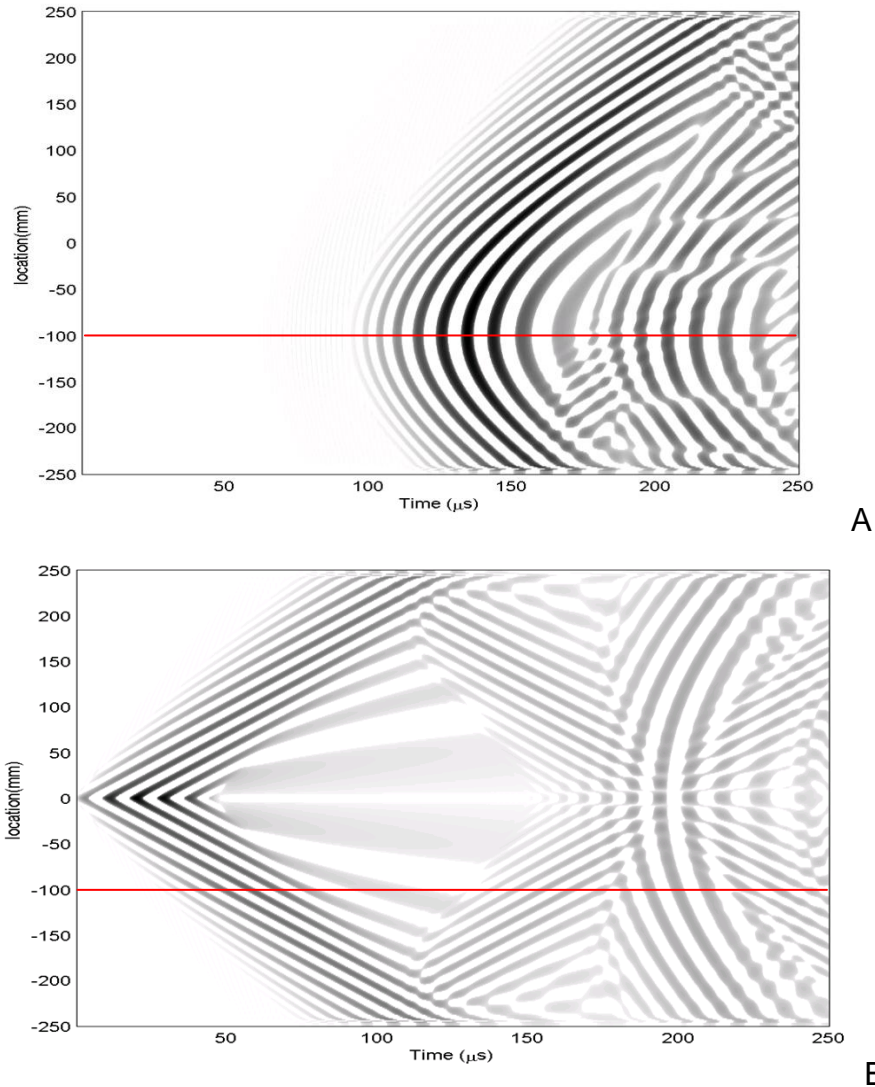


Figure 3-4. A) Scattered wavefield obtained at the sensor position (ordinate), B) Incident wavefield for back propagation. Actuator is located at the origin

The cross-correlation coefficient is calculated for every individual sensor position, which is the ordinate of Figure 3-4, and the time difference used in cross-correlation is linearly related to the distance from the sensor since the velocity of  $A_0$  mode is constant (3km/s). For example, the time difference between scattered signal and incident wavefield at sensor position -100 mm (red line in Figure 3-4) is about 40  $\mu\text{s}$ . Then the cross-correlation coefficient is measured by Eq.3-1, and the image intensity value at the position (-100, -120) mm from the center is assigned with the coefficient. So the



distance between sensor position and evaluating point is determined by multiplying the time difference with the velocity of the incident wave, and the image intensity is the cross-correlation coefficient. This procedure is done for every sensor position, and every time difference.

Calculating the cross correlation coefficient requires a large amount of computation for integration. To reduce the computation time, frequency domain migration technique (f-k migration) was developed in geophysics [67-68] and extended for SHM by Yuan et al [55]. F-k migration is computationally more efficient than the reverse-time migration. The calculation speed is almost in real time. In f-k migration, the signal is transformed to the frequency domain using discrete Fourier transform, and the cross-correlation is calculated by Eq. 3.3

$$\Phi_{fg}(t) = (f \star g)(t) = \mathcal{F}(f)^* \cdot \mathcal{F}(g)$$

$$\Phi_{fg}(t)_{norm} = \frac{\Phi_{fg}(t)}{\sqrt{\Phi_{ff}(0) \cdot \Phi_{gg}(0)}} \quad (3-3)$$

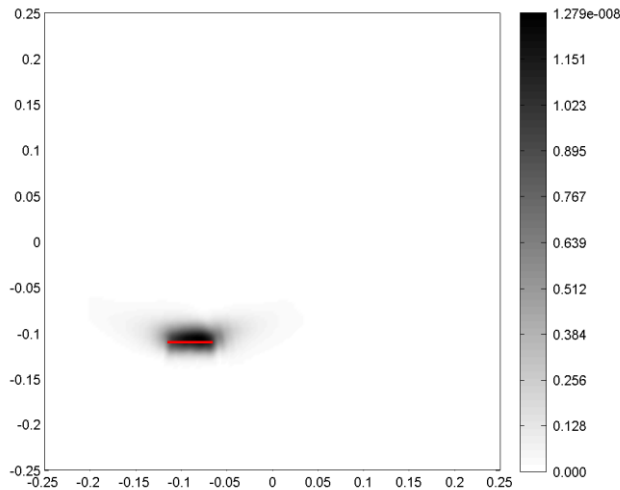


Figure 3-5. Final images obtained by evaluating the image intensity at each point from simulation for a 50mm straight horizontal crack.

Figure 3-5 shows the case when the wave is simulated by FDM. Since we have one image data from each excitation event, we have 7 images in total and prestack approach developed by Yuan is used to obtain the final image [51].

So far, we have discussed how we can obtain images from signal using the migration technique. As we have seen in the results, the images indicate damage existence and its approximate location.

### **Bayesian Approach**

Migration technique provides the inspector an image, which is easily interpreted visually. However, the image only provides approximate location. Therefore, if we are interested in more detailed information such as coordinates of cracks, we need to improve its accuracy. From the images obtained from the migration technique, image intensity refers to the grayscale value at each point in the images. This section describes how to combine the image intensity of several images about one crack using Bayesian approach.

### **Bayesian Approach**

For more accurate estimation of crack location through migration technique, we have applied Bayesian approach to the migration technique to enhance the result. The main objective of this section is to improve the accuracy of detecting crack location by using Bayesian update.

Bayes' rule about conditional probability was suggested in the 1700's, but the development for practical applications has started in the 1900's mainly because of the

computational burden. This rule is about conditional probability, and the rule consists of simple formula stated in Eq.3-4.

$$P(A | B) = \frac{P(A)l(B | A)}{P(B)} \quad (3-4)$$

This formula indicates that if we are interested in probability of A, given B, we can calculate the probability by an inverse formula.  $P(A)$  is the prior probability of A,  $l(B|A)$  is the probability of B, given A, which is called the likelihood, and  $P(B)$  is marginal probability of B which acts as a normalizing constant. So this is especially useful when we know the probability of B given A. Bayesian approach has been shown many times to give better estimation by combining prior knowledge and likelihood to draw conclusions [69].

The Bayesian framework can be applied to identify the location of the crack by incorporating the image intensity data with prior information. When we have the image intensity information, the coordinates of crack center can be stated by:

$$f^{upd}(x, y | I^i(x, y)) = \frac{f(x, y)l(I^i(x, y) | x, y)}{\int f(x, y)l(I^i(x, y) | x, y) dx dy} \quad (3-5)$$

where  $x, y$  are the coordinates of a possible location of the center of the crack,  $I^i(x, y)$  is the image intensity obtained from  $i^{\text{th}}$  test,  $f$  is the prior distribution which is the current state probability density that crack center exist at  $x, y$  without  $i^{\text{th}}$  image intensity information, and  $l$  is the likelihood function from current data, which is the probability that we will get the image if the crack center is located at  $x, y$ .

In Bayesian approach, the likelihood function represents the relation between actual crack center location and what we obtained. For this example, if the center of

crack is  $x, y$  then the probability density that we can obtain the image intensity from the migration simulation is defined as the likelihood. In Eq.3-5, we assume that the image intensity distribution along the  $x$  and  $y$  coordinates are independent, or the randomness of the two is not correlated.

In this study, a horizontal crack centered at  $(-90, -110)$  mm with length of 40 mm is considered. A five-peaked toneburst narrowband excitation with center frequency 110 kHz (duration of 44  $\mu$ s) is emitted from an actuator. After the flexural waves propagate in the plate, the reflected signals from the damage are detected by the sensors. Seven actuators are excited sequentially and 200 sensors located along the  $x$ -axis collect reflected waves for maximum resolution. Under this excitation frequency, only the first fundamental flexural mode propagates in the plate. In an isotropic aluminum material, the group velocity for the center frequency is around 3 km/s with wavelength of 27 mm. We use finite difference method for calculating the wave propagation. An Al-6061 aluminum square plate with dimension  $500\text{mm} \times 500\text{mm} \times 3.2\text{mm}$  is discretized by  $200 \times 200$  plate elements. Simulated sensor data is collected from 1250 time steps (total time span: 250  $\mu$ s). Using the simulated sensor data, the migration technique is then used for imaging the crack.

We start the process to determine the center of the crack location by assuming a non-informative prior or initial distribution of  $x$  and  $y$  on the plate. Here we choose a uniform distribution function as our prior distribution for plates that have never been inspected before. Assuming that the origin is at the center of the plate, we can construct a prior distribution as Eq.3-6, which implies that we have no information for the plate before inspection and the damage might exist anywhere.

$$f(x, y) = f_{\text{uniform}}(x; -250, 250) \times f_{\text{uniform}}(y; -250, 250) = 4 \times 10^{-6} \quad (3-6)$$

where  $f_{\text{uniform}}$  is the probability density function of a uniform distribution. With the given prior distribution, the next task is the selection of appropriate likelihood estimators  $l(I^i | x, y)$  for our next iteration. In this case, the test result  $I^i$  indicated by the image intensity is a deterministic known value obtained in the simulation. If the center of crack is  $x, y$  then the probability density that we can obtain the image intensity from the migration simulation is the likelihood.

However, due to computational cost of the migration techniques, accurate estimation of likelihood estimator is almost impossible. Instead, we suggest several ways to assume and estimate  $l$  through error analysis. In the following two subsections, we suggest two basic ways to construct the likelihood estimators, direct image intensity and multivariate normal distribution.

### **Direct Image Intensity**

The simplest way to construct a likelihood function out of given image is direct interpretation of the given image intensity to our likelihood function. In other words, the probability that we will get the image when the center of the crack is at point  $(x, y)$  is proportional to the image intensity at  $(x, y)$ . In this case the likelihood estimator is defined by Eq.3-7.

$$l(I^i | x, y) = I^i(x, y) \quad (3-7)$$

Using this likelihood function with Bayesian updating with all seven images from the seven actuators, we obtained the final distribution shown as an image in Figure 3-6.

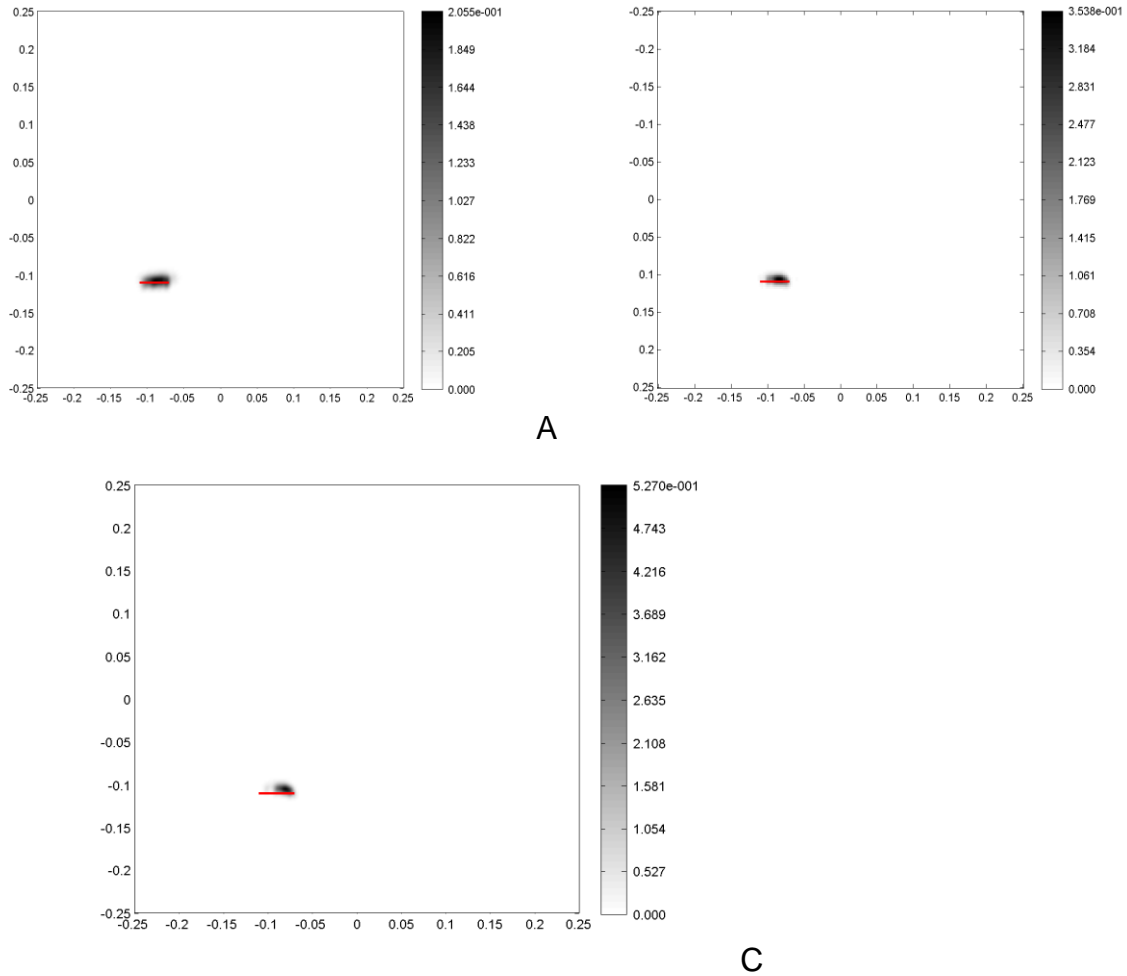


Figure 3-6. Combining image using direct image intensity as likelihood A) Up to 3<sup>rd</sup> actuator B) Up to 5<sup>th</sup> actuator C) Up to 7<sup>th</sup> actuator (final)

### Multivariate Normal Model about Center of Intensity

Instead of using the entire image data, we may elect to use only the center of intensity to estimate where the center of the crack is. The center of intensity of an image obtained from  $i^{\text{th}}$  actuator is defined by Eq.3-8.

$$x_{c,i} = \frac{\iint xI^i(x, y)dxdy}{\iint I^i(x, y)dxdy}, y_{c,i} = \frac{\iint yI^i(x, y)dxdy}{\iint I^i(x, y)dxdy} \quad (3-8)$$

This estimation has errors associated with the migration technique. By simulating a large number of cracks, we found that the error in estimated location from each actuator follows a simple trend defined by a bi-variate normal distribution, and the variation due to location of crack center is observed (Figure 3-7).

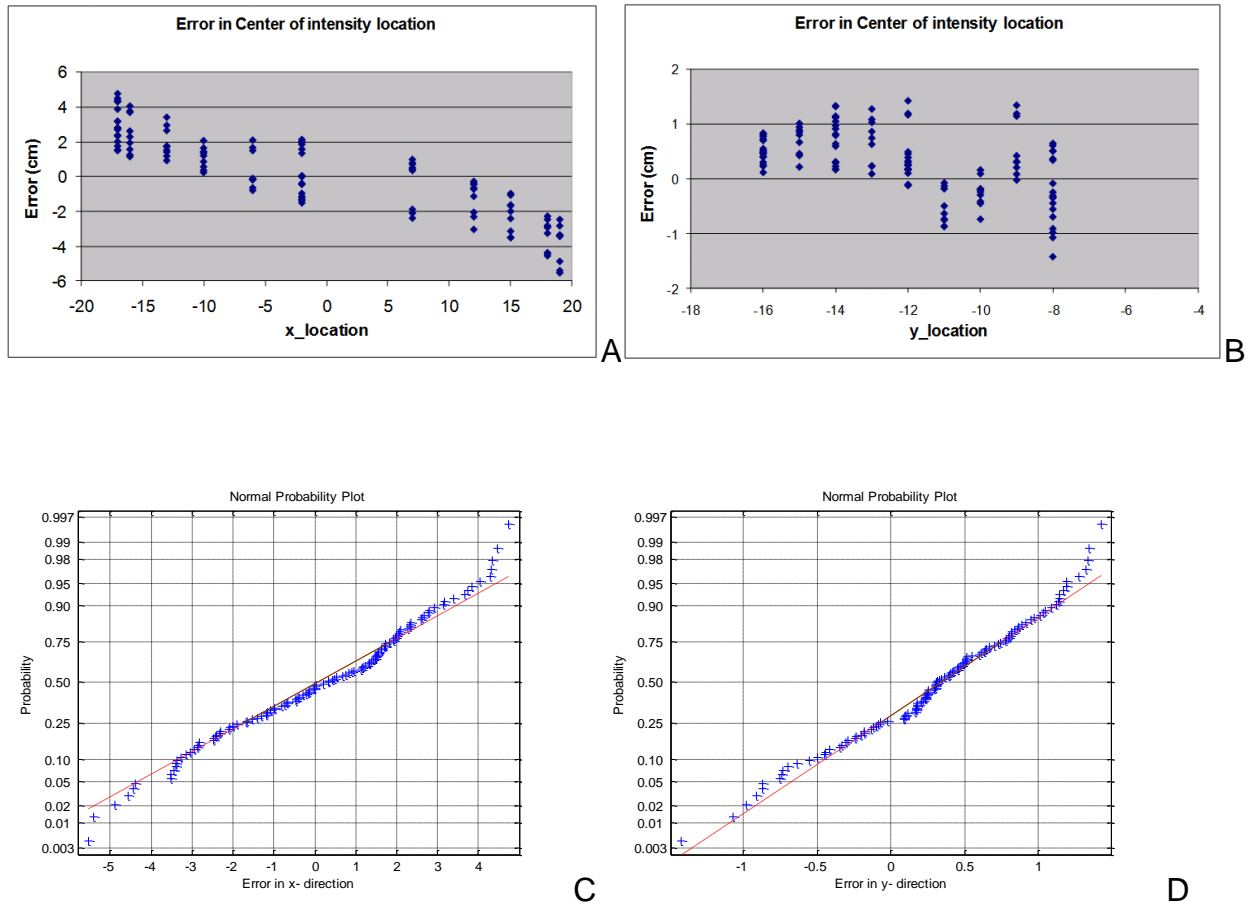


Figure 3-7. Estimation error in x and y directions. We tested 117 different crack configurations with different actuators and calculated the difference between actual locations and the estimated locations. A and B shows estimation error associated with location of crack center, and C and D shows normal fit of the error distribution.

So, we defined a multivariate normal model for the likelihood in Eq.3-9.

$$\begin{aligned}
 l(I^i | x, y) &= l(x_{c,i} \text{ from } I^i | x) l(y_{c,i} \text{ from } I^i | y) \\
 &= f_{normal}(x_{c,i}; x - c_1 x, \sigma_x^2) \times f_{normal}(y_{c,i}; y + \hat{y}, \sigma_y^2)
 \end{aligned}
 \tag{3-9}$$

where the parameters are estimated as  $\sigma_x = 24.2mm$ ,  $\sigma_y = 6.0mm$ , and linear coefficient in x direction as  $c_1 = -1.62$  from Figure 3-7A and the bias in y direction as  $\hat{y} = 3.07mm$  from Figure 3-7D.

The bi-variate distribution gives the probability of the center of intensity being at a point, given that the center of the crack is at  $(x, y)$ . Using Bayesian updating with this likelihood function with all seven images from seven actuators, we obtained the final distribution shown as an image in Figure 3-8. The estimated locations by center of intensity and their error in the crack center location are shown in Table 3-1.

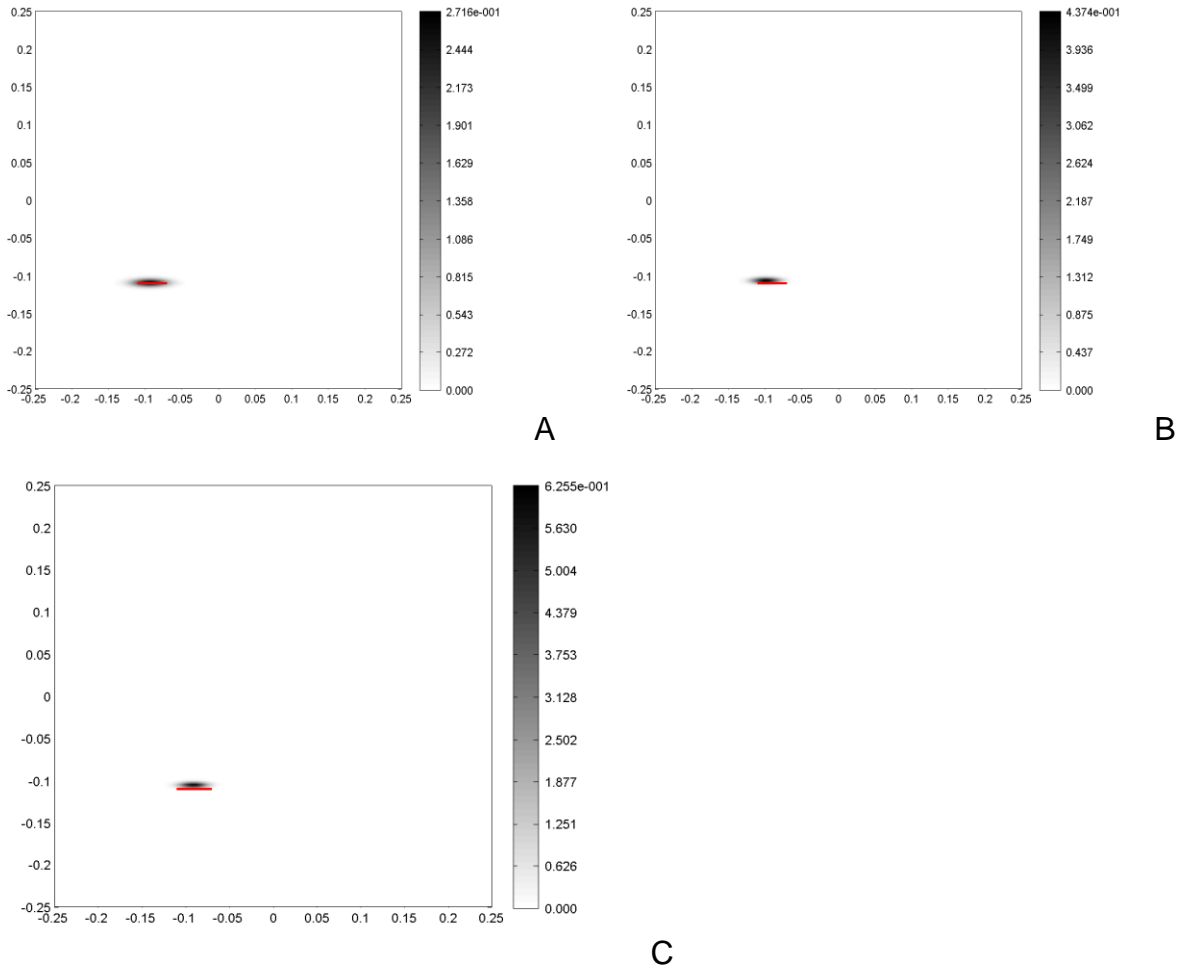


Figure 3-8. Combined image using multivariate normal model. A) Up to 3<sup>rd</sup> actuator B) Up to 5<sup>th</sup> actuator C) Up to 7<sup>th</sup> actuator (final)



Table 3-1. Estimation error due to different imaging techniques

Likelihood estimators	Estimated location (mm)	Distance from true crack center (mm)
Actual	-90.0, -110.0	-
Prestack migration	-81.1, -104.0	10.73
Direct image intensity	-82.7, -105.7	8.47
Multivariate normal	-91.4, -105.5	4.71

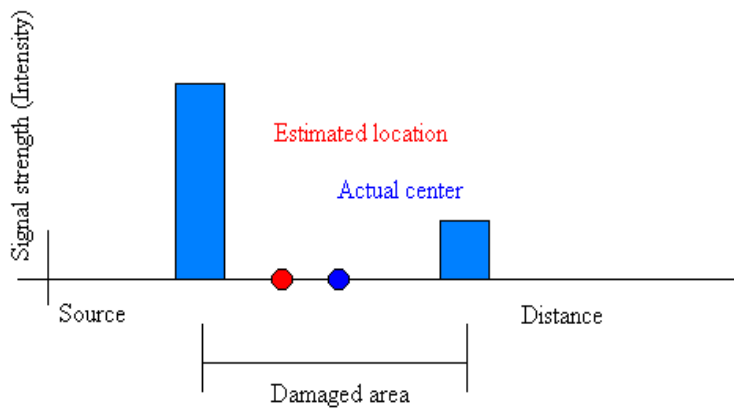
Table 3-1 shows that the estimated crack center is closer to the true crack center. Although the improvement is small, we have much more focused images such as Figure 3-6 and Figure 3-8 compared to prestack images shown in Figure 3-5. So the chance of misinterpretation of crack location is low.

### **Compensation for Geometrical Decay**

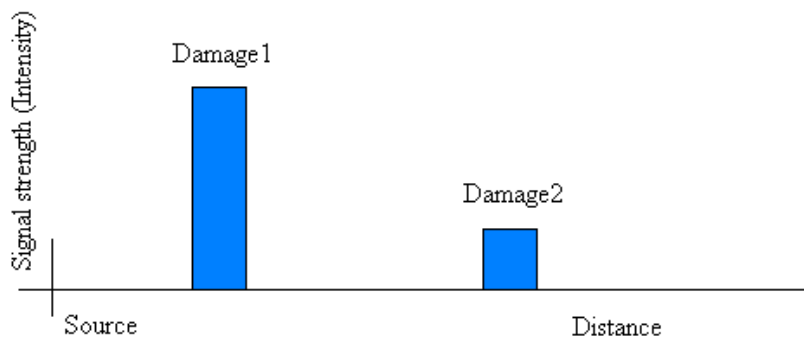
In the previous section, we have introduced a Bayesian approach to improve the accuracy of crack center location by images obtained from the migration technique. However, it is found that there exists a bias of the detected damage location due to different sensor-actuator combinations. We have concluded that the bias came from geometrical decay. As a result, the image intensity when the damage is located close to the actuator and sensors is higher with the image when it is located far from the actuators and sensors. This happens because the image intensity depends on the distance from the sensor and actuator. To compensate the effect of distance on image intensity and to obtain a more accurate location of the damage, a correction method for signal decay is suggested.

For 2D or 3D structures, the strength of propagating Lamb wave experiences geographical decay caused by dispersion of wave to larger wavefront at a longer distance region. In addition, the white noise in the signal is greatly amplified near the

actuator. As a result, the image intensity in the sensor shows a combined effect of reflection and distance from damage. The signal amplitude differs a lot when we have a crack at a different location. To summarize, the signal amplitude for small damages that are close to the sensor and actuator is larger than that of large or severe damages that are far from the sensor and actuator (Figure 3-9).



A



B

Figure 3-9. Possible errors related to geometrical decay A) The estimated center of damage may have an error B) Damages that have the same size are depicted differently because of their locations.

The idea of compensating for decay of signal such as attenuation was first proposed in the medical imaging area [66]. When ultrasonic waves are used for medical imaging, the effect of decay causes many problems, and more accurate images are

obtained by compensating for attenuation of signals. In this section, the compensation procedure is introduced to SHM in order to solve the inaccuracy problem and to decompose the size from location simultaneously.

### **Geometrical Decay in Plate Wave**

As described in Chapter 2, when an ultrasonic pulse disperses from a point source, the amplitude experiences a decay described by Bessel function in space, and experiences exponential decay in time. From the asymptotic function of Bessel function, the maximum amplitude  $A$  at distance  $r$  can be described as:

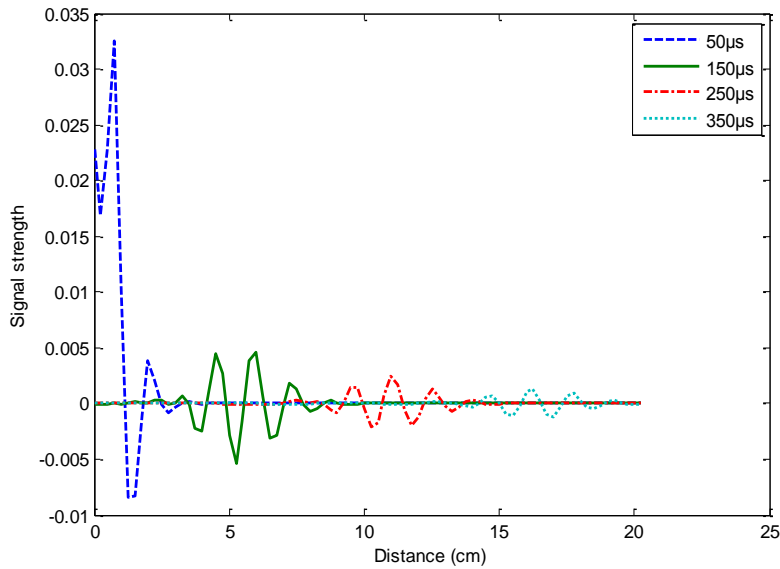
$$A \propto \sqrt{\frac{1}{kr}} \propto \frac{1}{t} \quad (3-10)$$

where  $k$  is the wave number.

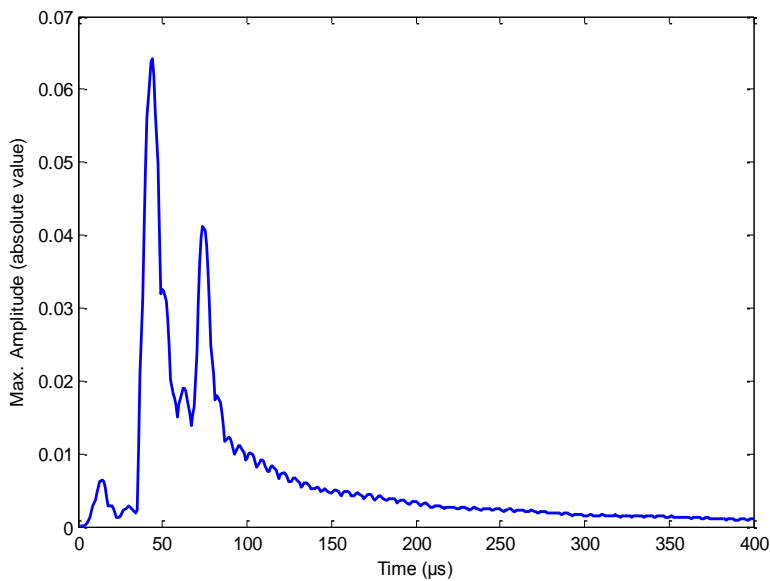
In the actual simulation and experiment, a five-peaked tone-burst signal is used for successful generation of Lamb waves within the plate. However, the initial amplitude does not follow the above relation closely because of the transient response and inertia effect. By using finite difference simulation, the geometrical decay of signal with respect to time and distance is calculated, as shown in Figure 3-10A. We used 200 x 200 grids in an Al 6061 square plate of 500 x 500 x 3.2 mm to simulate the results.

Also, we have obtained the profile of decay of the maximum amplitude as a function of time (Figure 3-10B). The graph fits Eq. 3.10 well after all the transient effects are gone. Figure 3-10B shows the maximum amplitude specified from simulation at each time step. As time goes by, and the wave travels further, the signal strength decreases due to dispersion. Thus, the signal strength highly depends on the location of the damage as well as its severity. In the imaging technique, this causes weak signal in

the far region, which correlates distance with image intensity. Although human eyes conceive every point in an image equally weighted, but the truth is that the points near the actuator and sensor are greatly amplified due to stronger signal strength.



A



B

Figure 3-10. A) Signal decay with respect to wave propagation in plate, generated from the finite difference model B) Decay profile in a plate with respect to time

From the observations made in the simulation, a compensation curve is constructed using a Matlab curve fitting tool (cftool). We assumed that the amplitude  $A$  is inversely proportional to time  $t$  following this relation:

$$A \propto \begin{cases} 1/(t-t_d) & (t > t_d) \\ 1 & (t < t_d, \text{unknown}) \end{cases} \quad (3-11)$$

where  $t_d$  is a threshold time for the transient region. We assume that the amplitude is uniform during the transient period. From data analysis, we choose  $t_d = 58 \mu\text{s}$ .

There are two ways to compensate for attenuation of signal strength. One is to apply the compensation scheme in the time domain, while the other is to apply it in the spatial coordinates. In this section, we construct the curve in Eq.3-11 based on time domain and applied to the received signal directly (Figure 3-11). After that, the back propagation stage of migration technique is compensated based on distance. Compensating for back propagation stage is discussed in the next section.

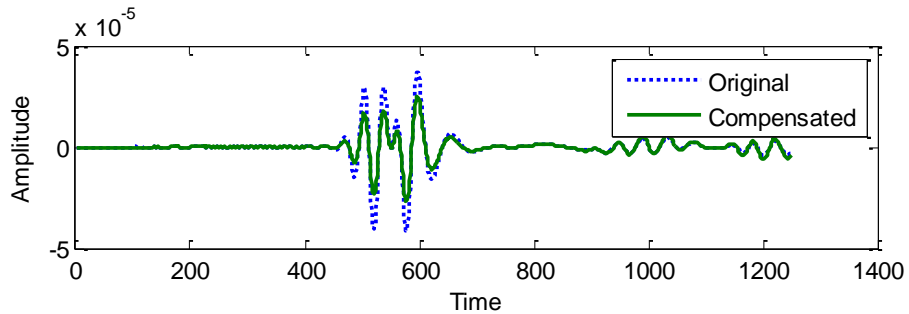


Figure 3-11. An example of compensated signal displayed on time scale.

### Application to Migration Technique

The migration technique comprises two different steps: detection of the reflected wave and back-propagation. Then the image intensity is calculated by cross-correlation of the reflected wave and the back-propagated wave. The reflected wave first travels

from the actuator to damaged site and as the wave hits the damage, the reflective wave propagates as if the source is at the point of damage. During these propagation paths, the wave strength decays.

Then the back-propagated wave also decays when traveling the distance between actuator and a point. By calculating the cross-correlation, or convolution, of these two waves, the image intensity  $I$  has a relation stated in Eq. 3.12, and the compensated image intensity can be calculated by Eq.3-13.

$$I \propto A_{\text{actuated}}^2 \cdot A_{\text{reflected}} \propto 1/d_{\text{actuator-distance}}^2 \cdot d_{\text{sensor-distance}} \quad (3-12)$$

$$I_{d\text{-corr}} = I d_{\text{actuator-distance}}^2 \cdot d_{\text{sensor-distance}} \quad (3-13)$$

where  $I$  is the image intensity used to represent the possible damage location in the domain,  $A$  is the amplitude of a signal, and  $d$  is the distance between the actuator/sensor and the point in the domain.

We applied the signal compensation, and in addition to that, corrected image intensity is calculated by  $I d_{\text{actuator-distance}}^2 \cdot d_{\text{sensor-distance}}$  at a point  $(x, y)$ . With this procedure, the effect of distance from the imaging result is eliminated.

## Numerical Simulation

The simulation is done by finite difference scheme using 200 x 200 grids on a 50 x 50 x 0.32 cm square plate with 1250 time steps (1 $\mu$ s time interval). A straight, horizontal crack is centered at (-9, -11) cm from the center of the plate, and the size is 4 cm. Those three techniques use the same sensor information.

Figure 3-12 shows the images obtained from the three methods, using the migration technique, using Bayesian approach (Section 3.2), and applying

compensation for geometrical decay in addition to Bayesian approach. The three images do not show a significant difference about the location at a glance, but the error of estimation of crack center location is greatly reduced by attenuation compensation. The crack center location is obtained from taking the mean of entire image. Table 3-2 summarizes the results.

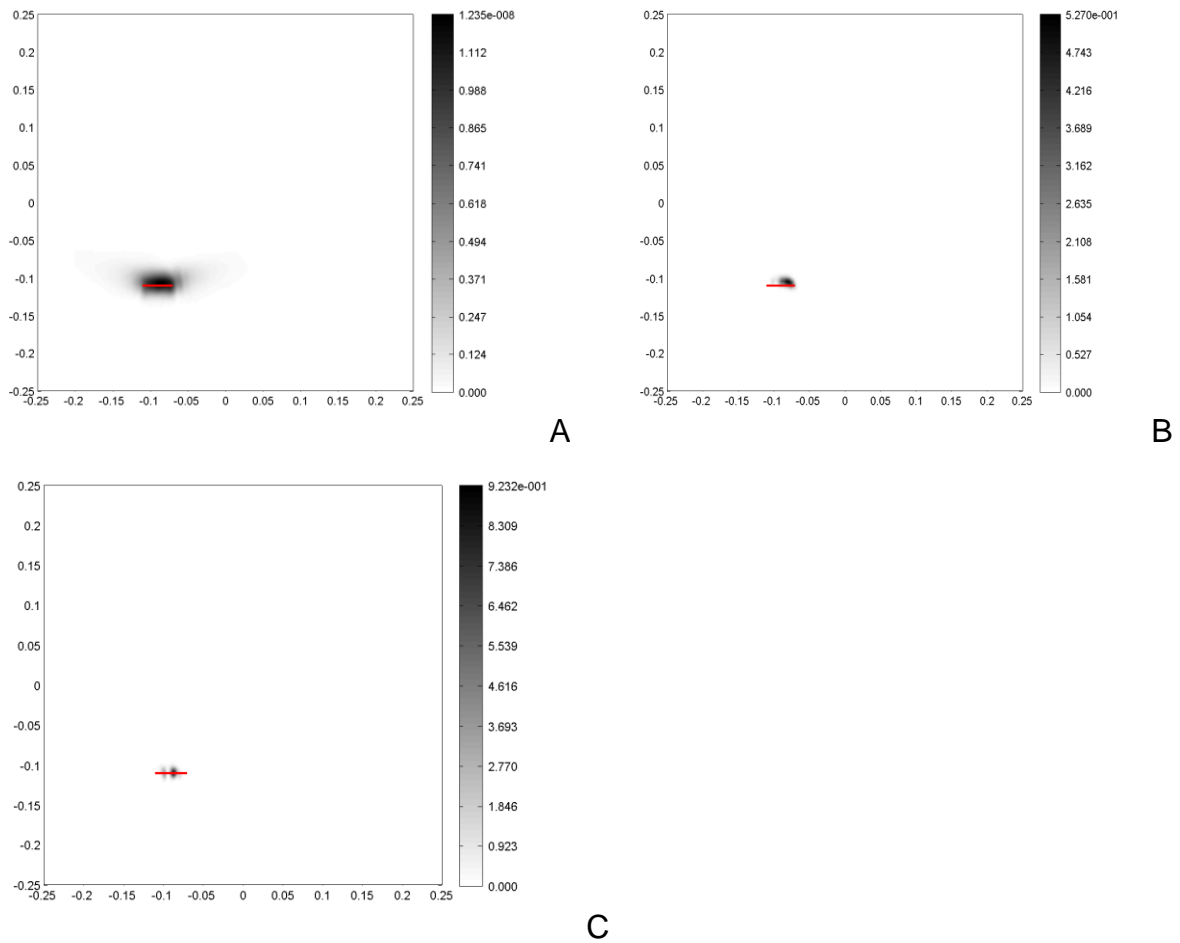


Figure 3-12. Images from migration technique with the same sensor data. A) Prestack approach B) Bayesian approach C) Bayesian approach with compensation for geometrical decay

Also, in order to check if the formula for compensation is valid, we also simulated several crack locations to check if they yield a consistent level of image intensity with respect to size. The result is shown in Figure 3-13 and Table 3-3.

Table 3-2. Comparison of accuracy, different imaging results.

Imaging method	Estimated location (mm)	Distance from true crack center (mm)
Actual	-90.0, -110.0	-
Prestack migration	-81.1, -104.0	10.73
Bayesian approach	-82.7, -105.7	8.47
Bayesian approach with compensation factor	-88.6, -108.3	2.20

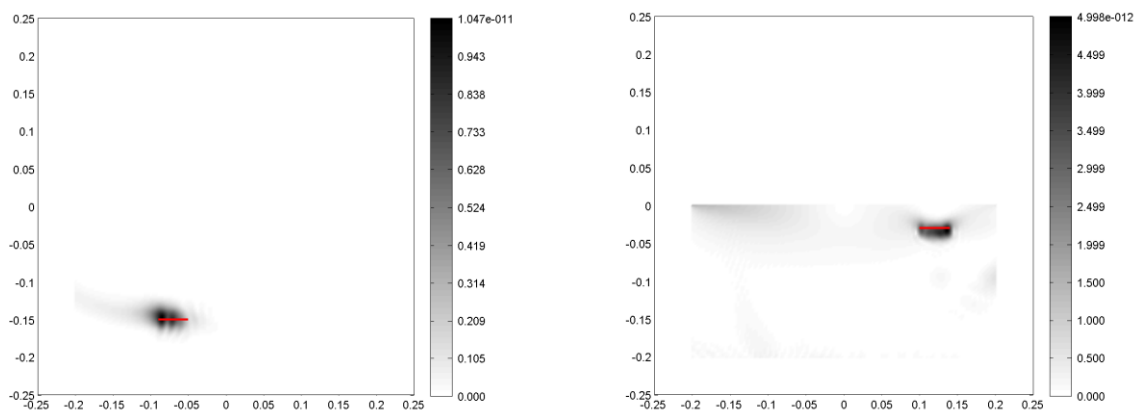


Figure 3-13. Image intensity distribution for a single actuator image

Table 3-3. Comparison of imaging results

Crack location	Estimated location (cm)	Difference (cm)	Max. Intensity
(-7, -15) cm	(-6.63, -14.65) cm	0.509 cm	$1.047 \times 10^{-11}$
(-12, -3) cm	(-13.02, -3.17) cm	1.034 cm	$4.998 \times 10^{-12}$

In principle, all images of a crack regardless of the actuator location should provide the same value of image intensity after compensation. However, we observed that the image intensity of a closer actuator is still greater than the others. This is because that the crack orientation, reflection angle and other minor characteristics are not fully considered in the compensation procedure. We did not include them in the procedure since they only have a minor effect, and they tend to be easily contaminated by the error in real situation.



We have applied the idea to Migration technique to improve it with compensation. The numerical results showed an improvement of accuracy of the estimated crack center location. In SHM, many diagnostic techniques using ultrasonic wave propagation and reflection have been suggested. There are techniques that reduce location error by time of arrival, but it is not sufficient enough for decomposing the effect of signal strength and distance. The location from the image obtained from diagnosis mainly depends on the time of arrival, but the effect of signal strength still remains in the image. In a previous study on the migration technique, our research group has discovered the biased error due to this feature [57]. In order to compensate for the bias error of detecting crack location, we suggested a compensation for decay of signal strength for ultrasonic imaging techniques. The motivation for this application is improving numerical accuracy of detection techniques suitable for transfer to prognostic stage. Since the prognosis process involves a large amount of uncertainty compared to diagnosis, a small error may be critical for evaluating remaining lifecycle of the structure.

## CHAPTER 4 EXPERIMENTAL STUDY ON IDENTIFYING CRACKS OF INCREASING SIZE

An experiment is conducted to explore the relationship between the sensor signal amplitude and crack size through experiments and simulation for estimating the size. The objective of this chapter is to explore the relationship between the sensor signal amplitude and crack size through experiments and simulation for estimating the size. Cracks are machined into an aluminum plate with increasing size, and measurements are carried out with ultrasound excitation using piezoelectric transducer arrays that alternate their role as actuators or sensors.

### **Test Panel and Test Procedure**

An Aluminum 6061 panel (600mm×600mm×3.2mm) was tested for examining the ability to estimate the size of a through-the-thickness crack. Table 4-1 shows the mechanical properties of the panel. In order to detect a crack, we used two sets of linear sensor/actuator arrays, with each set containing nine lead zirconate titanate (PZT) discs (diameter 10 mm; thickness 0.4 mm, refer to Table 4-2). Each PZT disc can be a sensor or an actuator. The equally-spaced sensor arrays are attached to the plate by epoxy bond (Loctite 401) as shown in Figure 4-1C with 62.5 mm spacing, and the total length of sensor array is 500 mm. The two sets of linear arrays are used to study the effect of crack location. Figure 4-1C also shows a vertical array of sensors, which is not used for this paper. When a PZT disc is used as an actuator, all other PZT discs in the array are used as sensors. The sensors at both ends (numbered 0 and 8) are not used as actuators but only as sensors. Thus only seven PZTs are used as actuators to emit the ultrasonic signal into the plate, and the Lamb wave generated from the actuator is

recorded at the remaining sensors for both the pristine and damaged states for every crack increment. The excitation from the PZT is a five-peaked toneburst signal. Scattered wavefield from the damage is calculated by the difference between the pristine and damaged states. The crack was manufactured first by drilling a 4.5mm diameter hole centered at (-90mm, -110mm) at the center of the plate. Afterwards, we gradually increased the size of the damage to form a shape close to a straight crack up to 50 mm in length by machining (Figure 4-2). The fifteen crack sizes tested are listed in Table 4-3.

Table 4-1. Mechanical properties of aluminum plate

Young's modulus E (GPa)	72
Poisson's ratio $\nu$	0.3
Density $\rho$ (kg/m <sup>3</sup> )	$2.73 \times 10^3$

Table 4-2. Properties of piezoelectric disc (modified PZT-4)

Geometry (mm)	diameter:10.0, thickness:0.4
Density $\rho$ (kg/m <sup>3</sup> )	$7.9 \times 10^3$
Young's modulus E (GPa)	$E_{11}: 86, E_{33}: 73$
piezoelectric coefficient $d_{31}$ (m/V)	$-140 \times 10^{-12}$
Piezoelectric coefficient $d_{33}$ (m/V)	$320 \times 10^{-12}$
Piezoelectric coefficient $g_{31}$ (Vm/N)	$-11 \times 10^{-3}$
Piezoelectric coefficient $g_{33}$ (Vm/N)	$25 \times 10^{-3}$
Dielectric constant $K_3$	1400

Table 4-3. List of crack sizes tested, (unit: mm)

2.5 (hole)	13.8	31.5
3 (hole)	16	35
4.5 (hole)	18	40
9	21	45
11	26	50

NI PXI-1000B system was used for data collection with the LabView program. The sampling rate was set to 5MHz, and the signal resolution was 16-bit. Since the resulting signal amplitude from the sensors was very small, a Piezo Linear Amplifier EPA 104

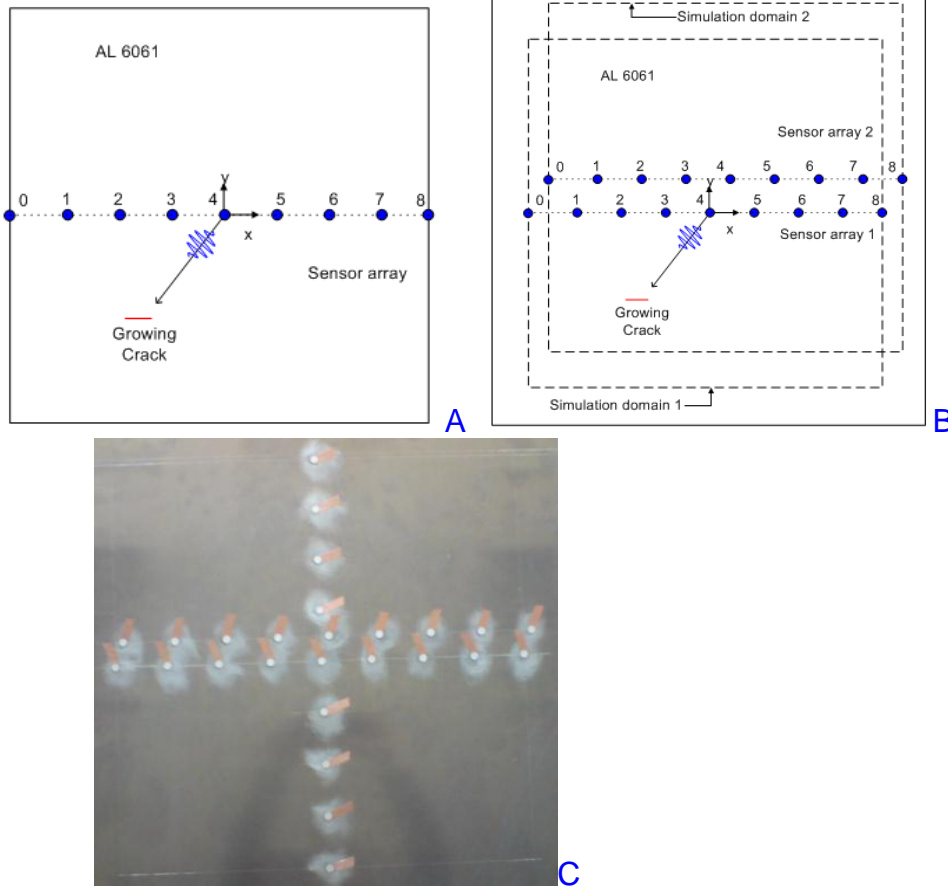


Figure 4-1. Layout of actuators and sensors A) One set of sensors for simulation and experiment B) Two sensor arrays attached to the plate and their corresponding domain C) Aluminum 6061 test plate – pristine state. Three arrays of sensors are attached to the plate, but the vertical array is not employed in this research.

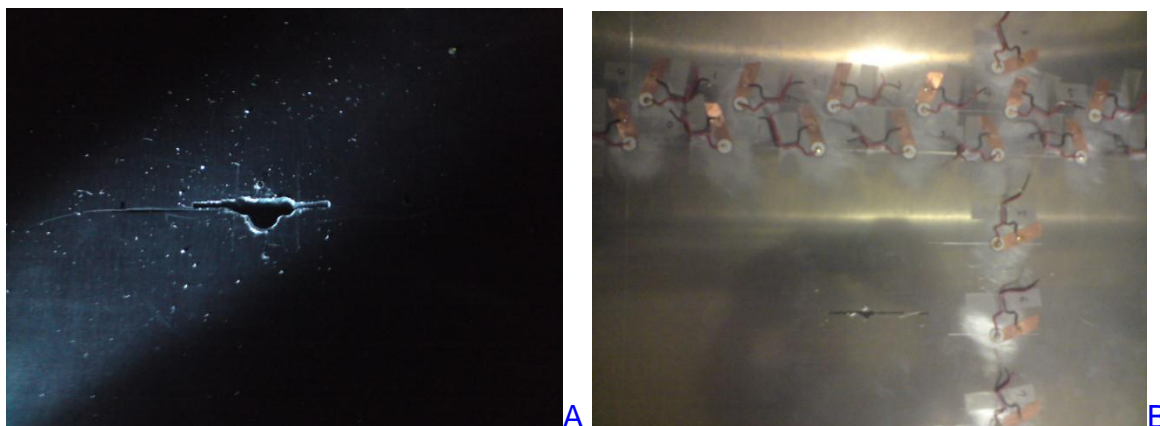


Figure 4-2. Damage manufactured to the plate A) 16 mm damage centered at -90, -110 mm B) 50 mm machined crack

with 7 dB gain was used (Figure 4-3). A band-pass filter between 50 kHz and 250 kHz is used to enhance the signal response.

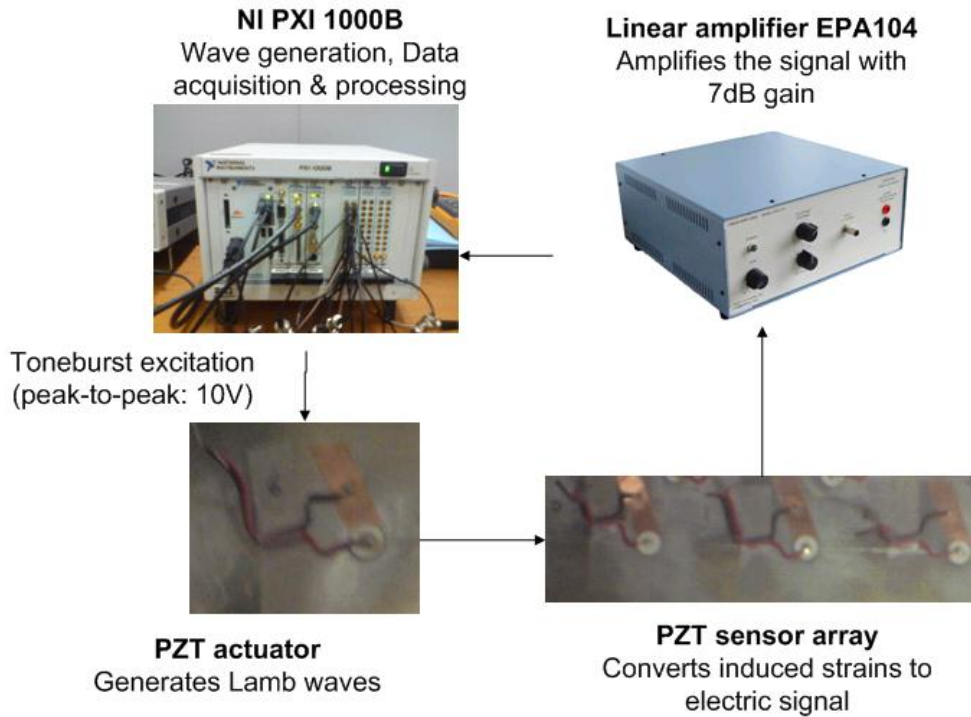


Figure 4-3. Signal generation and acquisition in the experimental set-up

In addition to that, to reduce the effect of Gaussian random noise in the obtained signal, the excitation from the PZT is repeated ten times and the sensor readings are averaged. This repetition can reduce the effect of random noise by a factor of approximate three. By comparing two signals under identical test condition without repetition, we observed white noise that follows a Gaussian distribution with zero mean and standard deviation of 3 mV after the amplifier. This is due to the noise in the testing system. The manufacturers of PXI-1000B and EPA104 specified the excitation and sensing noise of around 0.1%. However, the noise is unbiased, so we can reduce the effect by averaging. Then we observed that the standard deviation of white noise has been reduced to 1mV during pre-trigger after averaging. If we have more repetitions, the

white Gaussian noise can be further eliminated, but we limited ourselves to only 10 repetitions because only 10 repetitions can have a SNR (infinity norm) of three for the smallest damage.

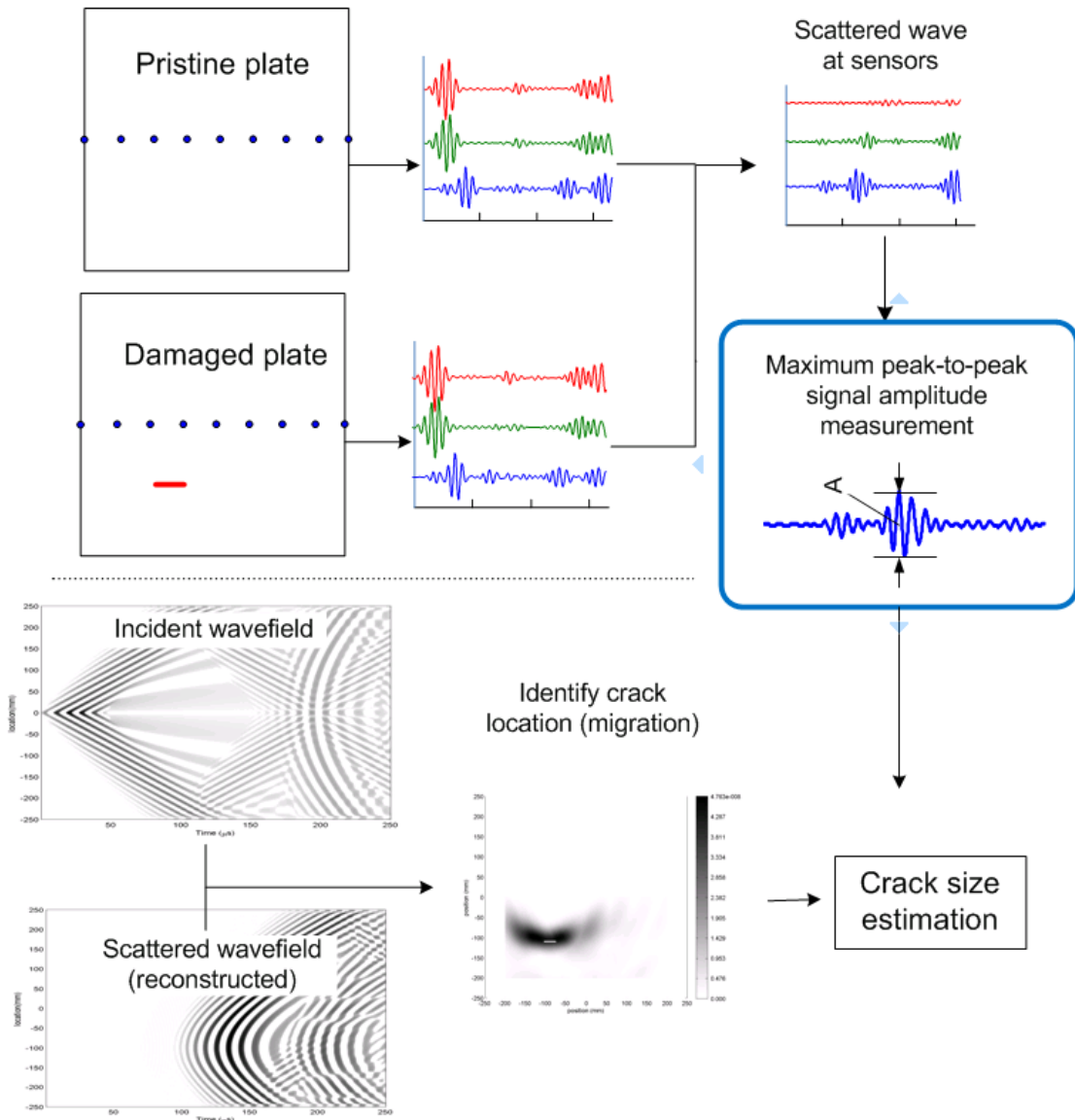


Figure 4-4. Test procedure for estimated location by migration technique and signal amplitude measurement

The scattered wavefield from the crack was obtained by subtracting the pristine plate signal from the signal from the damaged plate (Figure 4-4). Then, the maximum

peak-to-peak amplitude of the scattered signal was identified. In addition, the migration technique was used to create an image of the damage for an approximate location of the crack.

To determine the excitation frequency, a preliminary experiment was performed using an identical plate prior to actual testing. By using two piezoelectric transducers attached on the same location on the plate, but opposite sides through the thickness and a PZT sensor on the different location, we examined the amplitude difference due to different excitation frequencies. Because of the low value of the product of frequency and plate thickness, only the fundamental modes of symmetric and anti-symmetric waves, also known as  $S_0$  and  $A_0$  modes propagate in the plate.

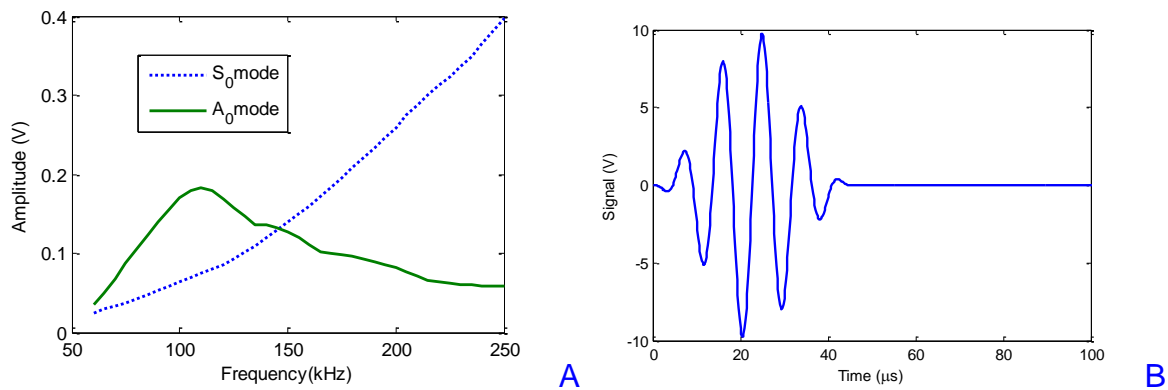


Figure 4-5. A) Frequency sweep experiment. Amplitudes of transmitted signal are shown for  $A_0$  mode and  $S_0$  mode. B) Five peaked toneburst excitation sent to the actuator (110 kHz)

In this study, only the  $A_0$  mode was used to examine the scattered signal since it has larger amplitude than  $S_0$  mode at the frequency of interest and is highly dispersive. The central frequency was chosen to be 110 kHz corresponding to the wavelength 27mm based on the result of this frequency-amplitude experiment, which gives the maximum amplitude of  $A_0$  mode excitation (Figure 4-5A). The five-peaked toneburst used for wave excitation is shown in Figure 4-5B.

## Results

### Scattered Signal from the Damage

In simulation, the transverse velocity is chosen as the sensing parameter at the corresponding nodes, and the maximum amplitude is proportional to the maximum strain or voltage at each piezoelectric transducer disc in the experiment. In both simulation and experiment, the scattered signal is obtained by subtracting the pristine plate signal from the damaged plate signal. Figure 4-6 displays a sample case when the crack size is 26 mm and the excitation point is at Actuator 4, which is located at the center of the plate (Figure 4-1).

In Figure 4-6, symmetry between left and right sides of actuator 4 was expected and observed in the simulation, but the experiment showed substantial asymmetry. This is attributed to differences in individual sensor quality and attachment uniformity. However, we have observed reasonable agreement between simulation and experiment in terms of time of flight (TOF) and scattered signal amplitude.

### Variation of the Signal with Crack Size

Maximum peak-to-peak amplitude of a signal represents the maximum strain energy transfer rate by the given signal. By examining the maximum peak-to-peak amplitude of the scattered signal, we can observe that the amplitude increases with crack size. Figure 4-7 shows the change in the scattered signal amplitude for two different crack sizes.

We have seven excitation sources, and for each excitation, eight sensors are used to examine the scattered signal. The highest peak-to-peak amplitude among all sensors and actuators is the maximum signal amplitude for each crack size. The maximum



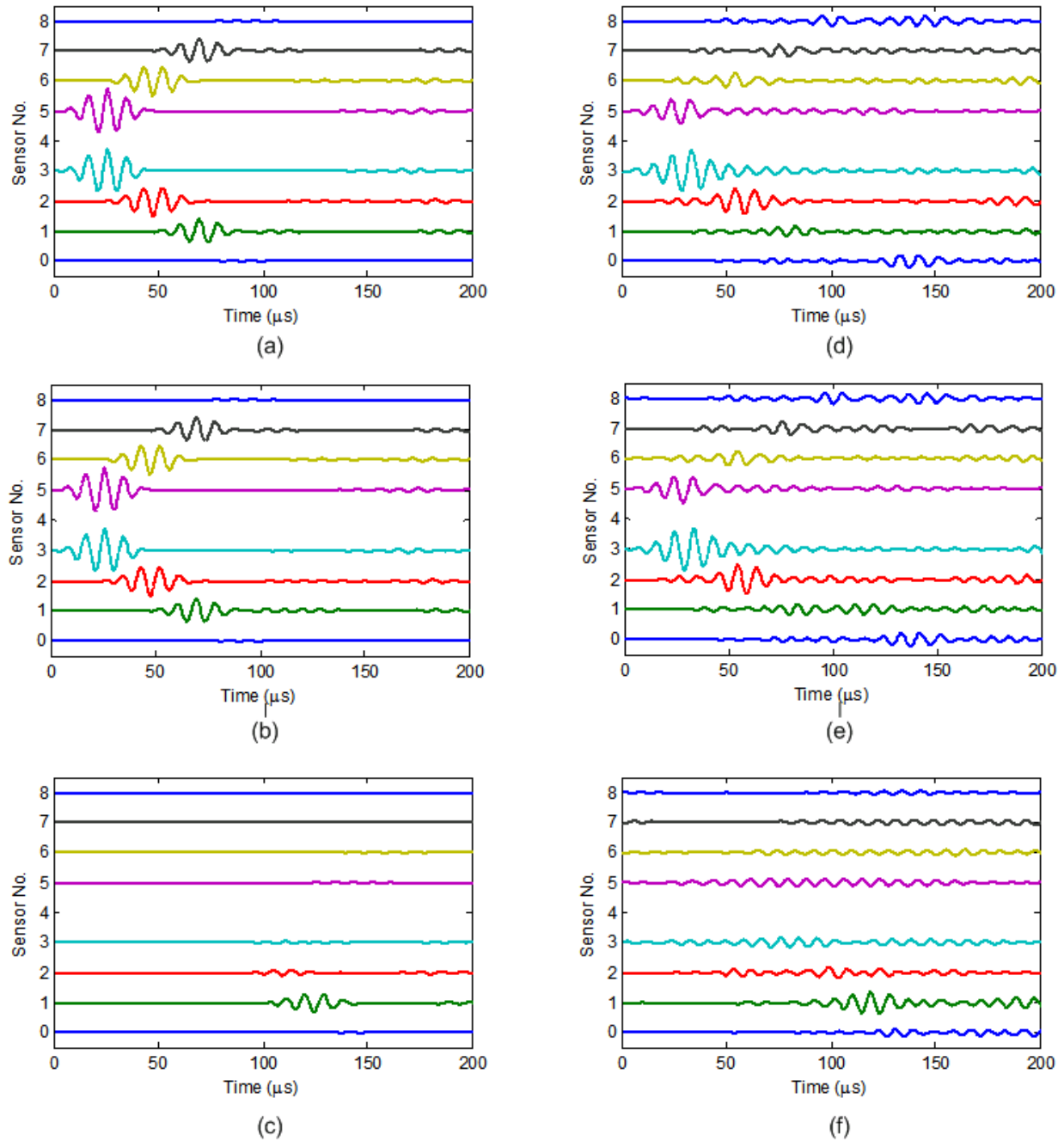


Figure 4-6. Toneburst excitation measured from all eight sensors from simulation (a, b, c) and experiment (d, e, f). Sensor spacing is 62.5 mm each. (a) pristine plate signal (b) damaged plate signal (c) scattered signal by subtracting (a) from (b). We can observe the scattered signal from the boundaries in experiment, but it is almost completely removed after subtraction. (d) pristine plate (e) damaged plate (f) scattered signal by subtracting (a) from (b) (Signal amplitude is adjusted for (c) and (f) because the scattered signal is much smaller than the healthy or damaged ones)

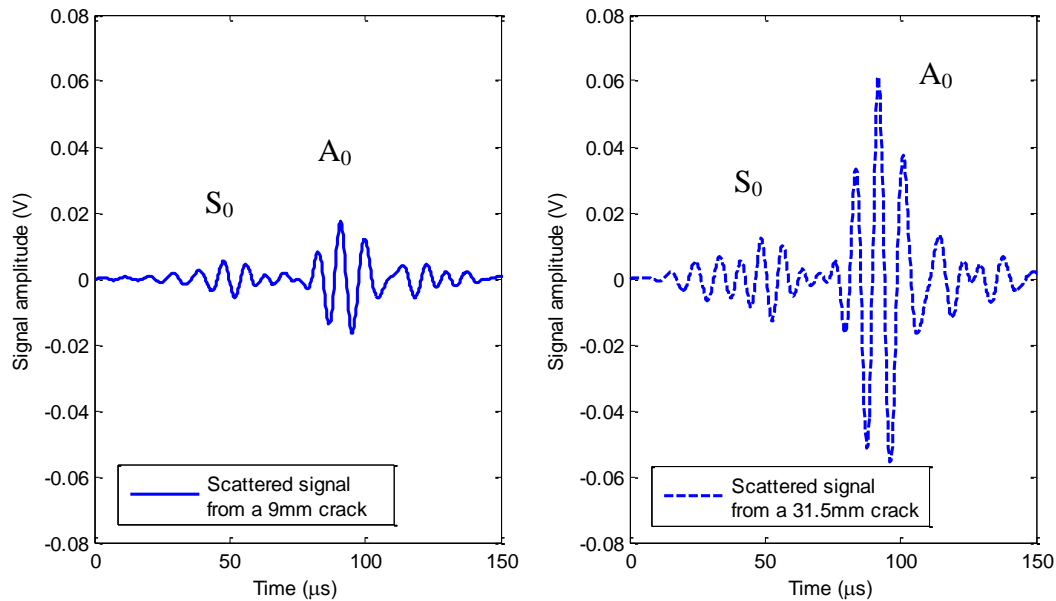


Figure 4-7. Experimental scattered signal amplitude change in different size cracks. A) 9 mm B) 31.5 mm

amplitude occurred usually at actuator 3 and sensor 2 for all crack sizes, except that for cracks sizes 2.5mm, 3mm, and 4.5mm it happened at actuator 4 and sensor 2. Due to difficulty in modeling the actuator and sensor interaction with the plate, normalized measured signals are compared to normalized signal velocities. Without loss of generality, the data are normalized with respect to the signal amplitude when the crack size is 25 mm. The comparison between normalized values of signal amplitude is presented in Figure 4-8. It can be seen that the relation is proportional to the crack size of 30 mm, and showed a good agreement between experiment and simulation.

The major observation in this experiment is that the signal amplitude increases with crack size up to a saturation point. This provides us a capability to monitor a crack growth up to a certain size.

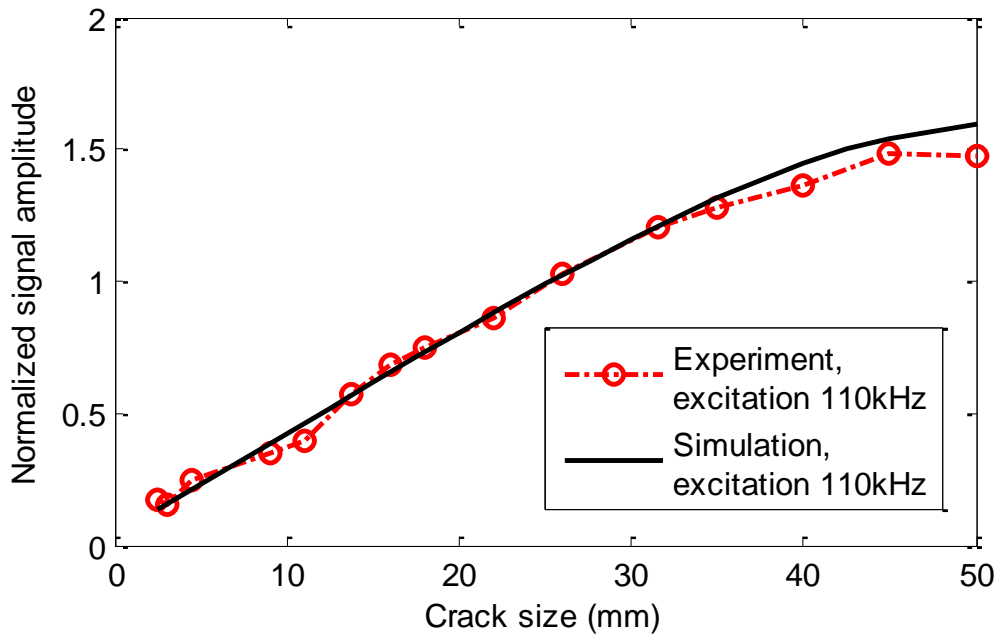


Figure 4-8. Signal amplitude variation (maximum peak-to-peak amplitude). The excitation frequency is 110 kHz and the signal amplitude is normalized using the signal at crack size 25 mm as the reference.

### Effect of Frequency

Figure 4-8 shows divergence of signal amplitudes between measurement and simulation when the crack size is longer than 30mm. To investigate this further, the experiment was repeated using a different excitation frequency. Since the signal from the experiment has both  $S_0$  and  $A_0$  mode, we examined individual signal to determine which is dominant. This is possible because  $S_0$  mode is significantly faster than  $A_0$  mode (Figures 4-7 and 4-9).

While the signal amplitude of  $S_0$  and  $A_0$  mode has similar magnitude for this central frequency, we observed that  $A_0$  mode amplitude is still larger than  $S_0$  mode in the scattered signal (Figure 4-9).

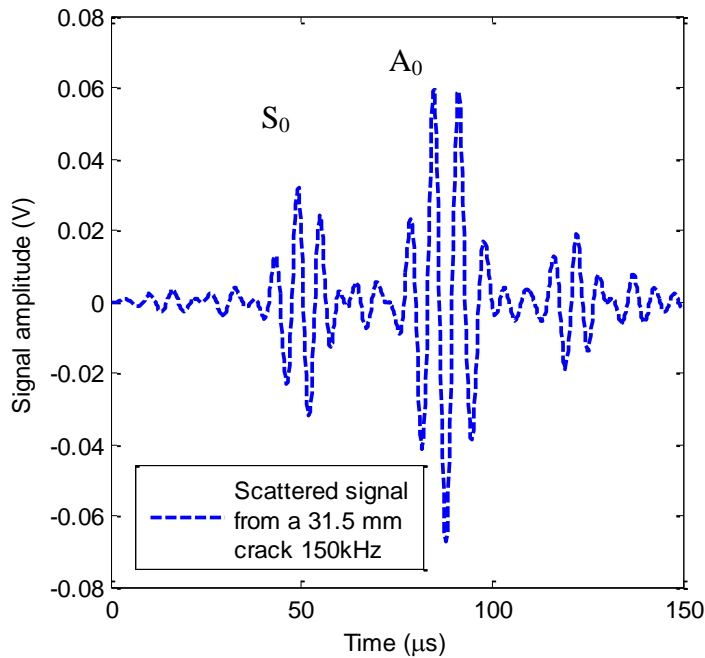


Figure 4-9. Scattered signal amplitude with 150kHz excitation.

The result, obtained at the same crack sizes with a different central frequency of 150 kHz, is presented in Figure 4-10. The amplitudes are normalized by the same scale factor as the previous result. In this case, the agreement between experiment and simulation was maintained up to crack size of 22 mm.

This time the separation between the two graphs occurs around 22mm. We speculate that is related to the wavelength (150 kHz,  $A_0$  mode wavelength  $\lambda \approx 20$  mm, and 110 kHz,  $\lambda \approx 27$  mm). Since all other conditions are identical and the group velocity of  $A_0$  mode propagation in the plate is almost the same for both frequencies, we concluded that the agreement may deteriorate for crack sizes larger than the wavelength. Since we have fixed excitation frequency, the crack size is a linear function of Helmholtz number. So we can also say that the scattered signal will change as a function of the Helmholtz number.

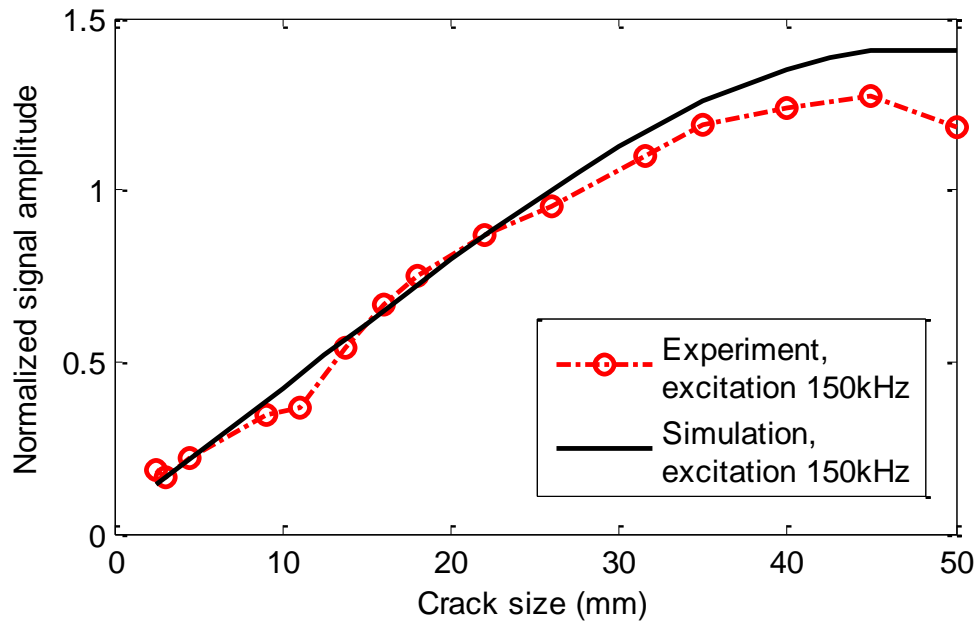


Figure 4-10. Signal amplitude variation (maximum peak-to-peak amplitude). The excitation frequency is 150 kHz and the signal amplitude is normalized using the same scale factor as Figure 4-8.

It is known that if Helmholtz number (the ratio of the crack size to the acoustic wavelength) is large, there is cutoff frequency where we cannot observe the increasing signal amplitude. The Helmholtz number for 110 kHz excitation to examine 30 mm crack is 1.11, and for 150 kHz excitation to examine 22 mm crack is 1.10. Theoretically, the cutoff Helmholtz number is 1.84 for a circular cavity which is of the same order of magnitude as our observation, so we concluded that as the Helmholtz number approaches its cutoff point, deviation between simulation and experiment begins to increase.

Also, the signal amplitude behavior beyond this point may be due to geometrical discrepancies; for example, the crack tested in the experiment is not perfectly straight. For longer cracks, the geometric variations are responsible for the change in the maximum amplitude by changing the amplitude along the directions of scattered waves.

In other words, we require more precise modeling for better agreement between simulation and experiment. The main reason that we do not discuss further on this effect is that we still can cover a wider range by changing the excitation frequency. However, when we are interested in long cracks, we can estimate the size by processing images obtained from migration technique or other techniques for general crack shapes. 11 mm crack also showed an abnormal result, but it is probably due to the transition from a circular hole to a hole plus a machined crack around that size.

### **Crack Location Effect**

We next investigated the effect of the relative location of the crack and the sensor array. Figure 4-11A shows two sensor arrays on a single plate and the simulation domain covered by each array. The crack is located at (-90mm, -110mm) from sensor 4 of array 1, while it is located at (-100mm, -140mm) from sensor 4 of array 2. The experiment for two different domains is essentially equivalent to cases for two different crack locations (Figure 4-11B). The behavior of maximum signal amplitude is predicted by simulation, and obtained from experiment. By using sensor array 2, we were able to obtain the signal amplitude for crack position 2, and compared it with the simulation results in Figure 4-12.

Since the distance from the sensor array is larger, the slope of peak-to-peak amplitude to the crack size is smaller compared to the previous experiment, but slightly larger than expected from the simulation. The sensors have some variability, so the sensors used later might be more sensitive than the one used in Figure 4-8. Therefore,

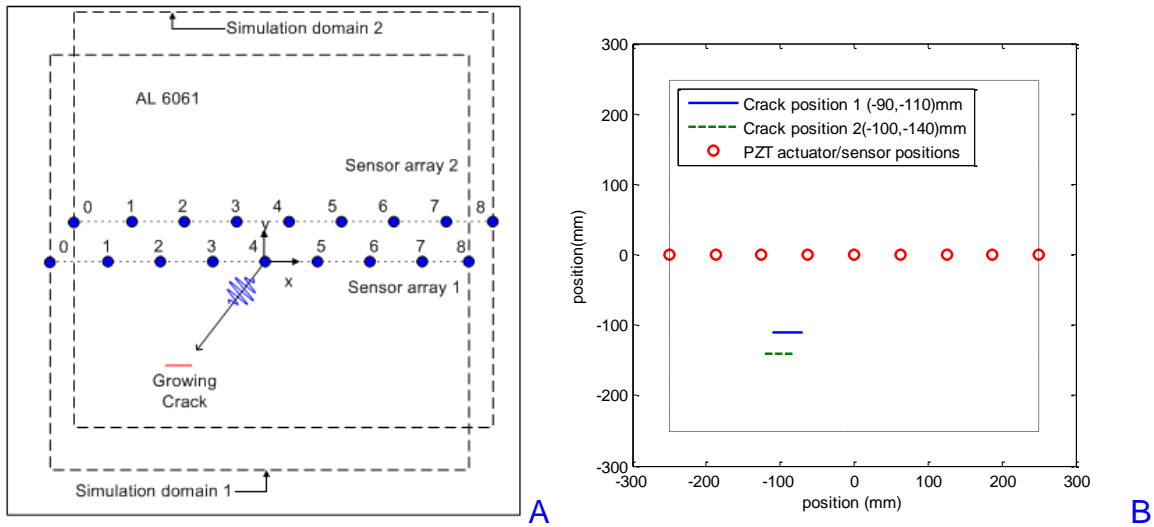


Figure 4-11. A) Two sets of sensors and the domains covered by each array B) Different crack center location with respect to the actuator positions: second crack center location is (-100mm, -140mm)

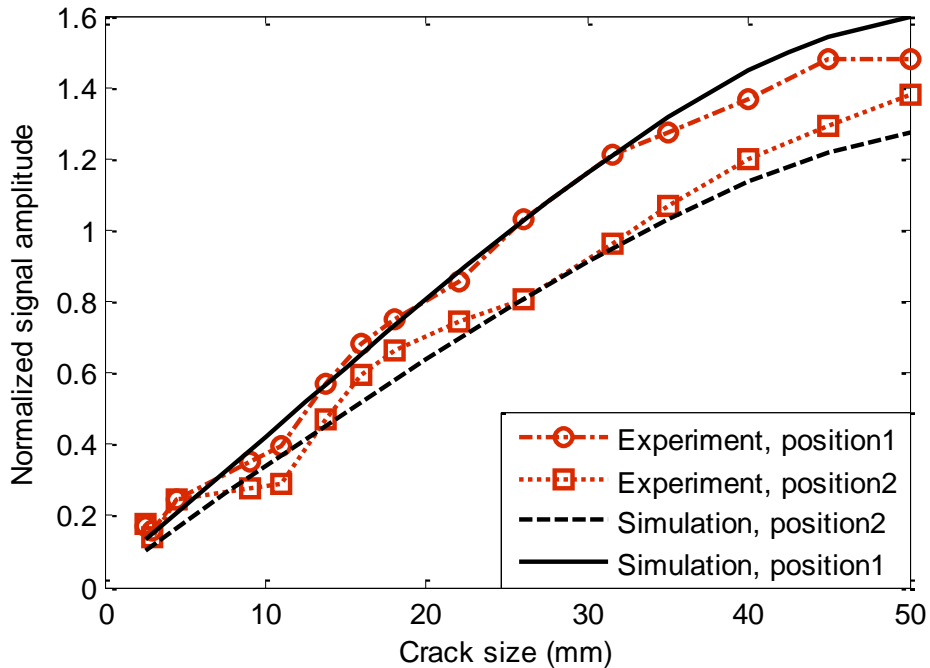


Figure 4-12. Scattered signal amplitude variation for cracks growing at a different location excited by 110 kHz ultrasonic toneburst. Signal amplitude comparison with result shown in Figure 4-8, simulation and experiment.

a different crack location as well as the sensors require a different calibration factor, which represents a different slope between crack size and signal amplitude. In our case, the factor is not calculated but we have performed another simulation to find more accurate relation. With the updated predicted behavior, we were able to find a linear relationship between signal amplitude and the crack size for the second location.

Since approximate crack location may be found by the migration technique, the calibration factor, or the coefficient for the linear relation, can also be found from that information. However, uncertainty in individual sensor characteristics and estimated location may be encountered during the procedure. To implement an SHM system to real-life structures, more research has to be done to overcome these difficulties.

### **Migration Technique with Experimental Data**

Chapter 3 discussed how we can identify crack location using simulated signal. With the same procedure, we can obtain images using experimental signal. In this case, we only have a limited number of sensors, so the scattered wavefield is reconstructed from the sensor signals by spline interpolation (Figure 4-13).

Figure 4-14 and 4-15 shows experimental results. Figure 4-14 shows the image obtained from one actuator and nine sensors. The final result is obtained by combining images in Figure 4-15 and Table 4-4.

Table 4-4. Comparison of different imaging methods

Imaging method	Estimated location (mm)	Error (mm)
Actual	-90.0, -110.0	-
Prestack migration	N/A	
Bayesian approach	-95.5, -104.0	8.14
Bayesian approach with signal decay compensation	-90.8, -106.2	3.88



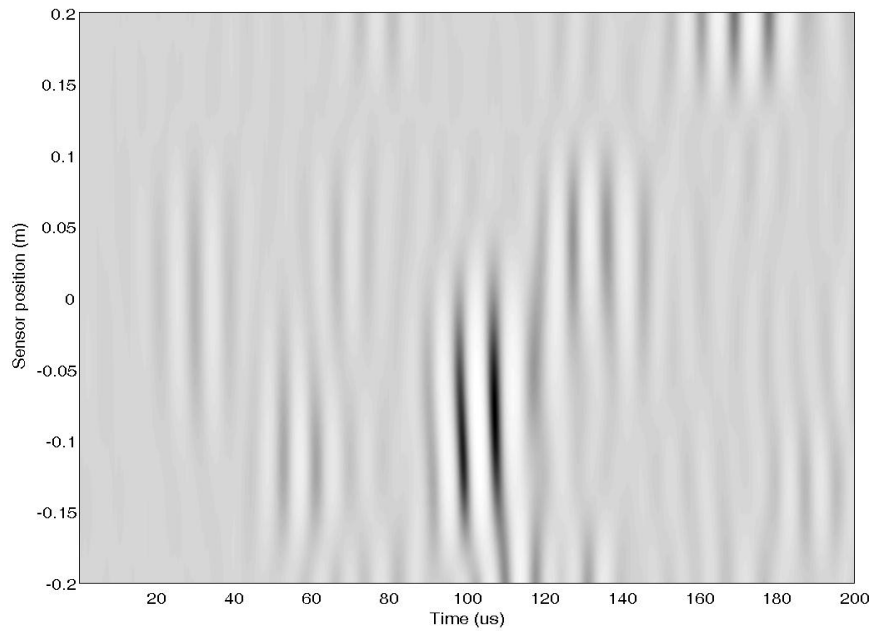


Figure 4-13. Reconstructed scattered wavefield

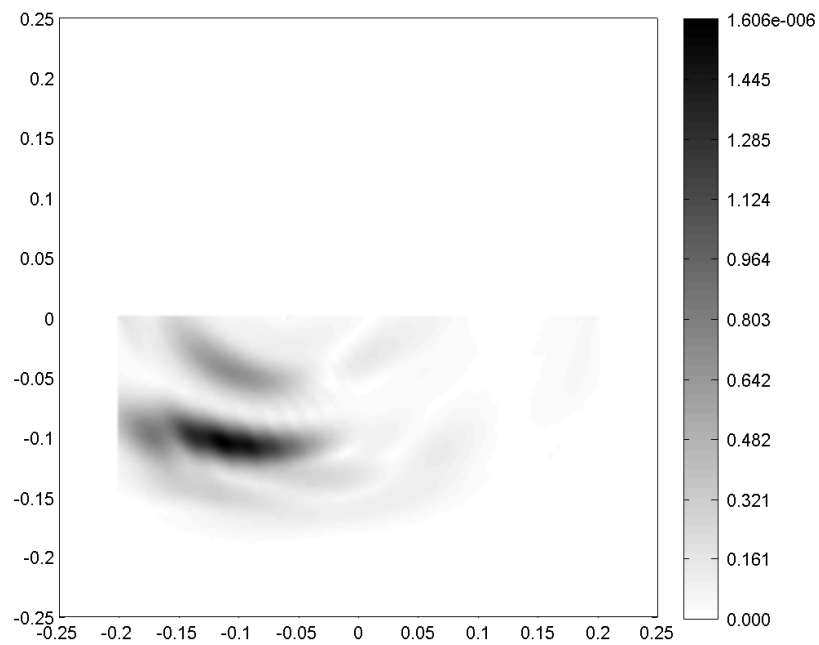
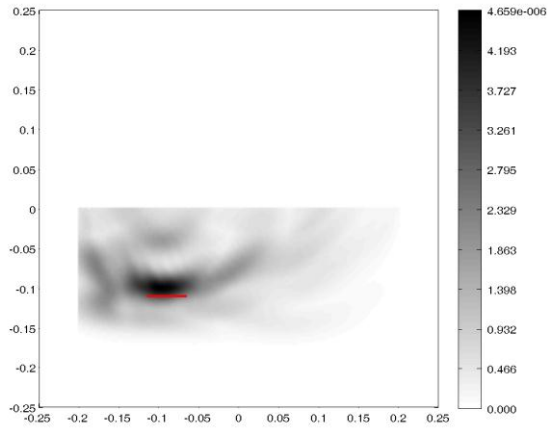
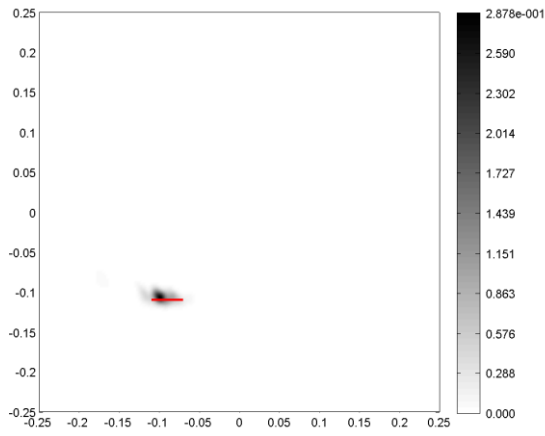


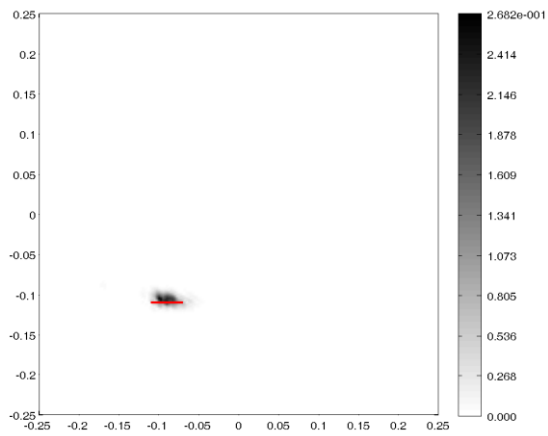
Figure 4-14. Experimental result is reproduced into image using migration technique. The crack size is 50 mm, and actuator position is at the center of the plate.



A



B



C

Figure 4-15. Combination of all 7 actuators available in the experiment. The crack size is 50mm. A) Prestack approach B) Bayesian approach C) Bayesian approach with signal decay compensation

Figure 4-15A uses migration technique described in Section 3.1. The image clearly indicates that there is damage, but the location is inconclusive. Figure 4-15B utilized the Bayesian approach suggested in Section 3.2, and we have a focused image where we can extract the coordinates of crack center. Figure 4-15C applied signal decay compensation (Section 3.3) on top of Bayesian approach (Section 3.2), and the estimated location is closer to the true crack center.

## CHAPTER 5 BAYESIAN APPROACH TO IMPROVE DIAGNOSIS FROM PAST PROGNOSIS

The goal of this chapter is to improve size estimation accuracy by taking advantage of previous prognosis. First, it is acknowledged that the measured crack size from SHM systems may have error and noise, which can be represented using a statistical distribution. With a series of inspection results available, we can make a prediction about how the crack will grow by the next inspection cycle using several methods. This can help narrow down the uncertainties involved in diagnosis by applying our knowledge from previous prediction of crack propagation. The procedure introduced in this chapter is very similar to the particle filtering approach [77, 78]. However, one difference is that the particle filtering generates crack size candidates and updates their weights for the next prior distribution, while this approach directly calculates the prior distribution using Monte Carlo Simulation.

Section 5.1 presents the crack propagation problem for fuselage panels, and Section 5.2 explains how to perform a Bayesian approach to take advantage of past prognosis. Section 5.3 presents the simulation results.

### **Modeling**

The fuselage is the main structure or body of the aircraft to which all other units attach. It provides space for the crew, passengers, cargo, most of the accessories, and other equipment (Figure 5-1). Typically, many panels are assembled together in the fuselage. However, when the airplane is under operation, it is subjected to a cyclic fatigue loading due to repeated pressurization. As a result, the number of cycles corresponds to the number of flights. Problem formulation for this low-cycle, high stress

fatigue is simplified by an infinite plane with uniform loading in one-direction (Figure 5-2).

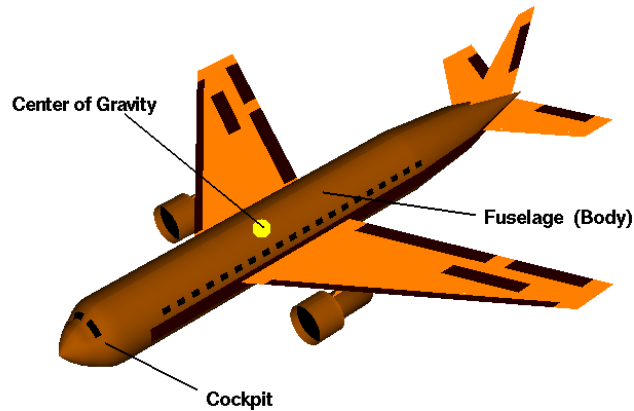


Figure 5-1. Aircraft fuselage

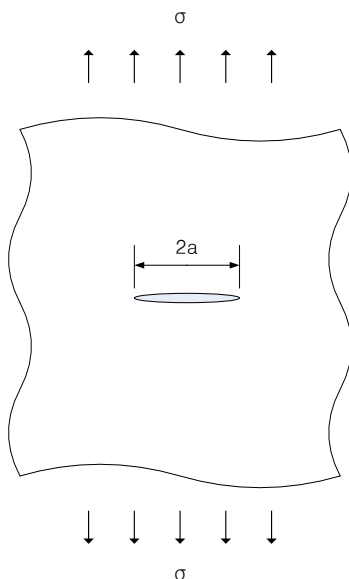


Figure 5-2. Simplified loading condition

A through-the-thickness center crack in a fuselage panel is considered. Since the pressurization is the major loading factor for a fuselage, the crack propagation can be considered as a low-cycle fatigue. Paris' law is used to model the true crack behavior during the simulation (Eq. 5.1).

$$\frac{da}{dN} = C\Delta K_I^m \quad (5-1)$$

where  $a$  is the half crack size,  $N$  is the number of loading cycles (treated as a real number),  $\Delta K = \Delta\sigma\sqrt{\pi a}$  is the range of stress intensity factor,  $\Delta\sigma$  is the difference between maximum and minimum applied stress, and  $C$  and  $m$  are crack propagation parameters related to material properties and geometry.

We also assume that the material has inherent defects, or micro cracks within the structure where the crack starts growing from them. With the parameters given in Table 5-1, the true crack propagation is modeled by the solution of the Paris' law as shown in Eq.5-2 and Figure 5-3. Note that the crack size  $a(N)$  shown in Eq.5-2 is a half crack size.

$$a(N) = \left( NC\left(1 - \frac{m}{2}\right)(\Delta\sigma\sqrt{\pi})^m + a_i^{1-\frac{m}{2}} \right)^{\frac{2}{2-m}} \quad (5-2)$$

Table 5-1. Parameters related to simulated crack propagation.

Parameters	Value
Initial flaw size, $a_i$	1 mm
Minimum detectable crack size	6 mm
Maximum allowable crack size	50 mm
Crack propagation parameter, $C$	$2.0 \times 10^{-10}$
Crack propagation parameter, $m$	3.7
Applied stress $\Delta\sigma$	78.63 MPa
SHM Inspection interval	50 cycles
First detection	34,300 cycles
Total life	42,300 cycles

The minimum detectable crack size of SHM is larger than that of manual inspection. In ultrasonic testing, the minimum size is about a half of the wavelength of the excitation wave [5]. Since there are practical limitations of the excitation frequency

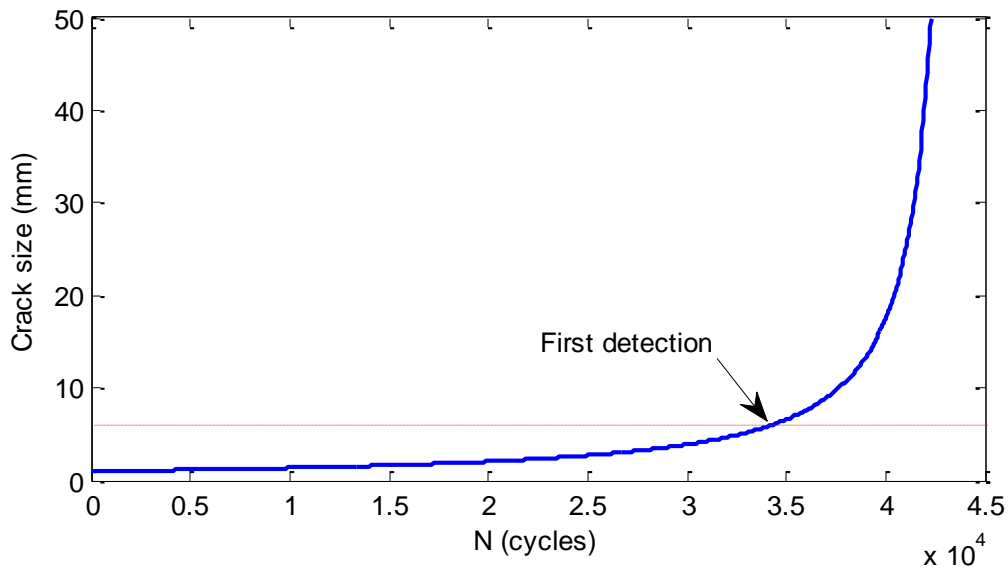


Figure 5-3. Crack propagation. We assumed that the crack is first detected when it is bigger than 6mm.

that we can use, the minimum detectable crack size that we can use is around 5 ~ 10 mm. Therefore, we assumed that the minimum detectable crack size to be 6 mm for this research. After the detection returns a positive signal, the crack will be monitored until it is sent for maintenance, which is defined to be 50 mm in crack size. In this research, the probability of detection is not considered.

Uncertainty in the detected crack size varies widely by inspection methods, data processing techniques, and associated noise with the procedure. In this research, we consider the uncertainty induced by white noise in the signal, which is unbiased. In general, it is known that the uncertainty of the detected size is larger when the crack is large [35,72], so this chapter models the ratio between true crack size and inspected crack size by a lognormal distribution which has mean value 1 and coefficient of variation 0.1 (Eq.5-3).

$$a_{inspected} / a_{true} \sim \text{LogN}(-0.005, 0.1^2) \tag{5-3}$$

Using this distribution, one sample of a series of detected crack size at each inspection event is shown in Figure 5-4. Although the general trend follows the true crack growth (green line), individual measured crack sizes are often quite different from the true one. The objective is to improve the measured crack size information by using predicted crack size information from the previous measurement.

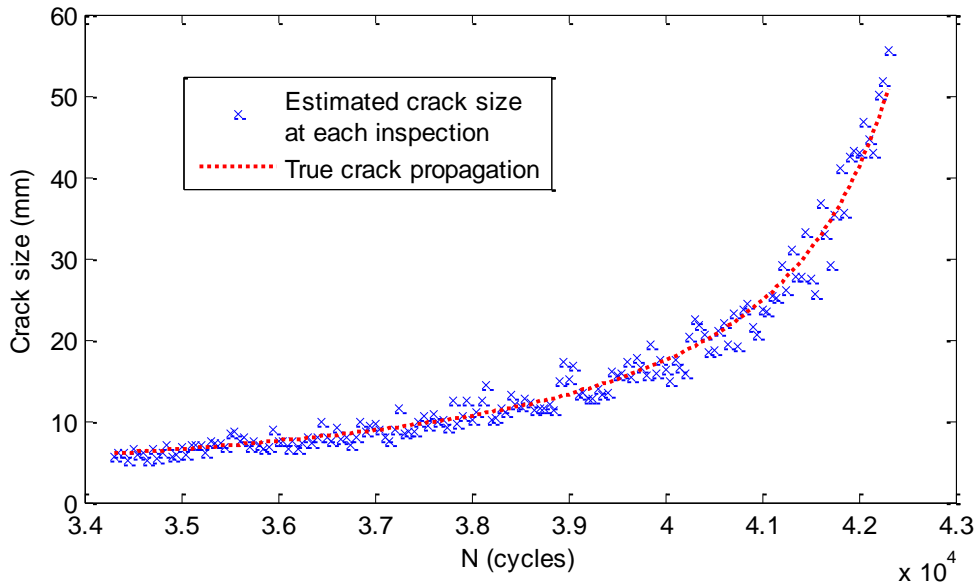


Figure 5-4. Sample of detected estimated crack sizes (based on Eq.5-3)

### Improved Diagnosis by using Bayesian Approach

Our objective is to estimate more accurate crack length by combining previous inspection result with current inspection result. Rewriting the formula suitable for our purpose, we can write an equation about estimating crack size from inspection as follows:

$$f_a(a_{poss} | a = a_m) = \frac{f(a_{poss})l(a_m | a = a_{poss})}{\int_0^{\infty} f(a_{poss})l(a_m | a = a_{poss})da} \quad (5-5)$$



where  $a_m$  is the measured crack size from the inspection, and  $a_{poss}$  is a possible crack length.  $l(a_m | a = a_{poss})$  is the likelihood function, which is the value of probability density to have  $a_m$  given that the true crack size being  $a_{poss}$ . The prior distribution  $f(a_{poss})$  is the result from the prognosis based on previous inspections.

Using Eq.5-5, we can improve the accuracy of current crack size estimation. The posterior distribution from Eq.5-5 is used for prognosis for the next inspection cycle by propagating it using Eq.5-2. As the data accumulates, we will have a better prior for the next inspection. For the subsequent construction of prior distribution, the distribution of estimated true crack size until the previous inspection is substituted into the propagation model. This is shown in Eq.5-6.

$$f(a_{poss}) = f_a(a_{poss}(N) | a = a_m) \quad (5-6)$$

where  $a_{poss}(N)$  is the crack size after N cycles.

Figure 5-5 illustrates this procedure using a large step ( $\Delta N=2500$ ) for clearer demonstration. In the actual simulation, we assumed that the inspection interval is 50 cycles. When the first detection result is 6 mm with 10% uncertainty, the distribution of crack size follows the solid curve in Figure 5-5A. To calculate the probability density, we used Monte Carlo simulation (MCS). First, a set of random crack sizes following the posterior distribution is generated and each is propagated by  $\Delta N$  using Eq.5-2. Then, the probability density is found by counting the number of samples (dotted curve).

At the next inspection, the measured crack size is 8 mm, and the uncertainty in measurement is interpreted by the likelihood function as in Eq. 5.7.

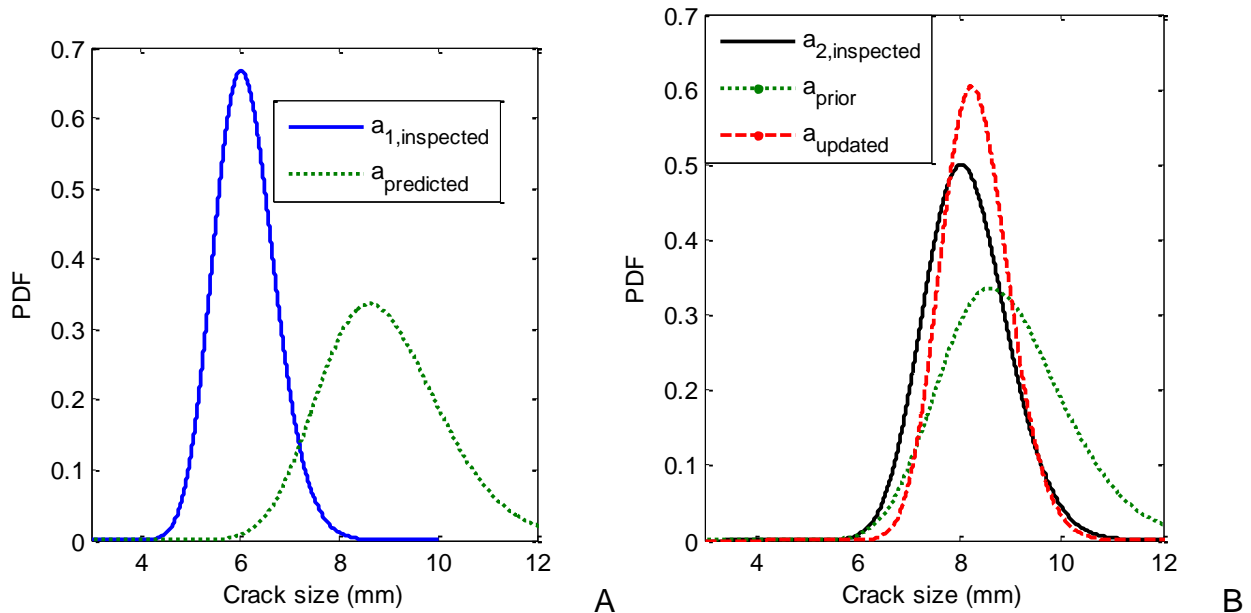


Figure 5-5. Simulation procedure A) Predicted probability distribution of crack size B) Predicted distribution is used as a prior for the next inspection. Posterior distribution is calculated by combining current inspection result and the prior distribution.

$$l(a_m | a = a_{poss}) = LN(a_m; \ln(a), 0.1) \quad (5-7)$$

where  $LN$  indicates the probability density function of a log-normal distribution. This explains that the likelihood is equivalent to the probability density that we will have our current measurement  $a_m$  if the true crack size is  $a$  for a range of values of  $a$ . By combining the likelihood with the prior distribution, we have an updated distribution about current crack size as in Figure 5-5B.

### Constructing Prior Distribution using Different Prognosis

Prognosis is a process of predicting the future behavior, which adds uncertainties to the initial measurement uncertainty. There are many approaches for predicting crack propagation from current measurements. To examine the effect of the prognosis model, we selected four cases of possible prognosis. First, we select a case of perfect

prognosis when we know the exact crack propagation model with accurate parameters. Second case is when our prognosis model is accurate, but the parameters are uncertain. The third case is the same as the second case, but we use a least square fit instead of uncertainty propagation via Monte Carlo simulation. Finally, we model a case where we have a crack growth model, not based on any physics, but on fitting a quartic polynomial to past measurements and extrapolation. Note that an interpolation scheme such as spline cannot be used in this research because we need confidence interval for the approximation to construct the prior distribution.

### **Perfect Prognosis**

We first discuss a case where we have a confidence in our failure prediction model, which is Paris law with parameters given in Table 5-1. In this example, the only uncertainty is the uncertainty of measurements. The inspection is performed every 50 cycles after the first detection. The probability distribution function (pdf) for the possible true crack size is constructed and updated at every inspection cycle. The evolution of the posterior pdf of crack sizes is shown in Figure 5-6.

When the crack propagates, the standard deviation increases as well because the noise is proportional to the crack size. Also, the crack propagates faster as the crack size increases. As a result, we can observe a wider posterior distribution when the crack is large. The estimated crack size at each inspection is the modal value of the corresponding pdf curve. The estimated crack size along the inspection cycle is shown in Figure 5-7.

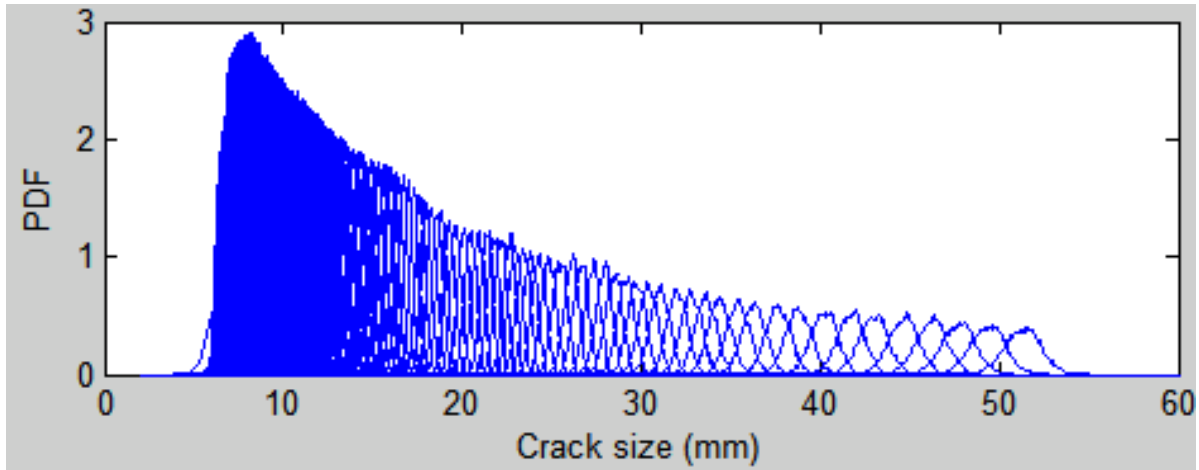


Figure 5-6. Probability distribution function of crack size updated at every 50 cycles

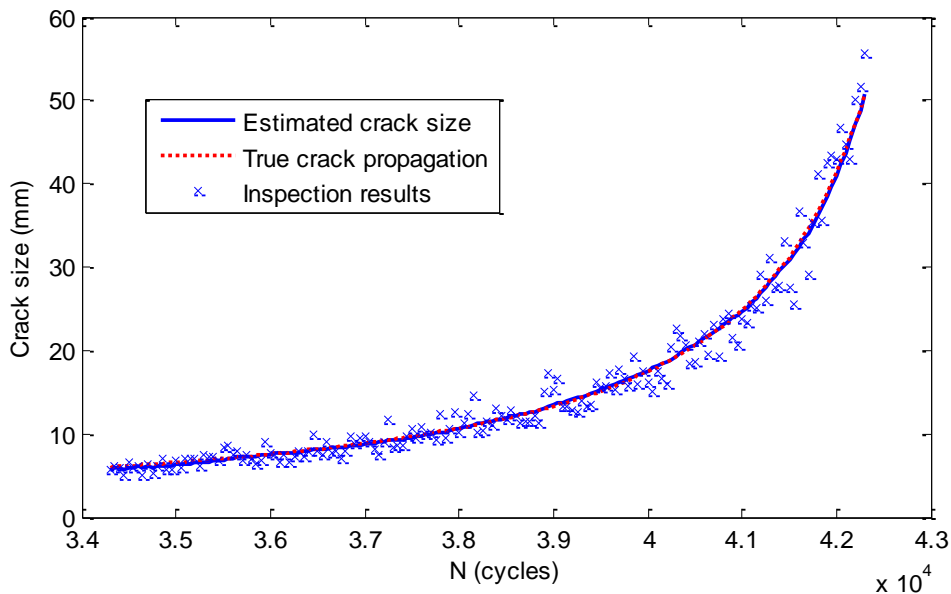


Figure 5-7. Crack size found by Bayesian update

Although the final crack size distribution was wide in Figure 5-6, the estimated crack size is fairly close to the true crack size curve.

### Uncertainty in Crack Propagation Parameters

The distribution of the Paris law parameters  $m$  and  $C$  can be fairly wide to begin with, but we assume that it has been narrowed based on crack propagation in the present or similar panels (e.g. using the method of [73]) to:

$$m \sim N(3.7, 0.1^2)$$

$$\log C \sim N(\log(2 \times 10^{-10}), 0.2^2) \quad (5-8)$$

For this prognosis model, MCS is also used to evaluate the prior distribution with random values of C and m. The change in the updated distribution indicating possible crack size is shown in Figure 5-8.

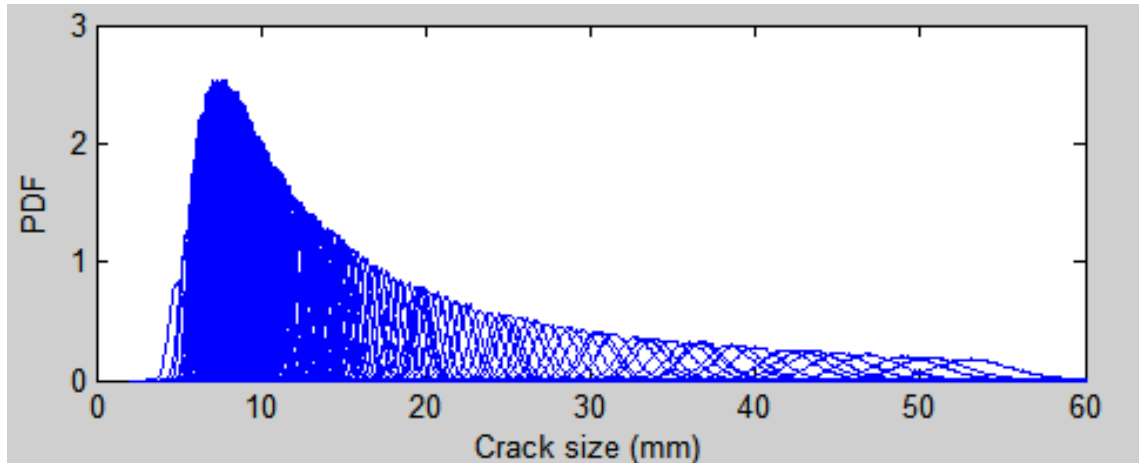


Figure 5-8. Probability distribution function of crack size updated at every 50 cycles with uncertain parameters C and m.

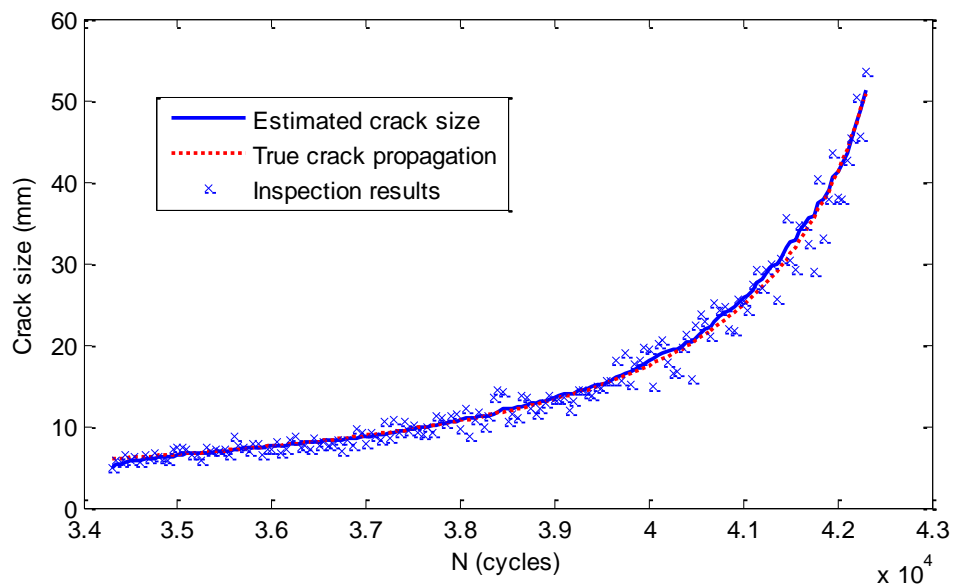


Figure 5-9. Crack size found by Bayesian update with uncertain C and m

In this case, the resulting posterior distribution is much wider than the previous case due to the increased uncertainty in the prediction. The estimated crack size at each inspection is the modal value of the corresponding probability distribution. The estimated crack size along the inspection cycle is shown in Figure 5-9. We can see that these modal values still provide accurate estimates of crack sizes.

### Prognosis using Least Squares Fit of Paris Law

Probably the simplest approach to do the prognosis, is using a least square fit the initial crack size and the parameters in Paris law based on the solution of Eq.5-1 given as:

$$a(N) = \left[ NC \left( 1 - \frac{m}{2} \right) (\Delta\sigma\sqrt{\pi})^m + a_i^{1-m/2} \right]^{\frac{2}{2-m}} \quad (5-9)$$

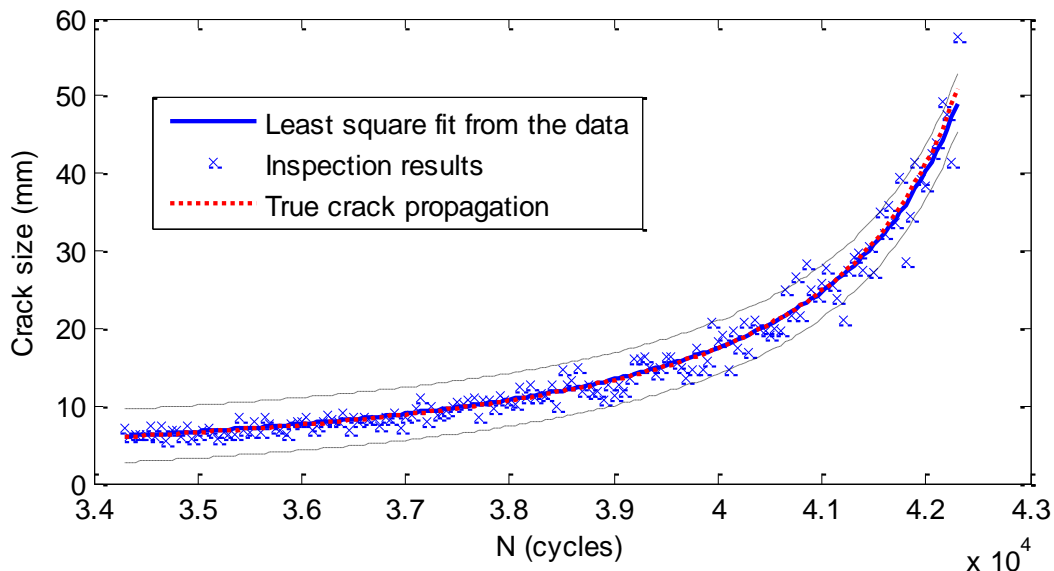


Figure 5-10. Approximation of the inspection data by Least squares fit of Paris law with 95% prediction bounds.

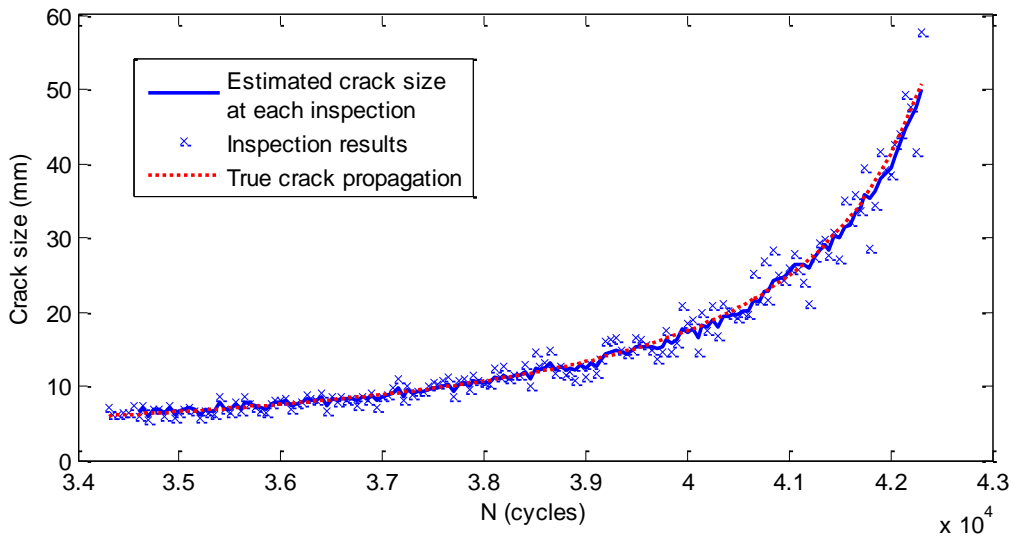


Figure 5-11. Estimated crack size by least square fitting of Paris law at each inspection cycle

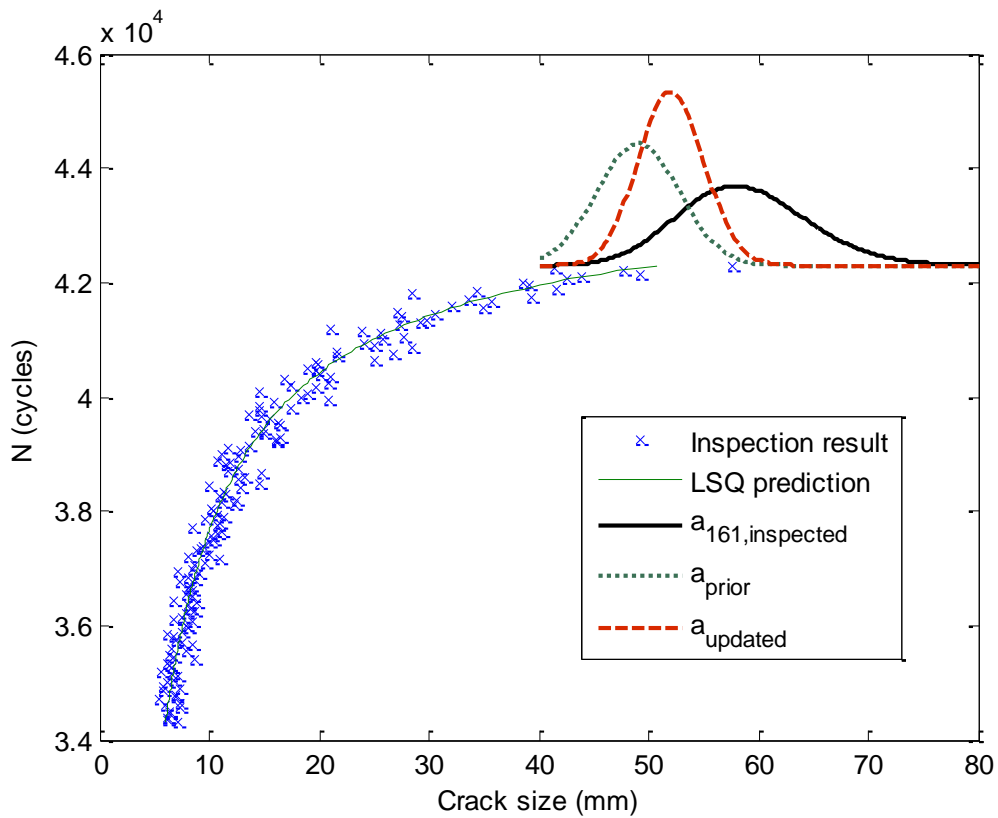


Figure 5-12. Demonstration of the suggested method to estimate crack size by Bayesian approach using prognosis based on least squares

Here we assume that we know C and the uncertainty is only in the initial crack size and the parameter m. Figure 5-10 shows results of the least-squares fit along with 95% prediction bounds. Figure 5-11 shows how the raw predictions of the least squares fit are improved by the proposed approach. At each inspection, the prior distribution is constructed using data up to that point, and combined with current inspection result to estimate the crack size. By constructing the prior distribution assuming that the least squares fit error follows a normal distribution, we can update the current measurement with the given prior distribution. The procedure is explained with Figure 5-12, which shows also the probability distributions at the last measurements.

Note that the abscissa and ordinate are switched for demonstration, the updated distribution is estimated by combining the prediction ( $a_{prior}$ ) and current measurement ( $a_{161, measured}$ ) using Bayesian approach as shown in Figure 5-5B.

### **Prognosis using Least Squares (Non-Physics Model)**

If we assume a case where we do not have any physical model for predicting the propagation of crack, the simplest approach is to extrapolate crack growth by curve fitting the measurement history. Here we employ a 4<sup>th</sup> order polynomial

$$a(N) = a_4N^4 + a_3N^3 + a_2N^2 + a_1N + a_0 \quad (5-10)$$

The procedure is exactly the same as explained in the previous case, except that the curve fitting is done based on the 4<sup>th</sup> order polynomial instead of Paris' law. To compensate the effect of imprecise curve at the early inspection result, only the 40 most recent inspection data were used to evaluate the least square fit. A single example with



the same set of data as the previous section is shown in Figure 5-13. Figure 5-13 also shows the prediction bounds for the curve fitting.

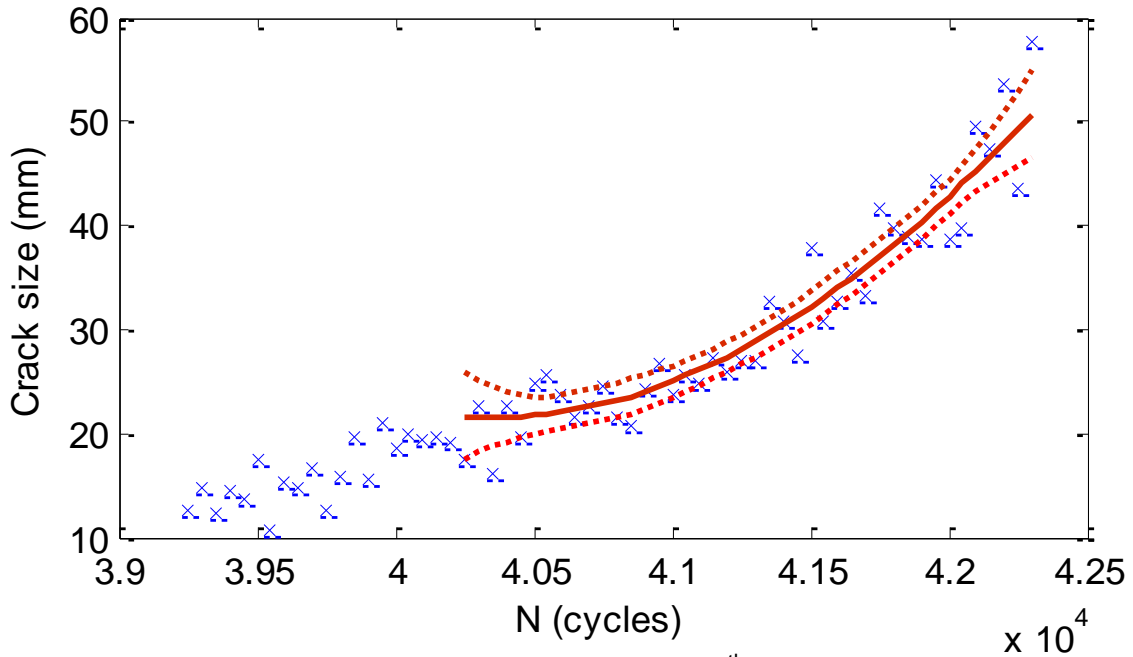


Figure 5-13. Approximation of the inspection data by 4<sup>th</sup> order polynomial with 95% prediction bounds. Only 40 recent data are used for curve fitting.

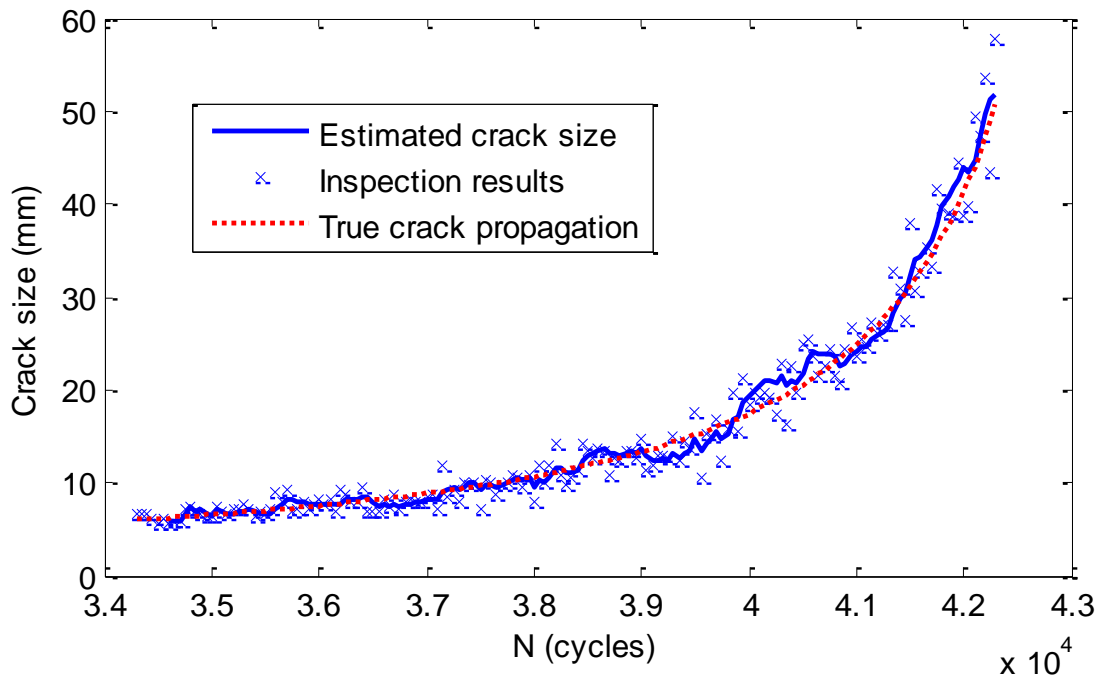


Figure 5-14. Estimated crack size by least square fitting using a quartic polynomial at each inspection cycle

Figure 5-14 shows the estimated crack size at each inspection occasion using suggested approach. To check the accuracy of suggested fit, we have run multiple cases to estimate the accuracy of our estimation.

To summarize the impact on diagnosis caused by past prognosis, we have run 10000 Monte Carlo Simulation with inspection uncertainty, and Table 5-2 summarizes the result.

Table 5-2. Comparison of accuracy with 10000 MCS

	Estimated value (Mode, most probable value)	Standard deviation of estimation
Single inspection	50.8 mm	5.08 mm
1. Perfect prognosis	50.8 mm	0.98 mm
2. With uncertainty of parameters	50.8 mm	1.48 mm
3. Least square fit of Paris law prognosis	50.6 mm	1.55 mm
4. Data-driven (quartic polynomial) Least squares	50.5 mm	2.72 mm

All cases employing past prognosis significantly reduce the standard deviation of the estimation. We have a noticeable difference in the estimated value for the data-driven case caused by the application of approximate model. However, we can take advantage in the predicted confidence interval even for that case.

For an implemented SHM system, we can perform the inspection as many as we want. If we reduce our inspection interval to  $\Delta N=25$  cycles, the accuracy can be improved further. Table 5-3 shows the result.

Since we have more data available for analysis, the standard deviations for all cases are reduced compared to the results shown in Table 5-2.

Table 5-3. Comparison of accuracy with 1000 MCS when  $\Delta N=25$  cycles

	Estimated value (Mode, most probable value)	Standard deviation of estimation
Single inspection	50.8 mm	5.08 mm
1. Perfect prognosis	50.8 mm	0.69 mm
2. With uncertainty of parameters	50.8 mm	1.11 mm
3. Least square fit of Paris law prognosis	50.6 mm	1.18 mm
4. Data-driven (quartic polynomial) Least squares	50.5 mm	2.02 mm

## CHAPTER 6 CONCLUSION

The major objective of structural health monitoring (SHM) is to identify the damage more accurately (diagnosis) to enable better prediction of its remaining useful life (prognosis). Unlike manual inspections, SHM can trace damage as it grows. This provides an opportunity for better prognosis, but it may also provide more accurate diagnosis because crack growth provides information on crack size evolution. Our objective was to integrate prognosis into diagnosis to improve diagnostic accuracy. Even though prognosis is the process of estimating remaining useful life by predicting crack propagation, it can also be applied to future diagnosis to improve overall accuracy. The first part of this research is about estimation of crack size when the crack location is known, followed by how we can obtain the crack location through the migration technique. At this point, we can evaluate the crack size with a single inspection, but it contains uncertainty of detection. The remainder of this research explains how we can benefit from the result of the past prognosis for accuracy of current estimation. By Bayesian approach, we were able to reduce the standard deviation of current estimate by 80%. This means that the inspection result is less affected from the large inspection error of SHM. We showed and compared many different prognosis methods including data-driven approach, and all of them improved the precision of current diagnosis in terms of standard deviation.

## LIST OF REFERENCES

1. Goranson, U.G. (1997). "Fatigue issues in aircraft maintenance and repairs," *International Journal of Fatigue*, Vol. 20, No. 6, pp. 413–431
2. Wanhill, R.J.H. (1994). "Damage tolerance engineering property evaluations of aerospace aluminum alloys with emphasis on fatigue crack growth," *National Aerospace Laboratory NLR, Amsterdam, Technical Publication NLR TP 94177 U*
3. Federal Aviation Administration (2007). "Civil aviation regulations part 5 – Airworthiness," Ver. 2.5
4. Papazian, J.M., Anagnostoua, E.L., Engela, S.J., Hoitsmaa, D., Madsena, J., Silbersteina, R.P., Welsha, G., and Whitesidea, J.B. (2009). "A structural integrity prognosis system," *Engineering Fracture Mechanics*, Vol. 76, Issue 5, pp. 620–632.
5. Worden, K., Farrar, C.R., Manson, G., and Park, G. (2007). "The Fundamental Axioms of Structural Health Monitoring," *Philosophical Transactions of the Royal Society: Mathematical, Physical & Engineering Sciences*, Vol. 463, pp.1639–1664
6. Ihn, J.B. and Chang, F.K. (2004). "Detection and monitoring of hidden fatigue crack growth using a built-in piezoelectric sensor/actuator network: I. Diagnostics," *Smart Materials and Structures*, Vol.13, No.3, pp.609–620
7. Sohn, H., Farrar, C.R., Hemez, F.M., Czarnecki, J.J., Shunk, D.D., Stinemates, D.W. and Nadler, B.R. (2004). "A Review of Structural Health Monitoring Literature: 1996–2001," *Report Number LA-13976-MS, Los Alamos National Laboratory*, Los Alamos, NM.
8. Giurgiutiu, V. (2008). "Structural health monitoring with piezoelectric wafer active sensors," Academic Press
9. Raghaven, A. and Cesnik, C.E.S. (2007). "Review of guided-wave structural health monitoring," *The Shock and Vibration Digest*, Vol. 39, No. 2, pp. 91–114
10. Giurgiutiu, V. and Cuc, A. (2005). "Embedded NDE for structural health monitoring, damage detection, and failure prevention," *Shock and Vibration Reviews, Sage Pub.*, Vol. 37, No. 2, pp. 83–105
11. Bourasseau, N., Moulin, E., Delebarre, C., and Bonniau, P. (2000). "Radome health monitoring with Lamb waves: experimental approach," *NDT&E Int.* Vol. 33, pp. 393–400

12. Doebling, S.W., Farrar, C.R., and Prime, M.B. (1998). "A summary review of vibration-based damage identification methods," *The Shock and Vibration Digest*, Vol. 30, No. 2, pp. 91–105
13. Montalvão, D., Maia, N.M.M. and Ribeiro, A.M.R. (2006). "A Review of Vibration-based Structural Health Monitoring with Special Emphasis on Composite Materials," *The Shock and Vibration Digest*, Vol. 38, pp.295–324
14. Zou, Y., Tong, L., and Steven, G.P. (2000). "Vibration-based model-dependent damage (delamination) identification and health monitoring for composite structures – a review," *Journal of Sound and vibration* Vol. 230, No.2, pp. 357–378
15. Sodano, H.A. (2007). "Development of an Automated Eddy Current Structural Health Monitoring Technique with an Extended Sensing Region for Corrosion Detection," *Structural Health Monitoring*, Vol. 6, No. 2, pp. 111–119
16. Banks, H.T., Joyner, M.L., Wincheski, B. and Winfree, W.P. (2002). "Real time computational algorithms for eddy-current based damage detection," *Inverse Problems*, Vol. 18, No.3, pp. 795–823
17. Zhou, G. and Sim, L.M. (2002). "Damage detection and assessment in fibre-reinforced composite structures with embedded fibre optic sensors—review," *Smart Materials and Structures*, Vol. 11, pp. 925–939
18. Doebling, S.W., Farrar, C.R., Prime, M.B., and Shevitz, D.W. (1996). "Damage identification and health monitoring of structural and mechanical systems from changes in their vibration characteristics: a literature review," *Los Alamos Report LA-13070-MS*
19. Pai, P.F., Young, L.G. and Lee, S.Y. (2003). "A dynamics-based method for crack detection and estimation," *Structural Health Monitoring*, Vol. 2, No. 1, pp. 5–25
20. Cai, Z., Li, H., Lin, J., and Lin, J. (2008). "Eddy current non-destructive testing application research of marine engines," *17<sup>th</sup> World Conference on Nondestructive Testing*, Shanghai, China
21. Ihn, J. B. and Chang, F. K. (2008). "Pitch-catch Active Sensing Methods in Structural Health Monitoring for Aircraft Structures," *Structural Health Monitoring* Vol. 7, No. 1, pp. 5–19
22. Sohn, H. and Law, K. H. (1997). "A Bayesian probabilistic approach for structure damage detection," *Earthquake Engineering and Structure Dynamics*, Vol. 26, No. 12, pp. 1259–1281

23. Sohn H., Park, G., Wait, J.R., Limback, N.P., and Farrar, C.R. (2004). "Wavelet-based active sensing for delamination detection in Composite Structures," *Smart Materials and Structures*, Vol. 13, No. 1, pp. 153–160
24. Balageas, D.L. (2002). "Structural health monitoring R&D at the European Research Establishments in Aeronautics (EREA)," *Aerospace Science and Technology*, Vol. 6, pp. 159–170
25. Gray, J., Tillack, G.R. (2001). "X-ray imaging methods over the last 25 years - new advances and capabilities," *Review of Progress in Quantitative Nondestructive Evaluation*, vol. 20, pp. 16–32.
26. Boller, C. (2001). "Ways and options for aircraft structural health management," *Smart Materials and Structures* Vol. 10, pp. 432–440
27. Achenbach, J.D. (2000). "Quantitative nondestructive evaluation," *International Journal of Solids and Structures* Vol. 37, pp. 13–27
28. Cheeke, J.D.N. (2002). "Fundamentals and Applications of Ultrasonic Waves," CRC Press, Boca Raton
29. Douka, E., Loutridis, S., and Trochidis, A. (2004). "Crack identification in plates using wavelet analysis," *Journal of Sound and Vibration*, Vol. 270, pp.279–295
30. Kim, J.T., Ryu, Y.S., Cho, H.M., and Stubbs, N. (2003). "Damage identification in beam-type structures: frequency-based method vs mode-shape-based method," *Engineering Structures*, Vol. 25 pp.57–67
31. Malinowski, P., Wandowski, T., Trendafilova I. and Ostachowicz, W. (2009). "A Phased Array-based Method for Damage Detection and Localization in Thin Plates," *Structural Health Monitoring* Vol.8, pp.5–15
32. Park, H.W., Sohn, H., Law, K.H., and Farrar, C.R. (2007). "Time reversal active sensing for health monitoring of a composite plate," *Journal of Sound and Vibration*, Vol. 302, pp. 50–66
33. Gelman, L., Giurgiutiu, V., and Petrunin, L., (2004). "Advantage of Using the Fourier Components Pair instead of Power Spectral Density for Fatigue Crack Diagnostics," *International Journal of COMADEM*, Vol. 7, No.2, pp.18–22
34. Charlesworth, J.P. and Temple, J.A.G. (1989). "Engineering Applications of Ultrasonic Time of Flight Diffraction," Research Studies Press LTD.,
35. Fromme, P. (2002). "Defect detection in plates using guided waves," Swiss Federal Institute of Technology, Doctoral Thesis

36. Michaels, J.E. and Michaels, T.E. (2005). "Detection of structural damage from the local temporal coherence of diffuse ultrasonic signals," *IEEE transactions on ultrasonics, ferroelectrics, and frequency control*, Vol. 52, No. 10, pp.1769–1782
37. Ritdumrongkul, S. and Fujino, Y. (2007). "Identification of the location and size of cracks in beams by a piezoceramic actuator–sensor," *Structural Control Health Monitoring*, Vol. 14, pp.931–943
38. Lu, Y., Ye, L. and Su, Z. (2006). "Crack identification in aluminum plates using Lamb wave signals of a PZT sensor network," *Smart Materials and Structures*. Vol. 15, pp.839–849
39. Yan, F., Royer, R.L. Jr. and Rose, J.L. (2010). "Ultrasonic Guided Wave Imaging Techniques in Structural Health Monitoring," *Journal of intelligent material systems and structures*, Vol. 21, pp. 377–384
40. Kerbrat, E., Clorennec, D., Prada, C., Royer, D., Cassereau, D., and Fink, M. (2002). "Detection of cracks in a thin air-filled hollow cylinder by application of the DORT method to elastic components of the echo," *Ultrasonics*, Vol. 40, pp 715–720
41. Giurgiutiu, V. (2005). "Tuned Lamb wave Excitation and Detection with Piezoelectric Wafer Active Sensors for Structural Health Monitoring," *Journal of intelligent material systems and structures*, Vol. 16, pp. 291–305
42. Sicard, R., Chahbaz, A. and Goyette, J. (2004). "Guided Lamb Waves and L-SAFT Processing Technique for Enhanced Detection and Imaging of Corrosion Defects in Plates with Small Depth-to-Wavelength Ratio," *IEEE transactions on ultrasonics, ferroelectrics, and frequency control*, Vol. 51, No. 10. pp.1287–1297
43. Cope, D., Cronenberger, J, Kozak, K., Schrader, K., Smith, L., and Thwing, C. (2010). "Integration of remote sensing and risk analysis for airframe structural integrity assessment," *Annual Conference of the Prognostics and Health Management Society*
44. An, D., Choi, J., Kim, N.H., and Pattabhiraman, S. (2011). "Fatigue life prediction based on Bayesian approach to incorporate field data into probability model," *Structural Engineering and Mechanics*, Vol. 37, No. 4, pp. 427–442
45. Pattabhiraman, S., Kim, N.H., and Haftka, R.T. (2010). "Modeling average maintenance behavior of fleet of airplanes using fleet-MCS," *AIAA Infotech@Aerospace 2010*, Atlanta, GA, USA
46. Morse, P.M. and Feshbach, H. (1953). "*Methods of Theoretical Physics*," Feshbach Publishing. LLC



47. Rose, J.L. (1999). "Ultrasonic waves in solid media," Cambridge University Press
48. Born, M. and Wolf, E. (1999) "Principles of Optics," Cambridge University Press
49. Graff, K.F. (1991). "Wave motion in elastic solids," New York: Dover
50. Bayliss, A., Jordan, K.E., LeMesurier, B.J. and Turkel, E. (1986). "A fourth-order accurate finite-difference scheme for the computation of elastic waves," *Bulletin of the Seismological Society of America*, Vol. 76, No.4, pp. 1115–1132
51. Lin, X. and Yuan, F.G. (2001). "Detection of Multiple Damages by Prestack Reverse-Time Migration," *AIAA Journal*, Vol. 39, No. 11, pp. 195–211
52. Wang, L. and Yuan, F.G. (2007). "Group velocity and characteristic wave curves of Lamb waves in composites: Modeling and experiments," *Composites Science and Technology*, Vol. 67, pp. 1370–1384
53. Zhou, L., Yuan, F.G., and Meng, W.J. (2007). "A pre-stack migration method for damage identification in composite structures," *Smart Structures and Systems*, Vol. 3, No. 4, pp. 439-454
54. Wang, L. and Yuan, F.G. (2005). "Damage identification in a composite plate using prestack reverse-time migration technique," *Structural Health Monitoring*, Vol. 4, No. 3, pp. 195-211
55. Lin, X. and Yuan, F.G. (2005). "Experimental study applying a migration technique in structural health monitoring," *Structural Health Monitoring*, Vol. 4, No. 4, pp. 341–353
56. Lin, X. and Yuan, F.G. (2001). "Damage Detection of a Plate Using Migration Technique," *Journal of Intelligent Materials Systems and Structures*, Vol. 12, pp. 469-482
57. An, J., Haftka, R.T., Kim, N., Yuan, F.G., and Kwak, B.M. (2008). "Bayesian Approach for Structural Health Monitoring – Application to Migration Technique," *US-Korea Workshop on Bio-Inspired Sensor Technology and Infrastructure Monitoring*, Korea
58. An, J., Haftka, R.T., Kim, N., Yuan, F.G., and Kwak, B.M. (2009). "Compensation for Decay of Signal Strength in Damage Detection by Ultrasonic Imaging: Application to Migration Technique," *50<sup>th</sup> AIAA/ASME/ASCE/AHS /ASC Structures, Structural Dynamics, and Materials Conference*, Palm Springs, California

59. Kulkarni, S.S. and Achenbach, J.D. (2008). "Structural health monitoring and damage prognosis in fatigue," *Structural Health Monitoring*, Vol. 7, No. 1, pp. 37–49
60. Wang P. and Youn, B.D. (2009). "A generic Bayesian framework for real-time prognostics and health management (PHM)," *50<sup>th</sup> AIAA/ASME/ASCE/AHS/ASC Structures, Structural Dynamics, and Materials Conference*, Palm Springs, California
61. Mohanty, S., Chattopadhyay, A., Wei J., and Peralta, P. (2009). "On-line Structural Health Monitoring and Prognosis of a Biaxial Cruciform Specimen," *50<sup>th</sup> AIAA/ASME/ASCE/ AHS/ASC Structures, Structural Dynamics, and Materials Conference*, Palm Springs, California
62. Brown, R.L. and Adams, D.E. (2003). "Equilibrium point damage prognosis models for structural health monitoring," *Journal of Sound and Vibration*, Vol. 262, pp.591–611
63. Biran, B. and Reusens, P.P.F. (1997). "Signal coupler with automatic common line attenuation compensation," *United States Patent*, No. 5,627,501
64. Szewczak, J.M. and Powell, F.L. (2003). "Open-flow plethysmography with pressure- decay compensation," *Respiratory physiology & neurobiology*, Vol. 134, No. 1, pp. 57–67
65. Rutherford, S.R. (1993). "Noise-discriminating, statistical-amplitude compensation for AVO analysis," *Geophysics* Vol. 58, No. 12, pp. 1831–1839
66. Hughes, D.I. and Duck, F.A. (1997). "Automatic Attenuation Compensation for Ultrasonic Imaging," *Ultrasound in Med. and Biol.*, Vol. 23, No. 5, pp. 651–664
67. Stolt, R.H. (1978). "Migration by Fourier transform," *Geophysics*, Vol. 43, No. 1, pp. 23–48
68. Gazdag, J. (1979). "Wave equation migration with the phase-shift method," *Geophysics*, Vol. 43, No.12, pp.1342–1351
69. An, J., Acar, E., Haftka, R.T., Kim, N.H., Ifju, P.G., and Johnson, T.F. (2008). "Being conservative with a limited number of test results," *Journal of Aircraft*, Vol. 45, No. 6, pp. 1969–1975
70. Schijve, J. (2007). "Multiple-site Damage in Aircraft Fuselage Structures," *Fatigue & Fracture of Engineering Materials & Structures*, Vol. 18, No. 3, pp. 329–344
71. Sanford, R.J. (2003). "Principles of Fracture Mechanics," Prentice Hall

72. An, J., Haftka, R.T., Kim, N.H., Yuan, F.G., Kwak, B.M., Sohn, H., and Yeum, C.M. (2010). "Experimental Study on Identifying Cracks of Increasing Size using Ultrasonic Excitation," *Structural Health Monitoring*, accepted
73. Coppe, A., Haftka, R.T., Kim, N.H., and Yuan, F.G. (2010). "Uncertainty reduction of damage growth properties using structural health monitoring," *Journal of Aircraft*, Vol. 47, No. 6, pp. 2030–2038
74. Paris P., Tada H., Donald J. (1999). "Service load fatigue damage—a historical perspective," *International Journal of fatigue*, Vol.21, pp.35-46
75. Elber W. (1971). "The significance of crack closure," *Damage tolerance in aircraft structures, ASTM STP 486*, pp.230-242.
76. Paris P., Lados D., Tada H. (2008). "Reflections on identifying the real DK effective in the threshold region and beyond," *Engineering Fracture Mechanics* Vol.75(3-4) pp.299-305
77. Xue S., Tang H., and Xie Q. (2008). "Structural Damage Detection Using Auxiliary Particle Filtering Method," *Structural Health Monitoring OnlineFirst*
78. Zio E. and Peloni G. (2010). "Particle filtering prognostic estimation of the remaining useful life of nonlinear components," *Reliability Engineering and System Safety* online publication

## BIOGRAPHICAL SKETCH

Jungeun An was born in 1980 in Chinhae, South Korea. He received his B.S. in mechanical engineering from KAIST (Korea Advanced Institute of Science and Technology) in 2003, and received his first Ph.D. in mechanical engineering from KAIST (Advisor: Prof. Byung Man Kwak) in 2010. He has collaborated with Prof. Raphael T. Haftka and Prof. Nam-Ho Kim in University of Florida since 2007, and he received his second Ph.D. in aerospace engineering from the University of Florida in the summer of 2011.